The electrical resistivity of the Posidonia black shale

– from magnetotelluric exploration to rock samples

Dissertation
zur Erlangung des Doktorgrades
der Naturwissenschaften
am Fachbereich Geowissenschaften
der Freien Universität Berlin

vorgelegt von

Filipe Jorge Santos Ferreira Adão

Potsdam, 2015

1. Gutachter: PD Dr. Oliver Ritter
(Freie Universität Berlin, Fachbereich Geowissenschaften, Fachrichtung Geophysik, Deutsches GeoForschungsZentrum Potsdam)

2. Gutachter: Prof. Dr. Serge A. Shapiro
(Freie Universität Berlin, Fachbereich Geowissenschaften, Fachrichtung Geophysik)

Tag der Disputation: 06.02.2015

Abstract

I carried out a magnetotelluric field survey in the southeastern area of the Lower Saxony Basin, in Germany. Eighty-three magnetotelluric stations were deployed along a SW-NE, sixty-three kilometre long profile. The main goals of the survey were of testing this geophysical method for imaging the regional Posidonia black shale formation and evaluating the influence of thermal maturity in its electrical resistivity.

The acquired data were highly affected by cultural noise. For this reason, I discarded the southern profile section between stations one and twenty-seven. However, data processing was successful for the majority of stations between twenty-eight and eighty-three.

The corresponding geo-electric strike estimates point to a predominantly E-W direction, in accordance with regional geology and major faults.

Two-dimensional magnetotelluric inversion results of the acquired data show a series of electrically conductive structures which correlate with brine saturated sediments but also with deeper, meta-anthracitic/graphitized Carboniferous coals. However, none of these structures could be directly related with the Posidonia black shale, which appears to be generally electrically resistive due to its low thermal maturity and, therefore, very difficult to resolve with the magnetotelluric method.

Besides the magnetotelluric experiment, I made a series of laboratory measurements of electrical resistivity on a set of Posidonia black shale samples from the Hils syncline structure found in the Lower Saxony basin. The corresponding rock samples were collected in shallow wells named Wickensen, Harderode and Haddessen. These three wells show immature, oil and gas thermal maturities, respectively. Results showed that the Posidonia black shale samples are electrically resistive, when measured in dry conditions. Furthemore, electrical resistivity is consistently higher when measured against rock bedding, which indicates that the Posidonia black shale is heterogeneous and electrically anisotropic.

I observed no direct correlation between electrical resistivity and thermal maturity: the Harderode samples showed the highest electrical resistivity, whilst the Haddessen samples showed the lowest. This was an unexpected result because the increase of thermal maturity between Wickensen and Haddessen contributed to the aromatization of the organic carbon in the Posidonia black shale. Consequently, this effect should have contributed to a constant

decrease of electrical resistivity in the Posidonia black shale between Wickensen and Haddessen. An ineffective drying process and the presence of moisture could have been the reasons for the observed trend of electrical resistivity.

I tested the dependence of electrical resistivity of the Posidonia black shale samples on water content by saturating them with distilled and saline water solutions. The saturation process led to a constant and significant decrease of electrical resistivity of the experimented samples. Moreover, increasing salinity corresponded to higher drops in electrical resistivity for the Wickensen and Harderode samples. However, the observed decrease of electrical resistivity with distilled water of electrical resistivity was generally lower at the Haddessen samples, meaning the influence of water content in electric conduction could be lower for these samples.

To constrain the influence of water content in electric conduction through the Posidonia black shale, I measured the porosity of all samples and correlated it with electrical resistivity of the water saturated samples. Strong and positive correlations were observed for the Wickensen and Harderode samples. No correlation was observed, however, for the Haddessen samples, possibly due to the lack data points. These observations indicate that the electrical resistivity of Posidonia black shale, at the immature and hydrocarbon generation stages, is porosity controlled.

I also correlated electrical resistivity with the organic carbon content of the samples. No correlation was observed in the Wickensen and Harderode samples, but a strong and positive correlation was observed for the Haddessen samples. This result together with the less prominent influence of water in electric conduction through the Haddessen samples strengthens the possibility of a more influential role of carbon in electric conduction at the gas stage in detriment of pore water and porosity.

I conclude from my research that the electrical conductivity of black shales depends on a variety of factors. At immature and hydrocarbon-generation thermal maturities the Posidonia black shale is not electrically conductive. Furthermore, electric conduction at these maturities seems to be mainly controlled by water content and porosity rather than by carbon content. Because of this, the magnetotelluric method has limited potential for the exploration of such black shales in sedimentary basins such as the Lower Saxony basin. The main difficulty is to distinguish them from other over- and underlying water-rich formations. It is possible, however, to characterize black shales with higher thermal maturities. The deep and highly conductive body present in the inversion models related to meta-anthracitic/graphitized Carboniferous coals, is proof of that possibility.

Contents

1 Introduction

Black shales are seen today as one of the most promising alternative source rocks for oil and gas of the future. They contain high levels of organic carbon in the form of kerogen (insoluble organic matter) and/or bitumen (soluble organic matter) that converts into hydrocarbons (oil and gas) under the right thermogenic and/or biogenic conditions (Jarvie et al. 2007). In general, it is known that thermal maturation is responsible for hydrocarbon generation in black shales (Tissot & Welte 1984; Selley 1998). However, the geochemical processes undergone in the organic carbon and their consequences on the physical properties of the rock, such as porosity and permeability, are not fully understood.

In the year of 2009, a project called GASH (Gas Shales in Europe: www.gas-shales.org) was created to better understand and characterize black shales and the associated effects of thermal maturation. For these efforts, the project brought together hydrocarbon exploration companies and research institutes from Europe in the field of geosciences. Within the framework of the project, research was performed in the fields of geochemistry and petro-physics (rock mechanics, porosity, permeability and fluid-flow) at the reservoir scale, and in the fields of geophysics (seismic and magnetotellurics (MT)) and basin modelling at the regional scale. This thesis focuses on the geophysical part of the project, specifically on the MT study.

Black shales have been suggested as possible causes for a number of low electrical resistivity anomalies found in the Earth's upper crust (Gaucher 1983; Loukola-Ruskeeniemi 1989; Korja & Koivukoski 1990). Low electrical resistivity in black shales is also related to high thermal maturation (>400°C) (Duba et al. 1988; Raab 1998). Increasing temperatures provoke a change in the chemical composition of the organic carbon found at the grain boundaries of black shales, which consequently turns it into an electrically conducting phase (Jödicke 1992). More recently, a study by Weckmann et al. (2007b) imaged the Whitehill black shale horizon in South Africa as a laterally extensive layer of very low electrical resistivity which could be mapped over hundreds of kilometres. Complementing this study, laboratory measurements were also conducted on Whitehill black shale rock samples and confirmed that lower electrical resistivity was related to those samples which had been exposed to higher temperatures (Branch et al. 2007).

Various black shale formations have been identified in Europe and investigated for GASH. One of them was the Posidonia black shale (PBS), which is located in the Lower Saxony Basin (LSB), in Germany. In this area, the research groups involved in GASH conducted geochemical, petrophysical, seismics and basin modelling studies. The PBS formation is a Lower Jurassic, 100 m thick, sedimentary horizon that is found predominantly at 2 km depth (e.g. Bruns et al. 2013). Furthermore, it has been influenced by a thermal maturity anomaly centred at the southern part of the LSB (Bartenstein et al. 1971). In other words, the PBS experienced different temperature levels, which were maximum at the southern margin and minimum at the northern margin of the LSB. It was, therefore, an objective of the MT experiment to resolve the PBS as a distinguishable feature and study a possible relation with thermal maturity. To accomplish this, a 63 km-long MT profile, was set up during November/December of 2011. It consisted of 83 stations and it crosses the LSB between the cities of Osnabrück and Hannover (Figure 1.1) and is approximately perpendicular to the main geological strike direction (Baldschun et al. 2001).

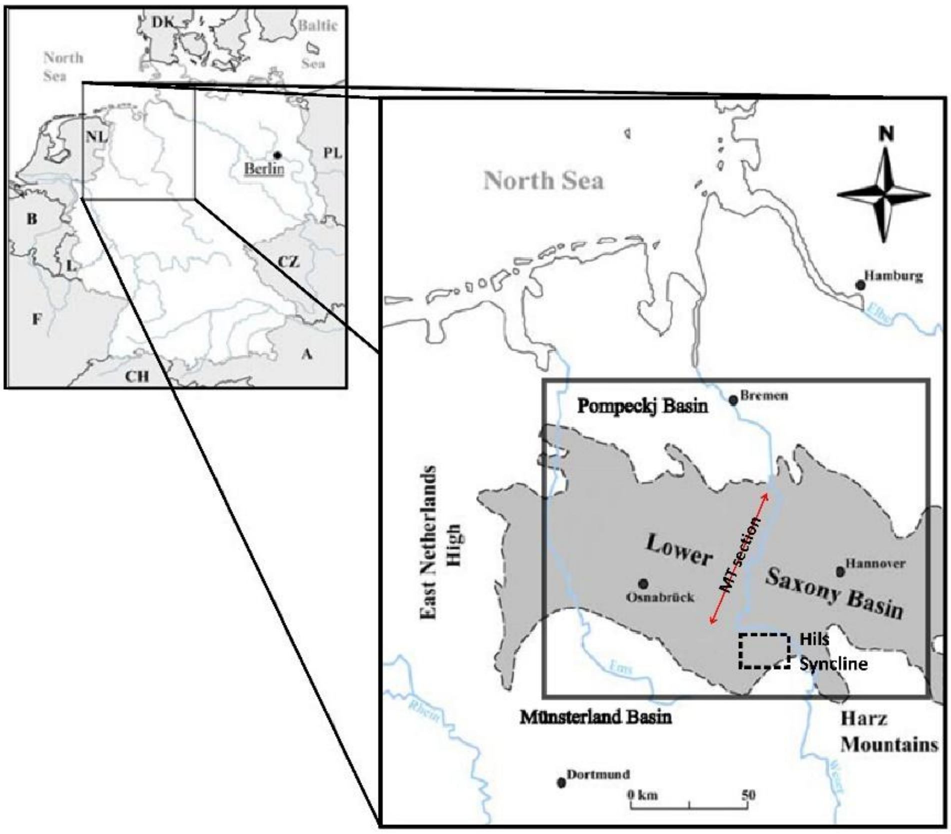

Figure 1.1 - Location of the MT profile and Hils Syncline area in the Lower Saxony basin, in northwestern Germany (modified after Bruns et al. 2013).

In addition to the MT study, I also carried out a series of laboratory measurements on PBS samples to characterize their electrical properties. These samples were collected from three different wells (Wickensen, Harderode and Haddessen) located within the Hils syncline in the LSB and cross different levels of thermal maturity (Mann 1987). This structure is located approximately 30 km southeast of the MT profile. The depositional and tectonic history of the PBS is similar between the wells so the differences in their physical and chemical properties is mainly due to varying thermal maturity (Bernard et al. 2012b). With these laboratory measurements, I sought to characterize a possible correlation between electrical resistivity and thermal maturity, total organic carbon, porosity, water content and sample anisotropy, and to use these results as constraints to the interpretation of the MT results.

The remainder of the thesis is structured in the following way: In chapter two, I define black shales and explain where and in which conditions these rocks serve as a source rock. Furthermore, I discuss how thermal maturity affects the composition of black shales and, consequently, their electrical resistivity.

In chapter three, I describe the geological setting of the LSB, in Germany. Moreover, I also explain the thermal maturity anomaly which affects the study area.

In chapter four, I present the MT study carried out in the LSB. This chapter includes the fundamentals of the MT theory, the strategy for data acquisition and its processing, inversion modelling and discussion of the obtained results.

In chapter five, I present the laboratory work done on the PBS samples. This chapter includes the theory behind the determination of electrical resistivity and porosity of the samples, the description of used apparatus, the results and corresponding discussion.

In chapter six, I present the main conclusions and outlook of this thesis.

2 Definition of black shales

A black shale is a ‘dark-coloured’ fine-grained mudrock (Tyson 1987). Mudrocks are known to be primarily constituted of clay minerals, such as illite, muscovite, kaolinite and chlorite, but also quartz and feldspar minerals. However, in the particular case of black shales it is common that carbonate (mainly calcite and dolomite) and sulfide (mainly pyrite and pyrrhotite) minerals also form an important part of the mineral matrix (Wignall 1994). The ‘dark colour’ originates from the richness in organic matter, which is the main distinction to a normal shale. Figure 2.1 shows the typical outward appearance of a black shale.

Figure 2.1 - A typical black shale. Source: Wikipedia.

The deposition of black shales occurs in constricted seas or lakes that possess bottom waters with anoxic conditions (Wignall 1994). Under these conditions, the organic matter (mainly composed of phytoplankton and marine algae) can deposit and be preserved at the bottom of the water column without oxidation and burrowing.

After deposition, and ongoing sedimentation, black shales are formed through diagenesis (Tissot & Welte 1984). During this process organic matter transforms mainly into kerogen but also into bitumen. These two organic compounds, plus hydrocarbons in the form of methane, constitute a black shale's organic matter. A commonly used estimate of organic matter in a black shale is the total organic carbon (TOC) (Selley 1998). TOC represents the carbon that is bound to other organic compounds within the organic matter and can constitute 2 to 10 vol. % of a black shale, sometimes even 20% (Tourtelot 1979).

2.1 Black shale as a source rock

According to a report from the U.S. department of Energy Information Administration (EIA)[1], the most recent estimate for technically recoverable hydrocarbons from 137 black shale formations in 41 countries accumulates to, at least, 345 billion barrels (1 barrel = 159 litres) of shale oil and 7201 trillion cubic feet (tcf) (1 tcf = 0.0283 m^3) of shale gas. Figure 2.2 shows a world map with the location of these formations. The red coloured areas represent those formations which account for the previous estimates and the tan coloured areas represent those formations that have been reviewed but have not yet been accounted in the estimates due to lack of data. To put in perspective, the shale gas and shale oil estimates represent 32% and 10%, respectively, of the total natural gas and oil resources still remaining worldwide. Nevertheless, the worldwide consumption of natural gas and oil is thought to increase from 120 tcf/year and 97 million barrels/year today to 185 tcf/year and 115 million barrels/year in 2040. Therefore, the available shale gas and shale oil reserves are already enough to account for ~66% of the global demand of natural gas and ~80% of the global demand of oil in the next 26 years.

---

[1] "Technically Recoverable Shale Oil and Shale Gas Resources: An Assessment of 137 Shale Formations in 41 Countries Outside the United States" 2013.

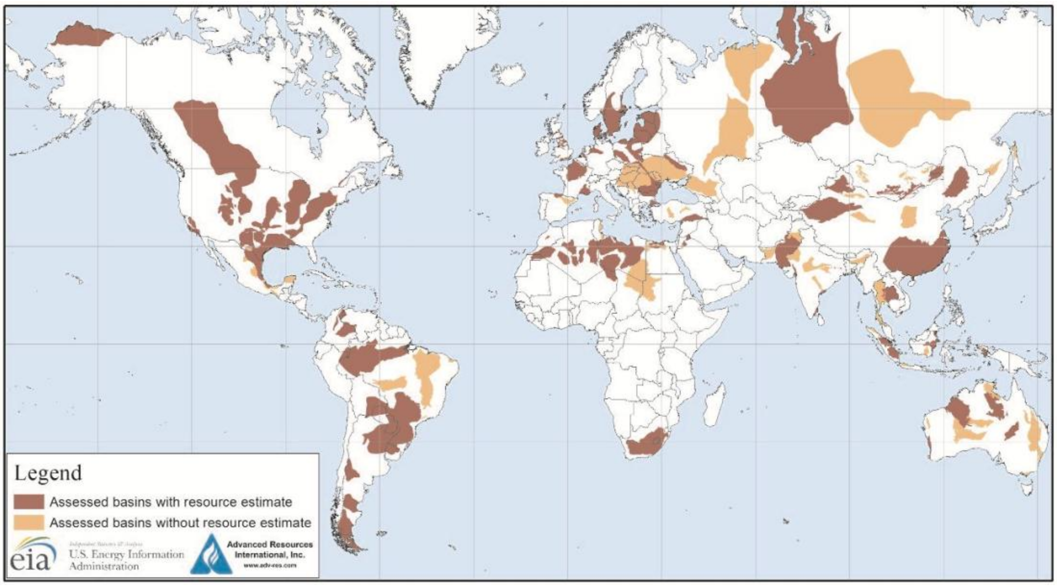

Figure 2.2 - World map showing the distribution of sedimentary basins with and without resource estimates for the corresponding black shale formations. Source: The 2013 U.S. EIA report "Technically Recoverable Shale Oil and Shale Gas Resources: An Assessment of 137 Shale Formations in 41 Countries Outside the United States".

Black shales are an important source-rock because of their organic matter generates hydrocarbons in different forms through thermal cracking (Tourtelot 1979). Thermal cracking occurs with the increase of temperature which occurs with deep burial, heat sources like magmatic intrusions and/or hydrothermal activity. The process of thermal cracking is divided in three phases (Tissot & Welte 1984): The first phase is the already mentioned diagenesis which occurs in the first few hundred meters of burial up to temperatures of 50°C. During diagenesis, methane is generated. The second phase is catagenesis. With the increase of temperature up to 150°C, oil and wet gas are formed. The third and final phase is metagenesis. With further increase of temperature until 200°C dry gas is formed. At higher temperatures, however, hydrocarbon generation ceases.

The released hydrocarbons are stored inside the source-rock’s pore system and/or in the reservoir strata that are overlying the source rock, depending on the particular geology.

For more information on this topic, see Tissot & Welte (1984) and Selley (1998).

2.2 Determining the thermal maturity of black shales

The thermal maturity of black shales is determined by the measure of the maximum temperature they have been exposed to. This property is commonly measured with vitrinite reflectance (Tissot & Welte 1984). The higher the temperature a black shale has been exposed to, the higher the vitrinite reflectance is. Typically, vitrinite reflectance data is presented in units of % Ro, which is the mean percentage of reflected light from a sample which is immersed in oil (% Ro = % reflectance in oil) (Adriasola-Munoz et al. 2007). This method is particularly sensitive in the temperature range of hydrocarbon generation. According to Tissot & Welte (1984), vitrinite reflectance values for the oil generation window lie between 0.6 and 1% Ro. For the gas generation window, between 1 and 2% Ro. For temperatures beyond the oil and gas windows, the remaining organic matter in black shales enters the anthracite stage with vitrinite reflectance as high as 4% Ro. Past this point, the range between maximum and minimum vitrinite reflectance values increases and it becomes difficult to determine the real reflectance (Teichmüller et al. 1979). This is due to the increase in reflectance anisotropy due to chemical rearrangement of the organic matter with thermal maturation. Nevertheless, up until mean reflectance of 10% Ro, anthracitic organic matter is in a metamorphosed state and is sub-categorized as meta-anthracite or amorphous graphite. The last stage of thermal maturation turns meta-anthracitic organic matter into graphite with mean reflectance higher than 10% Ro (Teichmüller et al. 1979).

2.3 Electrical resistivity of black shales

The electrical resistivity of black shales depends mainly on its depositional history. One aspect is the mineral constitution and its distribution. Table 2.1 summarizes electrical resistivity values for minerals typically found in black shales (no values regarding the electrical resistivity of illite were found, unfortunately).

Table 2.1 - Electrical resistivity values for minerals typical for black shales.

References: 1 – Schön (2004); 2- Parkhomenko (1967); 3 – Manouchehri et al. (2001).

Minerals	**Electrical Resistivity (Ωm)**	**References**
Calcite	$9*10^{13}$; $5*10^{12}$	1, 2
Dolomite	$4*10^{13}$	1
Quartz	$10^{12} – 2*10^{14}$	1
Pyrite	$1*10^{-4} – 1*10^{-1}$	1
Pyrrhotite	$6*10^{-4} – 4*10^{-2}$	2
Muscovite	$1*10^{14} – 1*10^{16}$	2
Chlorite	$2*10^{9}$	1
Kaolinite	$3*10^{7}$	1
Illite	-	-
Feldspar	$1*10^{7}$	3

Most of these minerals can be considered insulators because of their high electrical resistivities. The only exceptions are the iron sulphides (e.g. pyrite, pyrrhotite). However, in the case of black shales, iron sulphides normally occur in isolated clusters and do not form widespread interconnected networks required to influence electrical resistivity (regionally) (Wignall 1994).

Also influencing a black shale's electrical resistivity is its organic matter present at grain boundaries and its thermal maturity (Jödicke 1992). Chemically, an immature black shale's organic carbon is composed of dispersed planar aromatic compounds which are linked by aliphatic compounds (Tissot & Welte 1984). Figure 2.3 shows two examples of aliphatic and aromatic compounds found in kerogen and/or bitumen.

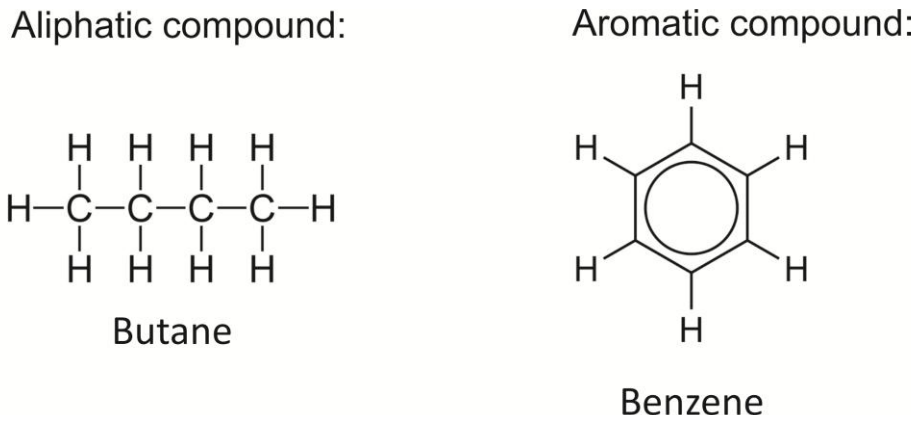

Figure 2.3 - Butane and Benzene hydrocarbons are two examples of aliphatic and aromatic compounds found in kerogen and/or bitumen.

The aromatic carbon rings contain delocalized electrons that are free to circulate onto neighbouring aromatic compounds. However, their aliphatic links do not allow these electrons to circulate freely within the organic matrix. Because of this, immature organic carbon can be considered a non-conductive substance (Walters et al. 2014). When exposed to thermal maturation, however, the chemical arrangement of immature organic carbon changes. Figure 2.4 shows a sketch of the main stages of evolution of organic carbon with thermal maturity.

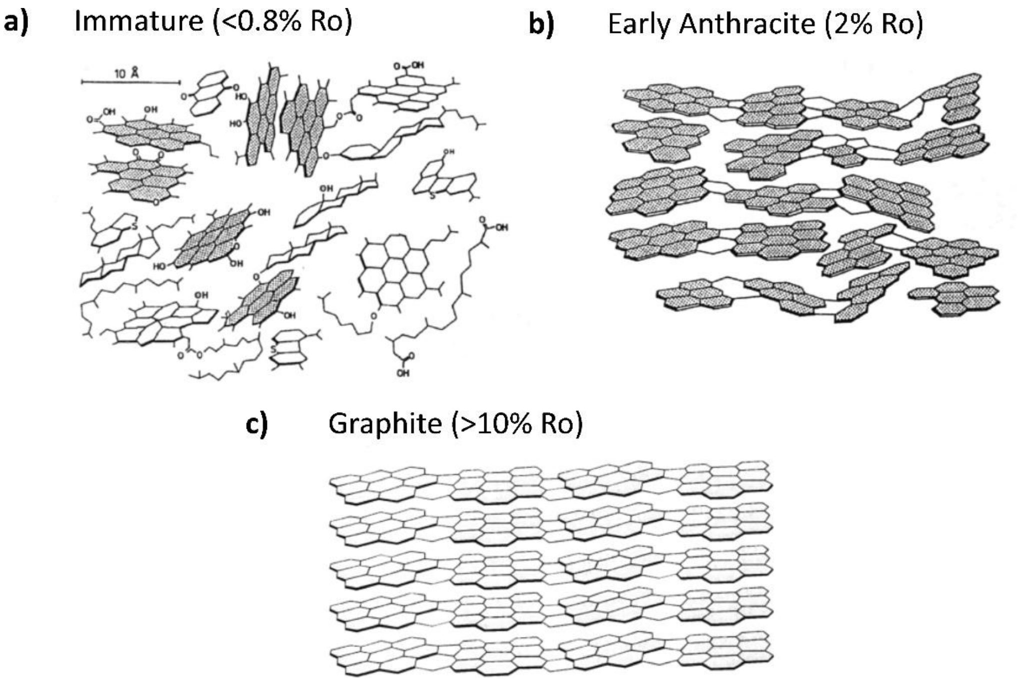

Figure 2.4 - Conceptual model of the structural development of carbon in organic matter at the a) immature/oil stage (<0.8% Ro), b) anthracite stage (~2% Ro) and c) semi-graphite and/or graphite stage (>10% Ro) (modified after Rouzaud & Oberlin 1984).

As oil starts to form from kerogen and bitumen, the remaining organic carbon suffers de-oxidation and de-hydrogenation (Tissot & Welte 1984). This is accompanied by aromatization of the aliphatic compounds which promotes the formation of poly-aromatic structures (Rouzaud & Oberlin 1990). In the gas stage these structures begin to coalesce which leads to a decrease of the electrical resistivity of the black shale (Rouzaud & Oberlin 1990). Furthermore, the poly-aromatic structures progressively align parallel to each other and form planar domains with a turbostratic nature (Villey et al. 1976, 1979; Oberlin et al. 1979; Oberlin 1989). These structures are composed of stacked layers of poly-aromatic carbon with conjugated sp^2 connections that are held together by Van der

Waals forces (e.g. Amelinckx et al. 1965). This carbon configuration is electrically anisotropic because electrical conduction is higher along the planar domains rather than across them (Krishnan & Ganguli 1939). The final stage of turbostratic alignment is the graphite stage. Graphitic carbon is the most electrically conductive carbon structure. Typical range of electrical resistivity of graphite ranges within 3.0×10^{-3} to 2.5×10^{-6} Ωm (e.g. Pierson 1993).

Table 2.2 summarizes reported values and/or ranges of electrical resistivity of black shales in different thermal maturities.

Table 2.2 - Electrical resistivity values and/or ranges of black shales in different thermal maturity stages. References: 1 – Duba (1983); 2 – Ahmad et al. (1991); 3 - Raab et al. (1998); 4 – Duba et al. (1988); 5 – Branch et al. (2007).

Black shale Formation	**Electrical Resistivity (Ωm)**	**Maturation Stage**	**References**
Green River Oil Shale (USA)	$1*10^{7}$	Oil Window	1
El-Lajjun Shale (Jordan)	$1*10^{7}$	Oil Window	2
Altmark Shale (Germany)	$3.6*10^{5}$	Early Anthracite	3
Alum Shale (Germany)	$2*10^{0} – 1.7*10^{1}$	Meta-Anthracite	3, 4
Whitehill Shale (S. Africa)	$4*10^{0} – 6*10^{0}$	Meta-Anthracite	5
Prince Albert Shale (S. Africa)	$8*10^{-3} – 5*10^{3}$	Meta-Anthracite Graphite	5

3 Geological setting

The study area is located in the Lower Saxony Basin (LSB) in northwestern Germany (Figure 3.1). This basin is a graben-in-graben system located within the greater North German Basin (NGB), also known as South Permian Basin (SPB) which is part of the Central European Basin System (CEBS) (e.g. Ziegler 1990; Kockel et al. 1994; van Wees et al. 2000).

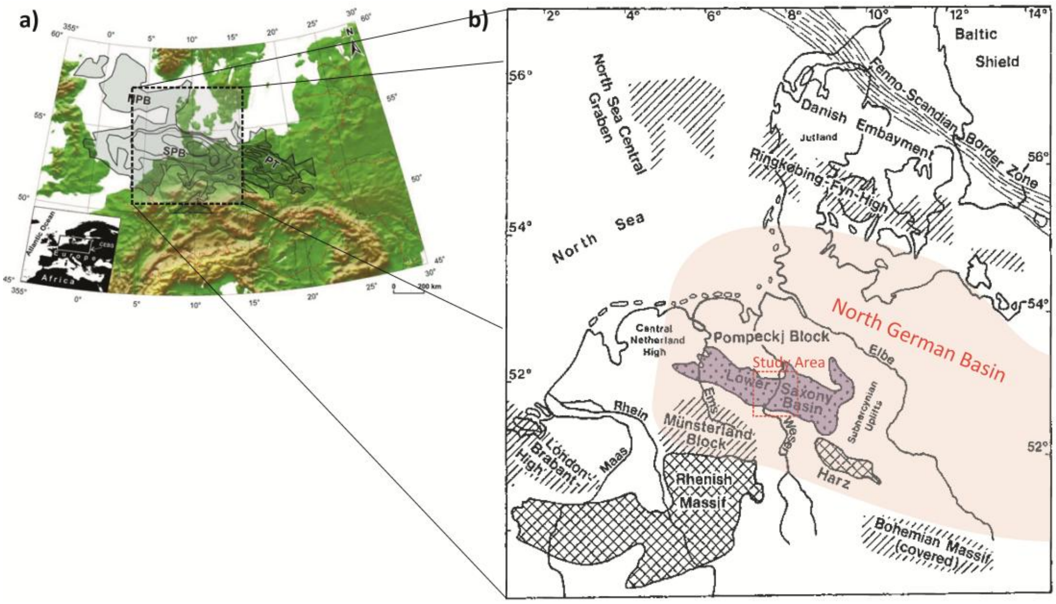

Figure 3.1 - a) Location of the Central European Basin System (CEBS) in Northern Europe (modified after Maystrenko et al. 2008). In outline are the main basin depo-centres of the CEBS (NPB, Northern Permian Basin; SPB, Southern Permian Basin; PT, Polish Trough). b) Location of the study area within the LSB (purple fill), comprised in the NGB (red fill) (modified after Kockel et al. 1994).

The NGB is deposited on Variscan crust in the south and on Caledonian crust in the north (Ziegler 1990). The central part of the NGB is believed to be deposited on the pre-Caledonian North German massif (Torsvik et al. 1993; Franke et al. 1996; Tanner & Meissner 1996). Total thickness of Late Carboniferous to Cenozoic sediment infill can exceed 8 km in its depo-centres (Schwab 1985; Bayer et al. 1995). For a general stratigraphic column of the LSB, with the main tectonic events and corresponding litho-stratigraphy, see Figure 3.2.

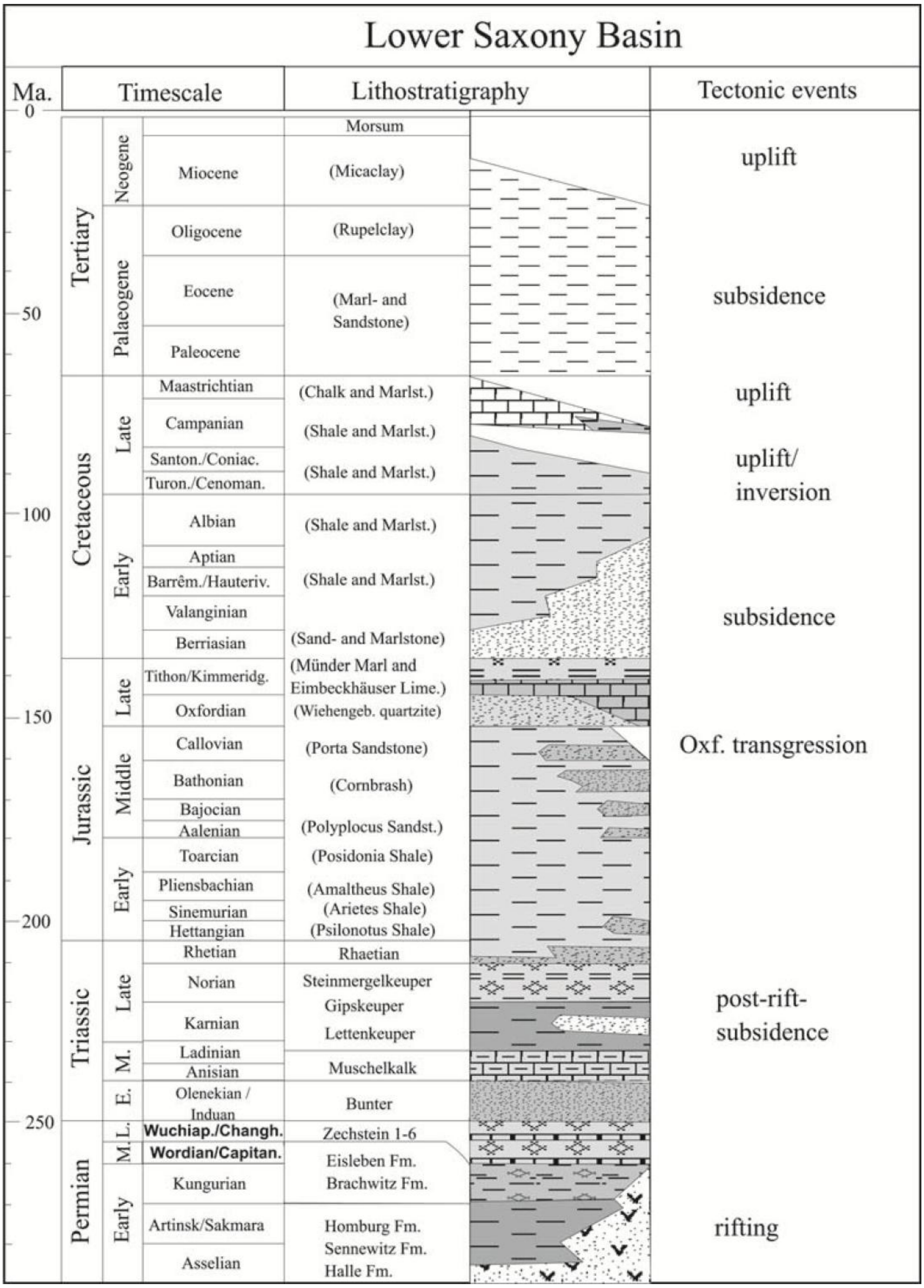

Figure 3.2 - Generalized stratigraphy of the LSB from Permian until recent times based on the German Stratigraphic Commission (modified after Senglaub et al. 2006).

Main orogenies

Structural evolution initiated in Late Carboniferous - Early Permian with N-S rifting of the area of the CEBS caused by the Variscan mountain range. This crust build-up formed due to the collision of the Euramerica and Gondwana continents (Ziegler 1990). This event was accompanied by strong volcanism (Benek et al. 1996; Breitreuz & Kennedy 1999). Then, between the Early Permian and Middle Triassic, thermal relaxation of the lithosphere and sedimentary loading caused subsidence of the northwestern and centre areas of the CEBS (Scheck & Bayer 1999). This caused former N-S trending grabens to join and form the predominant WNW-ESE sediment depo-centres related to the NGB and NPB (Betz et al. 1987; Ziegler 1990). Afterwards, between the Middle Triassic and Jurassic, differentiation in sediment depo-centres occurred due to a new E-W extension regime related to the Atlantic continental break-up between the American and European continents (Mazur & Scheck-Wenderoth 2005). This led to a new alignment of the NGB sediment depo-centre from a WNW-ESE alignment to a NNE-SSW alignment (Betz et al. 1987; Scheck & Bayer 1999). Furthermore, at this stage, a vertical movement of Zechstein salt was initiated (Scheck et al. 2003a; Scheck-Wenderoth et al. 2008b).

In the Late Jurassic subsidence decreased (Kossow & Krawczyk 2002) and the uplift of the NGB began, which led to erosional unconformities (Betz et al. 1987). A dextral trans-tensional regime was established during the Early Cretaceous, in addition to pre-existing tectonics (Betz et al. 1987; Scheck & Bayer 1999). As a consequence, the WNW-ESE Variscan structures were reactivated which caused strike-slip displacements and consequent formation of en-echelon sub-basins in the NGB, one of them being the LSB (Mazur & Scheck-Wenderoth 2005). Also, further salt movement occurred during this time (Scheck et al. 2003a; Scheck-Wenderoth et al. 2008b).

Between the Late Cretaceous and Palaeocene, the collision of Gondwana and Eurasia led to an inversion of the LSB induced by the Subhercynian/Lamaride tectonic phase (Kockel 2002; Maystrenko et al. 2008). Basin inversion is the relative uplift of a sedimentary basin or of similar structures as a result of crustal shortening. This event led to the uplift of the southern margin of the LSB (along the pre-Permian Osning lineament) and resulted in erosion of more than 6000 m of sediments (Senglaub et al. 2005, 2006; Adriasola-Munoz et al. 2007). Whilst the LSB was inverted, the neighbouring sedimentary blocks underwent subsidence (Walter et al. 1995; Petmecky et al. 1999).

After the inversion period, thermal subsidence of the entire CEBS was resumed in the Tertiary due to far-field tectonic stress coming from continent collisions associated with the Pyrenees and/or the Alps mountain ranges (Scheck-Wenderoth & Lamarche 2005; Rasser & Harzhauser 2008). This subsidence process was accompanied by Zechstein salt vertical movement, which increased the growth of the previous Middle Triassic and Jurassic N-S oriented salt walls (Scheck & Bayer 1999). The overall present-day stress regime in the CEBS exists since the Miocene and is predominantly characterized by NW-SE compression and NE-SW extension (Heidbach et al 2008). The cause of these effects is the on-going push forces of the Atlantic ridge and the forces related to convergence of the Eurasian and African plates (Gölke & Goblenz 1996; Goes et al. 2000).

Lithostratigraphy

The main lithologies of the NGB in the area of the LSB are the following: the Namurian and Westphalian stages of the Carboniferous are known for its organic-rich coal seams (Scheidt & Littke 1989), which are intercalated with silt- and sandstones (Senglaub et al. 2005). These sediments denote the depositional shift from the Devonian marine environment to a Carboniferous partly terrestrial environment (Hedemann et al. 1984). The coal formations are regarded as one of most important natural gas producing formations in NW Europe (e.g. Kockel et al. 1994; Littke et al. 1995; Adriasola-Munoz et al. 2007). Overlying Permian sandstones and limestones form perfect hydrocarbon reservoir layers (Kockel et al. 1994). Stephanian and Rotliegend volcanoclastic sediments are rare below the LSB and are mostly confined to its northern part (Maystrenko et al. 2010). The Permian gas reservoirs are then capped by a 1000 m thick evaporate layer (carbonates, anhydrites and salt) that was deposited during the transgressive hypersaline Zechstein Sea (Petmecky et al. 1999). After regression of the sea, the following Lower Triassic sediments are composed of red clastics, which were deposited in a terrestrial to lacustrine and fluvio-deltaic environment (Stollhofen et al. 2008). Then in the Middle Triassic a marine transgression established a shallower marine environment in the NGB (Schöneberg & Neugebauer 1987). The corresponding Muschelkalk sediments are composed mainly of carbonates and interbedded evaporites (Petmecky et al. 1999). The Late Triassic is then predominantly composed of clastic Keuper sediments (Stollhofen et al. 2008). In the Rhaetian sea-level rose and re-established epicontinental marine conditions (Bruns et al. 2013). By the Late Jurassic the Posidonia black shale, the target formation of this study, was deposited (Kockel et al. 1994). It is a widespread organic carbon and carbonate-rich black shale, nowadays located at 1 to 2 km depth with an average thickness of 16 to 40 m (e.g. Riegel et al. 1986; Littke et al. 1991; Kockel et al. 1994). Total duration of deposition during the Toarcian of the Posidona black shale was of about two to three million years (Littke et al. 1991). According to Teichmüller & Ottenjhan (1977) the bulk of the organic matter is derived from phytoplankton (green algae) and bituminite, whereas small amounts of land plant-derived vitrinites and inertinites are present. Its well-laminated character and the absence of current influence indicate that deposition took place below current and wave base (Littke et al. 1991). Furthermore, the lack of burrowing and the abundance of well-preserved hydrogen-rich organic matter point towards stagnant and anoxic deposition conditions at the Toarcian Sea (Littke et al. 1991). Outside the LSB, Posidonia black shale can also be found in the North Sea basin (Morris 1980; Jenkins 1985), the Paris Basin (Espitalié et al. 1987), the Upper Rhine Graben (Welte 1979) and the Yorkshire basin (Ziegler 1990). After the deposition of the Posidonia black shale, during the Middle Jurassic Dogger, regular marine shale was deposited, intercalated with sandstone during the a period of transgressive-regressive cycles affecting sea-level (Gramann et al. 1997). By the Late Jurassic a more constant regression of the marine environment led to the deposition of Malm carbonates and evaporites (Mutterlose et al. 2000; Senglaub et al. 2005). Then, depositional conditions in the Late Jurassic and Early Cretaceous corresponded to a shallow marine environment with terrestrial influence (Petmecky et al. 1999). Until the Early Aptian organic-rich clastics were deposited and in the Coniacian the deposition of carbonates was resumed (Bruns et al. 2013). A period of basin inversion followed by basin uplift which lasted until the end of the Cretaceous led to the erosion of most of the Late Cretaceous sediments (Senglaub et al. 2005). Sedimentation of clay-rich sandstones resumed in the Paleocene and is on-going (Betz et al. 1987). However, due to the northward tilt of the LSB these sediments are mostly exposed on the northern margin (Bruns et al. 2013).

3.1 Thermal maturity of the Lower Saxony Basin

In the southwestern part of the LSB, around the area of Bramsche and extending to the east, a positive thermal maturity anomaly has been found (Figure 3.3). In the center of the anomaly, vitrinite reflectance of out-cropping Upper Jurassic organic-rich rocks have been measured between 2.99 and 4.56 % Ro (Bartenstein et al. 1971).

The cause for the thermal maturity anomaly in the LSB was initially attributed to the presence of deep-seated igneous intrusions, known as Bramsche and Vlotho massifs. This theory was supported with the existence of magnetic (Schmidt 1914; Breyer 1971) and positive gravimetric anomalies (Hahn & Kind 1971; Flotow et al. 1931). However, recent basin modelling studies for maturity distribution and temperature history have excluded that possibility and suggest instead that the observed maturity pattern of the LSB is more likely to be caused by elevated heat flows which occurred during the Upper Jurassic basinrifting, the Early Cretaceous basin inversion and the Early Cretaceous basin uplift tectonic events (Petmecky et al. 1999).

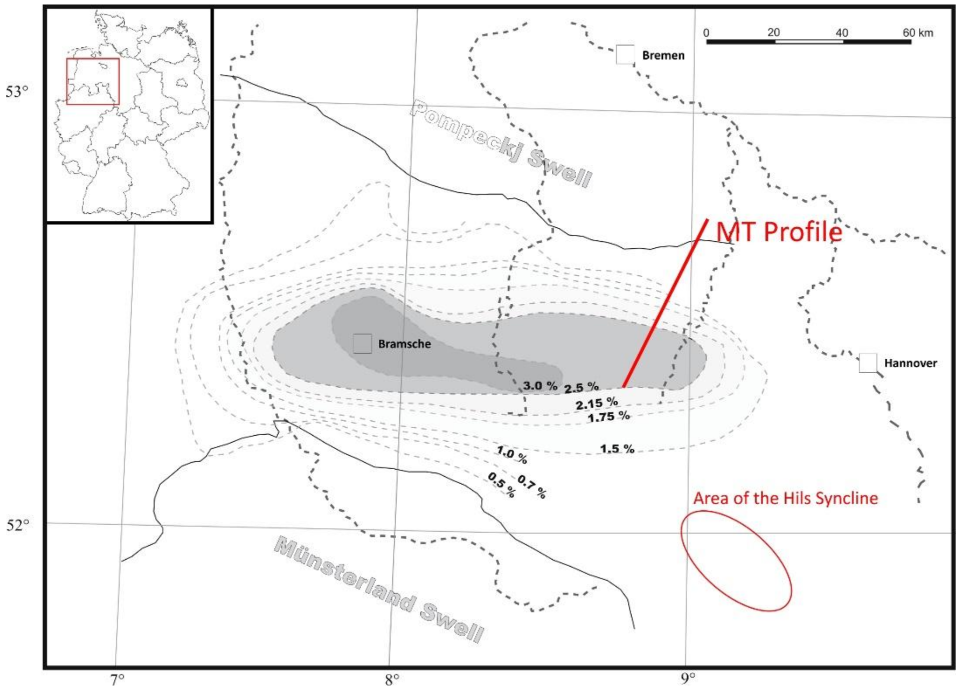

Figure 3.3 - Coalification map of the Upper Jurassic of the LSB based on Bartenstein et al. (1971) (modified after Senglaub et al. 2006). Black lines correspond to the boundaries of the LSB in relation to the Pompeckj and Münsterland Swells; dark grey dashed lines show main rivers; Light grey dashed lines correspond to vitritinite reflectance isolines. For more information on the Hils Syncline area, see chapter 5.

4 Magnetotelluric study of the Posidonia black shale

4.1 Theory of the magnetotelluric method

The magnetotelluric method (MT) was primarily described by Tikhonov (1950) and Cagniard (1953) and has been developed ever since. It is a passive geophysical method that allows one to gain information on the electrical conductivity distribution on any given underlying geological structure, using the natural electromagnetic field's diffusion and decay through Earth's interior.

The electric, **E**, and magnetic, **H**, fields propagating through an isotropic medium obey to the Maxwell equations:

$$\nabla \times \mathbf{E} = -\mu \frac{\partial \mathbf{H}}{\partial \mathrm{t}} \tag{4.1}$$

$$\nabla \times \mathbf{H} = \left(\mathbf{J} + \frac{\partial \mathbf{D}}{\partial \mathrm{t}}\right) \tag{4.2}$$

$$\nabla \cdot \mathbf{D} = q \tag{4.3}$$

$$\nabla \cdot \mathbf{H} = 0 \tag{4.4}$$

D represents the displacement current and **J** the current density. All quantities in **bold** are vectorial. q and μ are scalar quantities that represent the charge density and the magnetic permeability, respectively. The S.I. units of the quantities are expressed in the following table:

Table 4.1 - Quantities and respective units.

	Units	
E	Volt/meter	(V/m)
D	Coulomb/meter^2	(C/m^2)
H	Ampere/meter	(A/m)
B	Weber/meter^2	(wb/m^2)
J	Ampere/meter^2	(A/m^2)
μ	Henry/meter	(H/m)
ρ	Coulomb/meter^3	(C/m^3)

According to Faraday's law 4.1, a time varying magnetic field induces an electric field. According to Ampere's law 4.2 secondary magnetic field is induced. Equations 4.3 and 4.4 (after Gauss) state the source of electric field is proportional to the distribution of electric charge and that magnetic monopoles are non-existent, respectively. The referred vectorial quantities are related through the following expressions:

$$\mathbf{J} = \sigma\mathbf{E} \tag{4.5}$$

$$\mathbf{D} = \varepsilon_0\varepsilon_r\mathbf{E} = \varepsilon\mathbf{E} \tag{4.6}$$

$$\mathbf{B} = \mu_0\mu_r\mathbf{H} = \mu\mathbf{H} \tag{4.7}$$

where ε_0 is the permittivity of the free space, ε_r the relative permittivity, μ_0 the permeability of the free space, μ_r the relative permeability, and σ the electrical conductivity. The SI units and dimensions are:

Table 4.2 - Quantities and respective units.

	Units	
ε	Farad/meter	(F/m)
σ	Siemens/meter	(Ω/m)

The values for electric permittivity and magnetic permeability in free-space are of 8.85×10^{-12} As/Vm and $4\pi\times10^{-7}$ Vs/Am, respectively. These values are roughly the same for most rocks and materials existing in the Earth. Electrical conductivity, though, is different and varies quite a lot from rock to rock. Figure 4.1 shows a rough spectrum of electrical resistivity (inverse of conductivity) associated to different classes of rock:

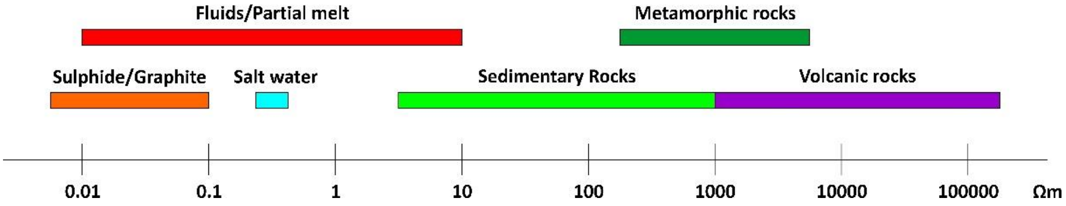

Figure 4.1 - Diagram of electric resistivity for different rocks. Sources: Haak & Hutton (1986), Simpson & Bahr (2005), Chave & Jones (2012).

For MT, the following the simplifications of the Maxwell equations are applied (Cagniard 1953; Jiracek 1990; Keller & Frischknecht 1966):

- The natural electromagnetic source fields used in MT are generated by large-scale Ionospheric current systems. These fields are generated far away so they can be considered as uniform, plane waves which have a near-vertical incidence on Earth's surface. The electric and the magnetic fields are described through the following mathematical formulas:

  $$\mathbf{E} = E_0\, e^{i\omega t - kz} \tag{4.8}$$

  $$\mathbf{B} = B_0 e^{i\omega t - kz} \tag{4.9}$$

  E_0 and H_0 are the initial amplitudes on the Earth's surface, ω the angular frequency and k the wave number. These fields are time-dependent, but their change in time is slow enough to consider them quasi-static fields;
- The Earth does not generate any electromagnetic energy. Energy is only absorbed or dissipated;
- Electric displacement current **D** is quasi-static for all periods. Therefore, it is negligible compared to conduction currents, allowing to treat electromagnetic induction as a diffusive process;

With these assumptions, the Maxwell equations can be rewritten in the following way:

$$\nabla \times \mathbf{E} = -\frac{\partial \mathbf{B}}{\partial t} \tag{4.10}$$

$$\nabla \times \mathbf{B} = \mu\sigma\mathbf{E} \tag{4.11}$$

$$\nabla \cdot \mathbf{E} = 0 \tag{4.12}$$

$$\nabla \cdot \mathbf{B} = 0. \tag{4.13}$$

A diffusion equation in terms of the electric and magnetic fields can be obtained by combining the Laplacian of 4.10 and 4.11 and with the curl of 4.12 and 4.13:

$$\nabla \times (\nabla \times \mathbf{E}) = -\frac{1}{\mu}\frac{\partial}{\partial \mathrm{t}}(\nabla \times \mathbf{H}) = -\sigma\frac{\partial \mathbf{E}}{\partial \mathrm{t}} \tag{4.14}$$

$$\nabla \times (\nabla \times \mathbf{B}) = -\mu\sigma(\nabla \times \mathbf{E}) = -\mu\sigma\frac{\partial \mathbf{B}}{\partial t} \tag{4.15}$$

$$\nabla^2(\mathbf{E}) = \mu\sigma\frac{\partial \mathbf{E}}{\partial \mathrm{t}} - \nabla\left[(\nabla\sigma)\cdot\frac{\mathbf{E}}{\sigma}\right] = \mathrm{i}\omega\mu\sigma\mathbf{E} = k^2\mathbf{E} \tag{4.16}$$

$$\nabla^2(\mathbf{B}) = \mu\sigma\frac{\partial \mathrm{B}}{\partial \mathrm{t}} - [(\nabla\sigma)\times(\nabla\times\mathbf{B})/\sigma\,] = \mathrm{i}\omega\mu\sigma\mathbf{B} = k^2\mathbf{B} \tag{4.17}$$

with the wave number *k* being

$$k = \sqrt{\mathrm{i}\mu\sigma\omega} = \sqrt{\frac{\mu\sigma\omega}{2}} + \mathrm{i}\sqrt{\frac{\mu\sigma\omega}{2}} = (1+i)\sqrt{\frac{\mu\sigma\omega}{2}}. \tag{4.18}$$

The inverse of *k* is called the Schmuker-Weidelt transfer function, *C* (Schmucker 1987). The real and imaginary parts of k are equal. The inverse of the real part is the so-called skin depth, δ (Tikhonov 1950; Cagniard 1953), and corresponds to the depth at which the amplitude of the electromagnetic field attenuates to a factor of e^{-1}:

$$\delta = \sqrt{\frac{2}{\mu\sigma\omega}} = \sqrt{\frac{2\rho}{\mu\omega}} \tag{4.19}$$

where ρ is the electrical resistivity. This expression allows one estimate the penetration depth of electromagnetic (EM) fields for a certain period depending of the conductivity of the half-space.

4.1.1 Magnetotelluric and magnetic transfer functions

The relationship between the horizontal electric and magnetic fields is represented by the impedance tensor **Z** [mV/T]. This tensor is complex, 2*2, and dependent on frequency:

$$\mathbf{E} = \mathbf{ZB} \tag{4.20}$$

Each component of the tensor can be expressed as amplitude and a phase. **Z** is decomposed in the following way:

$$\mathbf{Z} = \mathbf{X} + \mathrm{i}\mathbf{Y} \tag{4.21}$$

With **X** and **Y** representing the real and imaginary parts of the impedance tensor, respectively.

The vertical magnetic field is related to the horizontal magnetic field through the vertical magnetic transfer function **T**, also frequency dependent:

$$\mathrm{B_z} = [\,\mathrm{T_x} \quad \mathrm{T_y}\,] \begin{bmatrix} \mathrm{B_x} \\ \mathrm{B_y} \end{bmatrix} \tag{4.22}$$

With the real and imaginary parts of **T**, respectively, real and imaginary induction vectors can be calculated. The real induction vector is used to infer lateral conductive contrasts. According to the Wiese convention (Wiese 1962), induction vectors tend to point away from conductors, with its amplitude being dependent on the observed conductivity gradient (Jones & Price 1970). The amplitude and angle of induction vectors is computed as follows:

Real amplitude: $\sqrt{Re(\mathrm{T_x})^2 + Re(\mathrm{T_y})^2}$ (4.23)

Imaginary amplitude: $\sqrt{Im(\mathrm{T_x})^2 + Im(\mathrm{T_y})^2}$ (4.24)

Real angle: $\arctan(\frac{Re(\mathrm{T}_y)}{Re(\mathrm{T_x})})$ (4.25)

Imaginary angle: $\arctan(\frac{Im(\mathrm{T}_y)}{Im(\mathrm{T_x})})$ (4.26)

From the impedance tensor the apparent resistivity $\boldsymbol{\rho}_\mathbf{a}$ can be derived:

$$\boldsymbol{\rho}_\mathrm{a} = \frac{1}{\mu\omega}\,|\mathbf{Z}|^2 \qquad [\Omega\mathrm{m}] \tag{4.27}$$

as well as the phase **ϕ** values (Cagniard 1953):

$$\boldsymbol{\phi} = \arctan(\frac{\mathbf{Y}}{\mathbf{X}}) \qquad [°]. \tag{4.28}$$

4.1.1.1 Tensor properties

In a 1D environment electrical conductivity can only vary with depth ($\sigma = \sigma(z)$). Therefore, the diagonal components Z_{xx} and Z_{yy} of the impedance tensor are 0 and the off-diagonal components Z_{xy} and Z_{yx} are equal and symmetric.

In the case of a 2D geological structure, the coordinate system should be aligned with strike of the structure. In this way, the impedance tensor information is solely contained in the off-diagonal components (as in the 1D case). Moreover, in a 2D earth conductivities only change in the vertical direction and in one horizontal direction. Assuming electrical conductivity changes along the y-axis and the strike direction is along the x-axis ($\sigma = \sigma(y,z)$), the Maxwell equations can be decoupled into two different modes. For the first mode, called transverse electric (TE) or E-polarisation, the associated current system with the electric field component E_x is parallel to the strike direction, and the associated magnetic field components are B_y and B_z. For the second mode, called transverse magnetic (TM) or B-polarisation, the associated current system is the electric field component E_y flowing perpendicular to the strike direction, and the associated electric and magnetic fields components are B_x and E_z. Taking the differential form of the Maxwell equations 4.12 and 4.13, two sets of equations describe the E- and B- polarizations:

Transverse Electric:

$$\frac{\partial \mathrm{B_z}}{\partial \mathrm{y}} - \frac{\partial \mathrm{B_y}}{\partial \mathrm{z}} = \mu_0 \sigma \mathrm{E_x}, \tag{4.29a}$$

$$-\frac{\partial \mathrm{E_x}}{\partial \mathrm{y}} = -\mathrm{i}\omega \mathrm{B_z}, \tag{4.29b}$$

$$\frac{\partial \mathrm{E_x}}{\partial \mathrm{z}} = -\mathrm{i}\omega \mathrm{B_y}. \tag{4.29c}$$

Transverse Magnetic:

$$\frac{\partial \mathrm{E_z}}{\partial \mathrm{y}} - \frac{\partial \mathrm{E_y}}{\partial \mathrm{z}} = -\mathrm{i}\omega \mathrm{B_x}, \tag{4.30a}$$

$$-\frac{\partial \mathrm{B_x}}{\partial \mathrm{y}} = \mu_0 \sigma \mathrm{E_z}, \tag{4.30b}$$

$$\frac{\partial \mathrm{B_x}}{\partial \mathrm{z}} = \mu_0 \sigma \mathrm{E_y}. \tag{4.30c}$$

In this geometry, named principal coordinate system, impedances are calculated for the TE mode and the TM mode from the relationships 4.29 and 4.30, depending, of course, on whether the currents flow parallel or perpendicular to strike,

$$\mathrm{Z_{TE}} = \mathrm{Z_{xy}} = \frac{\mathrm{E_x}}{\mathrm{B_y}} \tag{4.31}$$

$$\mathrm{Z_{TM}} = \mathrm{Z_{yx}} = \frac{\mathrm{E_y}}{\mathrm{B_x}} \tag{4.32}$$

with

$$\mathrm{Z_{xy}} \neq -\mathrm{Z_{yx}} \tag{4.33}$$

$$\mathrm{Z_{xx}} = \mathrm{Z_{yy}} = 0. \tag{4.34}$$

In a 3D environment, there is no preferred geological strike. This implies that impedance and phase information from the subsurface is distributed through all tensor components. Because of this, tensors become generic, asymmetrical and complicated to treat.

4.1.2 Galvanic distortion

Accumulated charge at small geological heterogeneities generate time-independent, non-inductive effects known as galvanic distortions. Taking the divergence of 4.5,

$$\nabla \cdot \mathbf{J} = \nabla \cdot (\sigma \mathbf{E}) = \sigma \nabla \cdot \mathbf{E} + (\nabla \sigma) \cdot \mathbf{E} = 0 \tag{4.35}$$

and combining equations 4.3 and 4.6, results in

$$q = -\varepsilon(\nabla\sigma) \cdot \mathbf{E}/\sigma. \tag{4.36}$$

The equation 4.36 implies charge accumulation at the interface between two media of different conductivities in order to guarantee continuity of current flow. The galvanic distortion effect comes from charge accumulation that creates a secondary electric field that may amplify or diminish a primary electric field. This distortion is commonly addressed as "static shift" (Jiracek 1990; Simpson & Bahr 2005). In case of distortion the measured impedance tensor is:

$$\mathbf{Z} = \mathbf{M}\mathbf{Z_r} \tag{4.37}$$

M represents the distortion and it is unknown. Therefore, the amplitude information of $\mathbf{Z_r}$ cannot be obtained from **Z** without further independent information (Smith 1995).

4.1.3 Dimensionality criterion

As mentioned previously, in an ideal 2D case for MT, the diagonal elements of the impedance tensor are zero if the recorded fields are aligned with the principal coordinate system. However, this is normally not the case because the recorded fields are aligned with the magnetic north, without taking the geological strike in consideration.

A rotation **R** of the impedance tensor **Z** is therefore necessary and is described in the following way:

$$\mathbf{Z_r} = \mathbf{R}\mathbf{Z}\mathbf{R^t} \tag{4.38}$$

where

$$\mathbf{R} = \begin{pmatrix} \cos\alpha & \sin\alpha \\ -\sin\alpha & \cos\alpha \end{pmatrix}, \tag{4.39}$$

with a positive α angle applying a clockwise rotation.

To determine the rotation angle α, I used the method described in Becken & Burkhardt (2004) and Becken et al. (2008). This method is based on the fact that, in a 2D environment, linearly polarized primary magnetic fields produce elliptically polarized secondary electromagnetic fields. In case a primary field is oscillating parallel or perpendicular to the geological strike, the secondary field will also be linearly polarized. In this scenario, the impedance tensor columns – also known as telluric vectors (Bahr 1988) - will be also be linearly polarized. Therefore, in simple terms, one can estimate the principal coordinate system by determining the angle α at which the ellipticity of the impedance tensor columns is minimized.

4.2 Magnetotelluric survey location

The MT survey done for this study was set up in the Lower Saxony basin (LSB), in the NW part of Germany and consists of 83 MT stations (Figure 4.2). The length of the profile is 63 km, oriented SW-NE and it was planned so that it is approximately perpendicular to the geological strike direction according to the Tectonic Atlas of NW-Germany (Baldschun et al. 2001). The first 40 stations of the MT profile have a spacing of 500 m while the remaining stations have a spacing of 1000 m. The station spacing was made smaller in the southern end of profile because the Posidonia black shale (PBS) is shallower at that end of profile and outcrops close to stations 4 and 5.

In addition to the MT experiment, seismic and controlled-source (CS) experiments were done under the framework of the GASH (Gas Shale in Europe) and MULTI-EM (Three-dimensional Multi-Scale and Multi-Method Inversion to Determine the Electrical Conductivity Distribution of the Subsurface Using Parallel Computing Architectures) projects, respectively. In the seismic experiment it was possible to resolve the PBS in the first 10 km of the profile. However, this information could not be used in this thesis because stations 1 to 27 were excluded due to high cultural noise. In regard to the controlled-source experiment, no results have been obtained yet.

The MT data field recordings were made from the 15th of November until the 13th of December in the year of 2011. When all MT equipment is properly set up on the field an area of 60 m per 60 m is used. On that note, all stations were deployed on agricultural farms with such areas.

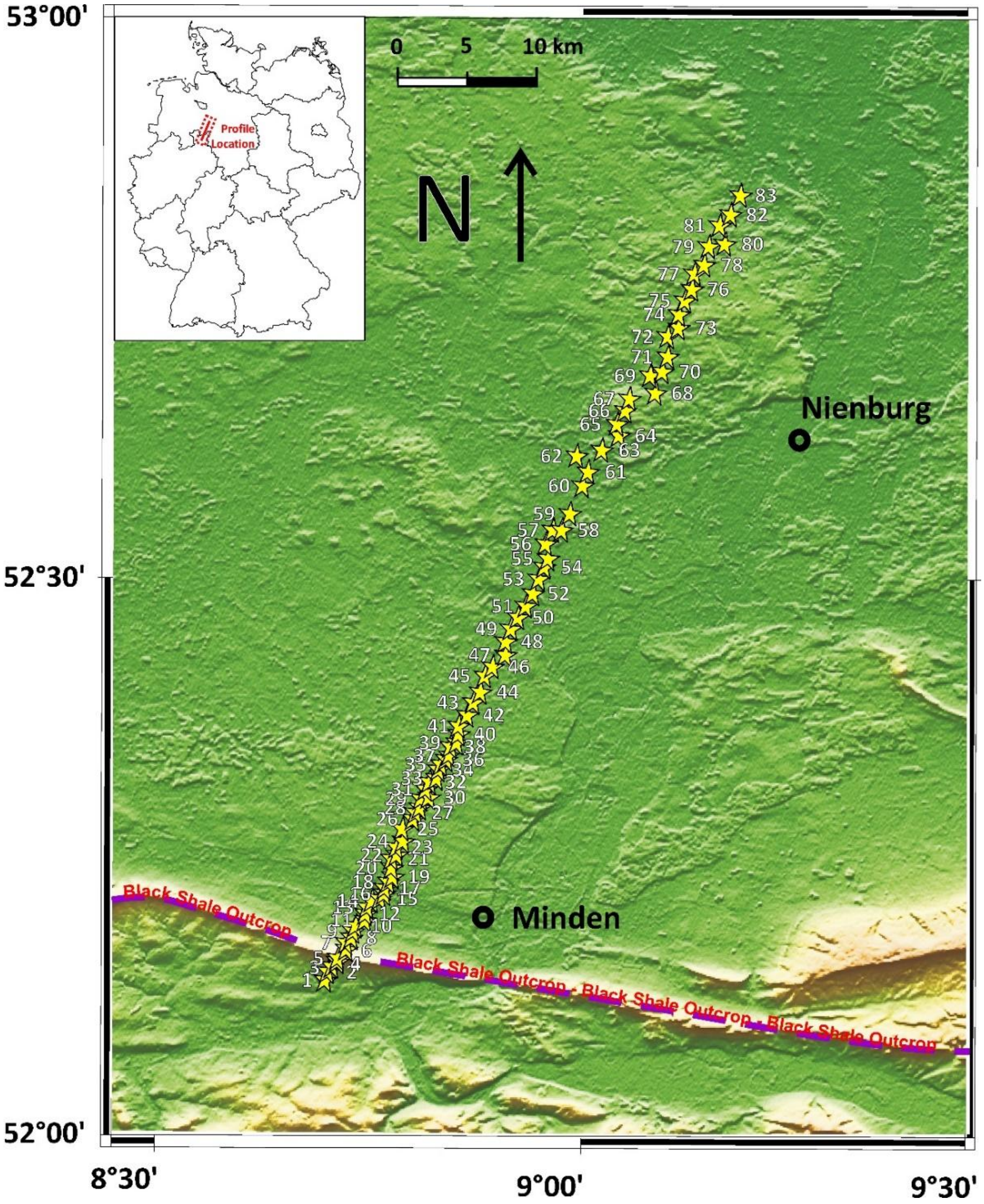

Figure 4.2 - Location of the MT stations. 83 MT stations were deployed along a 63 km long profile crossing the Lower Saxony Basin. The profile has an angle of approximately 28° in relation to the geographical north and is approximately perpendicular to the ESE-WNW geological strike.

The field procedure to measure the natural fluctuations of the magnetic and electrical fields is depicted in Figure 4.3. The electric field potential fluctuations were measured using non-polarizable Ag-AgCl electrodes surrounded by a solution of KCl used to avoid electrochemical noise associated with simple metal electrodes (Petiau & Dupis 1980). The electrodes formed two 60 m long orthogonal dipoles, oriented N-S and W-E, in order to ensure measurable differences. The magnetic field fluctuations were measured with

Metronix magnetic coils (models MFS05, MFS06 and MFS07. See coil information in: http://www.metronix.de/metronix/index.php?id=121). The magnetic fields induce currents in the coils and these are proportional to the strength of the fields after calibration by coil specific transfer functions (Ritter et al. 1996a). Three coils were used, oriented N-S, E-W and vertically. Instrument orientation was so that the x-axis corresponded to N-S and the y-axis corresponded to E-W. All of the measuring instruments were connected with a sensor box at the centre of the MT station. The sensor box was then connected with a data-logger which recorded the measured fields. The data-logger S.P.A.M. IV was used. This instrument allowed the recording of MT data in the period band between 10^{-4} and 1000 s. To achieve this, the electric and magnetic field were sampled with sampling rates of 25000, 6250, 500 and 50 Hz were used. Each MT station remained 3 to 5 days in the field. The data was stored internally in the data-logger and backed up when the MT stations were serviced. All of the recordings were properly time-stamped using a GPS system so that remote reference processing could be made.

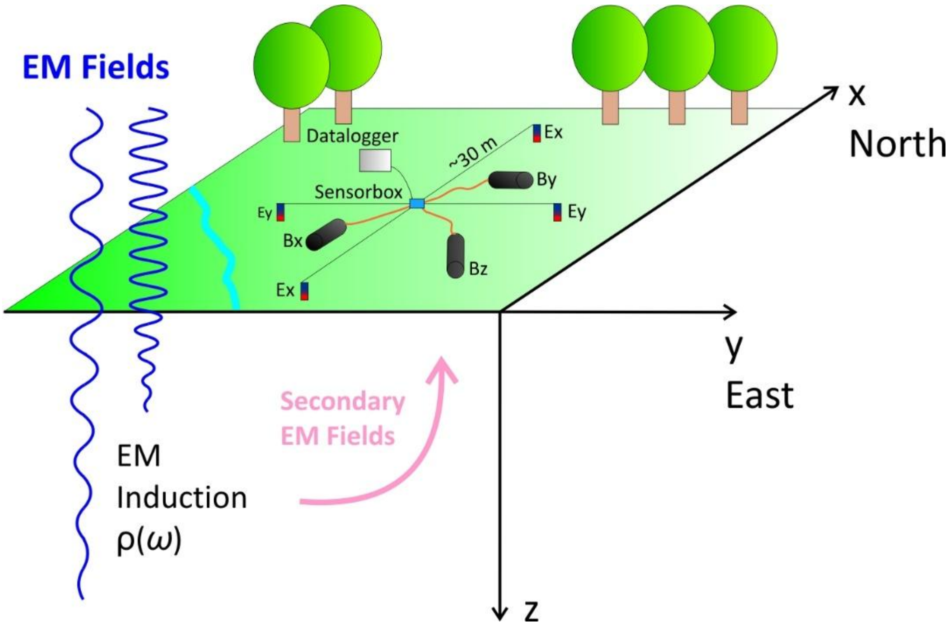

Figure 4.3 - Schematic view illustrating the main components of a MT station. Atmospheric electromagnetic fields (blue) diffuse into the soil and induce electric currents in the subsurface. The secondary field of these current systems contain information about the conductivity distribution and are recorded along with the primary field at the Earth's surface with a MT station. With the depicted MT station the horizontal electric field in the North-South (E_x) and East-West (E_y) directions is measured by two long 50-60m dipoles. The magnetic fields are measured in all three directions (B_x, B_y and B_z) with induction coils.

4.3 Magnetotelluric data processing

The time-series of the GASH data-set were processed with the processing program package EMERALD (Ritter et al. 1998; Weckmann et al. 2005; Krings 2007). All period-dependent transfer functions (impedance **Z** and the vertical magnetic transfer function **T**) were calculated using the entire recorded time-series of the electromagnetic field components. In single station processing, the recorded time series are band-pass filtered into narrow bands and divided into short segments, typically of 128 samples, also referred to as events (Weckmann et al. 2005). These events are cosine tapered and Fourier transformed. The respective Fourier coefficients are calibrated for instrument response functions of the induction coils and divided into sub-bands centred around equally-spaced frequencies on a logarithmic scale. The auto- and cross-spectra are then calculated for each so-called target frequency. Finally, averaged impedance and vertical magnetic transfer functions are obtained by stacking the calculated spectra using the iterative robust algorithm described in Ritter et al. (1998).

4.3.1 EM cultural noise

The impedance (4.20) and vertical magnetic transfer functions (4.22) only represent the responses one would get from a given subsurface in the absence of EM noise. In the ideal case, impedance and vertical transfer function estimates should render smooth apparent resistivity and phase curves and induction vectors along the period range. However, it is very difficult to obtain undisturbed transfer functions in developed countries such as Germany (Szarka 1988). Common EM noise comes, for example, from power-lines, trains, electric fences, corrosion protected pipelines and windmills. Furthermore, nearby metal pipelines, cables or fences serving as passive sources can also induce secondary fields. EM noise is more devastating in the dead-band because of the low energy natural signal (e.g. Iliceto & Santarato 1999; Simpson & Bahr 2005).

The recorded data-set is heavily affected by EM cultural noise. The calculated transfer functions using only single station processing always resulted in scattered apparent resistivity and phase curves and also large induction vectors pointing in erratic directions. Figure 4.4 shows the result of single station processing for station 83. In this figure one can see that impedance and vertical magnetic transfer function estimates show a significant scatter on the whole period range, especially in the smaller diagonal components $\rho_{a_{xx}}$ and $\rho_{a_{yy}}$.

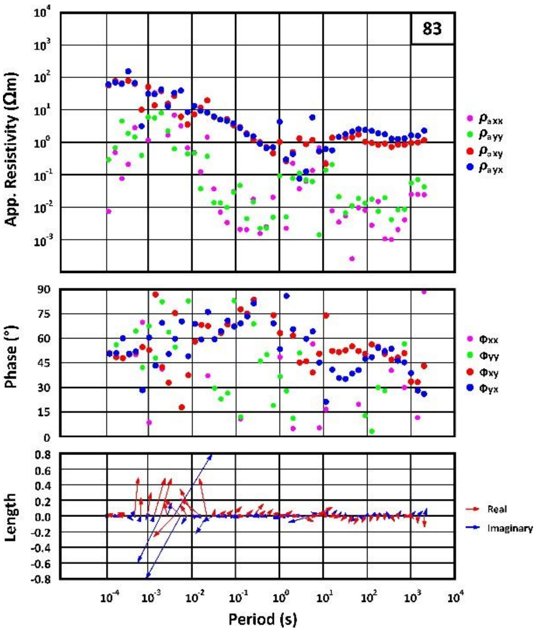

Figure 4.4 - Apparent resistivity, phases and induction arrows from station 83 using single station processing. The data is affected by EM noise particularly at the period band between 10^{-4} to 10^{-2} s and 1 to 10 s in the off-diagonal apparent resistivities $\rho_{a_{xy}}$ and $\rho_{a_{yx}}$ and over almost the entire period range for all other components.

In the following sub-sections I explain the data processing techniques that were applied to the data-set in order to remove or minimize the influence of EM noise from transfer function estimates and discuss corresponding results.

4.3.1.1 Controlled source EM noise

As mentioned before, a CS experiment was conducted simultaneously with the MT experiment. The transmitted signal is present in the time series of several MT stations. For MT purposes this near field signal can be considered as EM noise. To remove its effect, I simply removed time segment of the recorded fields when CS signal was transmitted and thus excluded these parts from further processing. Table 4.3 lists all time segments that were excluded from time-series processing.

Table 4.3 - Date and time segments of CS emissions.

Date	**Start time**	**Stop Time**
19/11/2011	08:28:22	14:31:34
20/11/2011	10:22:20	14:32:56
21/11/2011	07:44:42	14:25:59
22/11/2011	12:26:14	14:29:48
23/11/2011	07:49:55	14:29:06
24/11/2011	10:34:12	12:06:56
25/11/2011	07:45:26	14:32:53
26/11/2011	10:25:10	14:31:56
27/11/2011	07:10:01	14:29:38

The effect of CS signal in the MT transfer functions can be observed, for example, in station 36 (Figure 4.5). It shows a 45° rise of the apparent resistivity curve, phase values close to 0° and very large induction vectors in the period range of 10^{-1} to 10 s (Figure 4.5a). The exclusion of CS affected time-series segments successfully removed the described distortions (Figure 4.5b). However, the apparent resistivity and phase curves as well as the vertical magnetic transfer functions still are heavily affected by other noise sources.

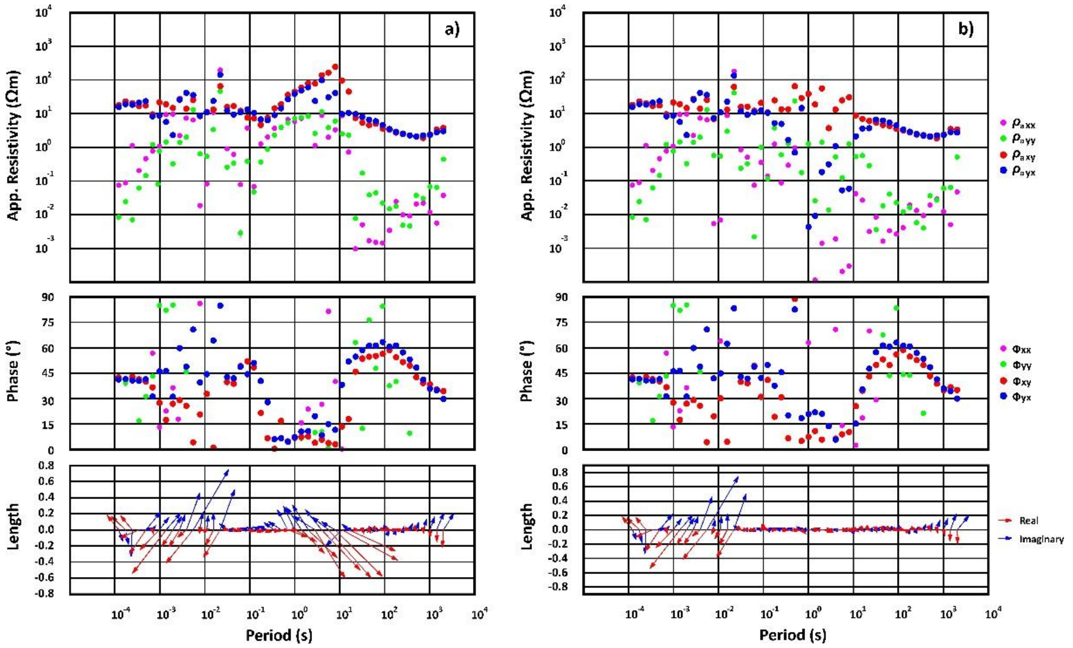

Figure 4.5 - Apparent resistivity, phases and induction arrows at station 36 using single station processing a) with and b) without CS signal. At a period band range of 10^{-1} to 10 s it a 45° rise of the apparent resistivity and very large induction arrows are caused by the controlled source signal. After removing the CS affected time-series segments, apparent resistivity and phase curves as well as induction vectors do not show these disturbances any longer.

4.3.1.2 Remote reference processing

Single-station processing is not always able to remove EM correlated noise. The auto-spectra calculation of the magnetic field has a squared noise term which leads to a downward bias of the apparent resistivity and phases as well as vertical magnetic transfer functions. Furthermore, cross-spectra calculation between the electric and magnetic fields adds another noise term which further hinders the quality of the transfer function estimates (Krings 2007). A common way to replace the affected auto-spectra and to minimize bias effects is to apply remote reference (RR) processing (Goubau et al. 1978; Gamble et al. 1979). RR processing requires a synchronized MT station that is located far away enough so that there is no correlated noise. Under these conditions the MT signal at both the local and reference stations should be correlated but not the cultural noise.

The chosen RR MT station was the GFZ permanent MT station in Wittstock, Germany (Eydam & Munoz 2012). This station recorded all components of the magnetic field and with a sampling frequency of 500 Hz. With this sampling frequency, remote reference processing could be used to improve transfer function estimates for periods below $7.81*10^{-3}$ s.

Figure 4.6 shows the improvement obtained for station 36 using RR processing. The transfer function estimates using single station processing are more disturbed by EM noise in all components. The implementation of remote reference processing successfully improved the quality of the off-diagonal components of apparent resistivity and phase curves and induction vectors for periods below $7.81*10^{-3}$ s.

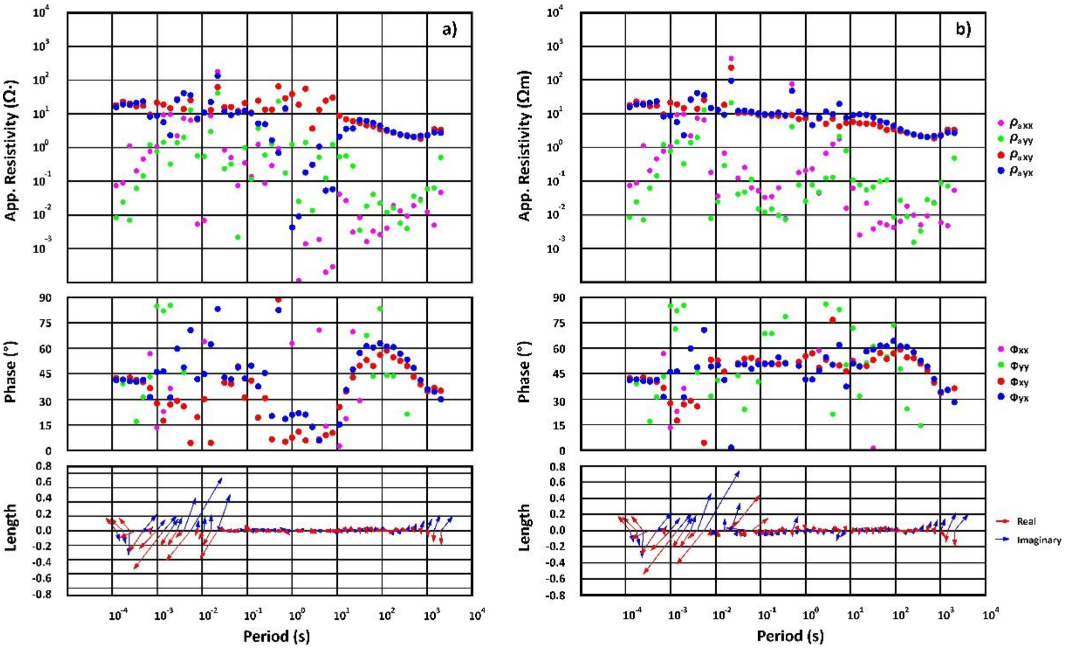

Figure 4.6 - Apparent resistivity, phases and induction arrows from station 36 using single station (a) and RR processing (b). RR processing successfully improved the quality of the off-diagonal components of apparent resistivity and phase curves and induction vectors for periods longer than $7.81*10^{-3}$ s.

4.3.1.3 Delay-line filter

Despite the existence of automated methods, such as RR, it is often necessary to visually inspect time series or power spectra to identify additional noise sources. Thereby, I noticed that the power-spectra of electric and magnetic fields showed several spectral peaks related to EM noise with fundamental periods of $6.02*10^{-2}$, $3.8*10^{-1}$, 1.43 and 15 s and respective harmonics. This is illustrated for station 83 in Figure 4.7. The noise sources are mainly from power-lines, wind-turbines and pipeline anti-corrosion currents. To diminish the influence of high-powered correlated noise on the quality of the transfer function estimates I used a delay-line filter, according to Chen (2008). In simple terms, this filter adds a delayed version of a signal to itself, causing destructive interference of EM monochromatic noise. Figure 4.8 shows the improvement obtained with this filter for station 83. The implementation of the delay-line filter is noticeable as the previously scattered distribution of the off-diagonal apparent resistivity and phase values were replaced by a much smoother distribution along the period range, particularly for phase values below the 10^{-1} s period. However, scatter is still observable in the diagonal components and in the yx-component in a period band between 1 and 10 s. An improvement of the induction vectors was not seen for this particular station, though.

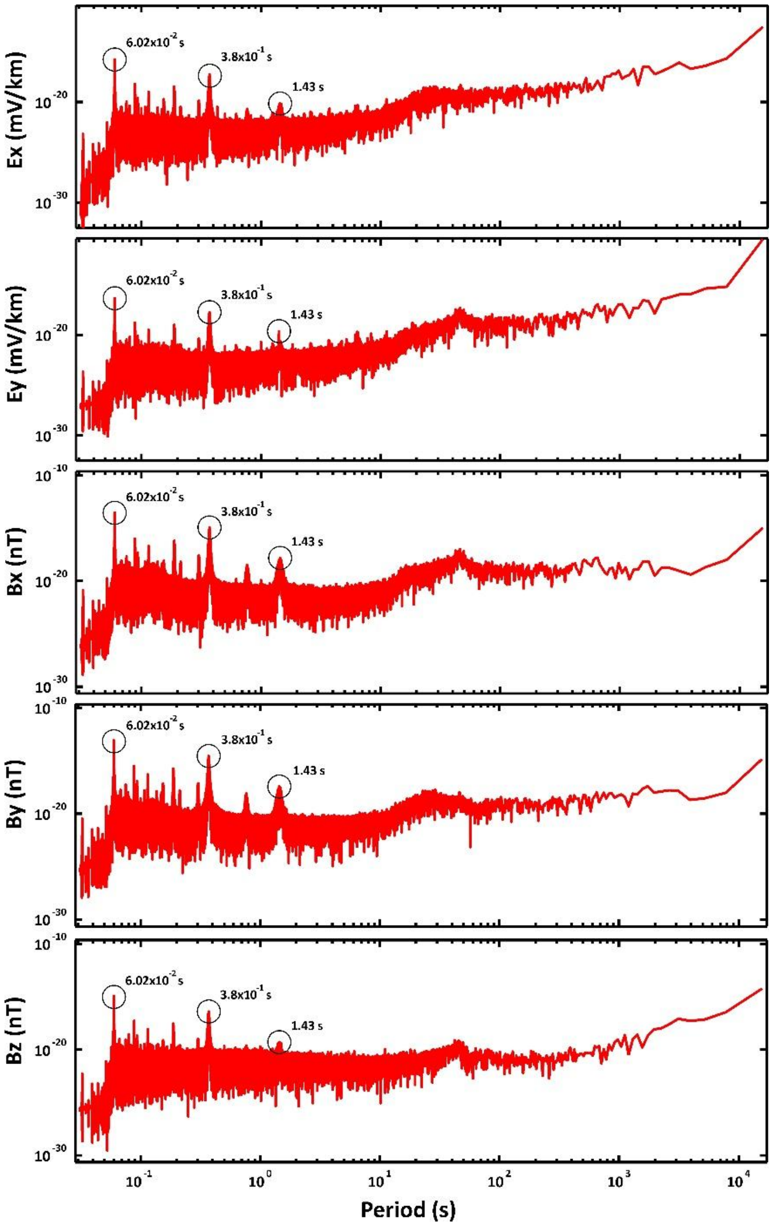

Figure 4.7 – Power-spectra periodograms of the recorded field components for station 83 for the period band $6.25*10^{-2}$ s to DC. Spectral peaks related to noise are observable at fundamental frequencies of 1.43, $3.8*10^{-1}$ and $6.02*10^{-2}$ s and respective harmonics.

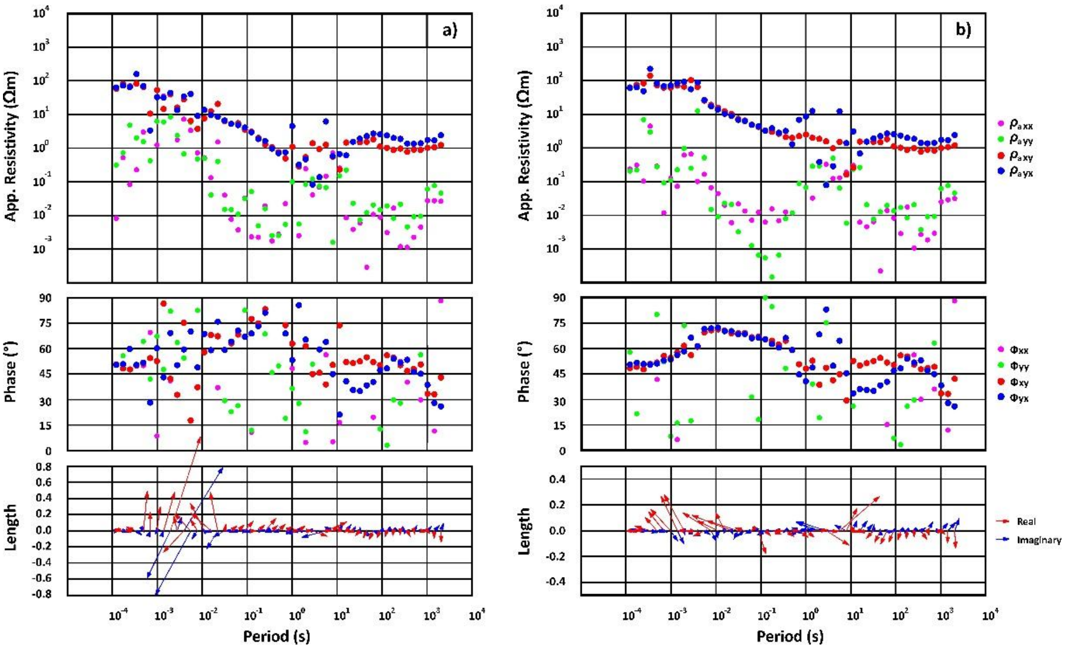

Figure 4.8 - Apparent resistivity, phases and induction arrows from station 83 using single station processing, a) without and b) with including a delay-line filter. The inclusion of the delay-line filter results in a much smoother distribution of off-diagonal apparent resistivity and phase data points along the period range, especially for phases at periods shorter than 10 s period. Significant improvement of the induction vectors is not observable.

4.3.1.4 Frequency domain pre-selection scheme

Remote reference processing and the delay-line showed to be helpful steps in improving the quality of the apparent resistivity and phase curves and the induction vectors. However, for many stations these steps were insufficient. An important tool that revealed to be crucial in improving the data quality of many stations was the SEL4ROB frequency domain pre-selection tool, included in EMERALD and described in Weckmann et al. (2005). This program was mainly developed for when a suitable RR station is not available and to learn about the physical properties of signal and noise. Moreover, one can remove time segments which consist of noise and only keep those that are undisturbed. Therefore, it allows the analysis of a variety of physical and statistical parameters related to the events used in the estimate of the transfer functions that can be described in the following way:

$$X = Z_1 \cdot Y_1 + Z_2 \cdot Y_2 \tag{4.40}$$

where the output channel X is E_x , E_y or B_z and the input channels Y_1 and Y_2 are B_x and B_y, respectively, and Z_1 and Z_2 are the response functions. The parameters are the spectral power density of the electrical [(mV km^{-1})^2 Hz^{-1}] and magnetic [(nT^2 Hz^{-1})] fields (e.g. Jenkins & Watts 1968), the bivariate (e.g. Jones 1979) and partial coherencies (e.g. Jenkins & Watts 1968), the polarization angle of the electric and magnetic fields (Fowler et al. 1967), the response functions (km s^{-1}) and their statistical errors (km s^{-1}).

In order to use this tool to remove noise from MT signal at a given period one has to set specific thresholds to the chosen parameters. Figure 4.9 shows the graphical output of the pre-selection scheme for station 83 at the period of 2 s for output channel E_x and input channels B_x and B_y, before and after selection of events. The spectral power densities of the events in the B_x and B_y (Figure 4.9b, c) components show a spread typical a varying natural signal activity. On the other hand, the power distribution of E_y (Figure 4.9a) shows a periodical ascent and descent over time. At the same event counter, a similar oscillation is seen for the response function errors (Figure 4.9e) and the polarization of the electric field (Figure 4.9h) shifts between 0 and 45°. Further parameters do not show distinguishable patterns that could be correlated with the spectral power density oscillation at E_y.

Apparent resistivity and phase curves and induction vectors of station 83 are shown in Figure 4.10. The yx-component of apparent resistivity and phase curves reveals a disturbance in the period band between 1 and 10s, also noticeable in the induction vectors (Figure 4.10a). Through trial and error process I understood that those events with spectral power density lower than 10^{-14} (mV km^{-1})^2 Hz^{-1} in the E_y channel were causing these disturbances. With exclusion of the affected time segments I could improve the apparent resistivity and phase curves in the yx-component and the induction vectors in the period of 2 s and the remaining data points in the disturbed period band (Figure 4.10b). Ultimately, I used SEL4ROB to improve the overall quality of the apparent resistivity and phase curves in off-diagonal components and also of the induction vectors for station 83.

before selection

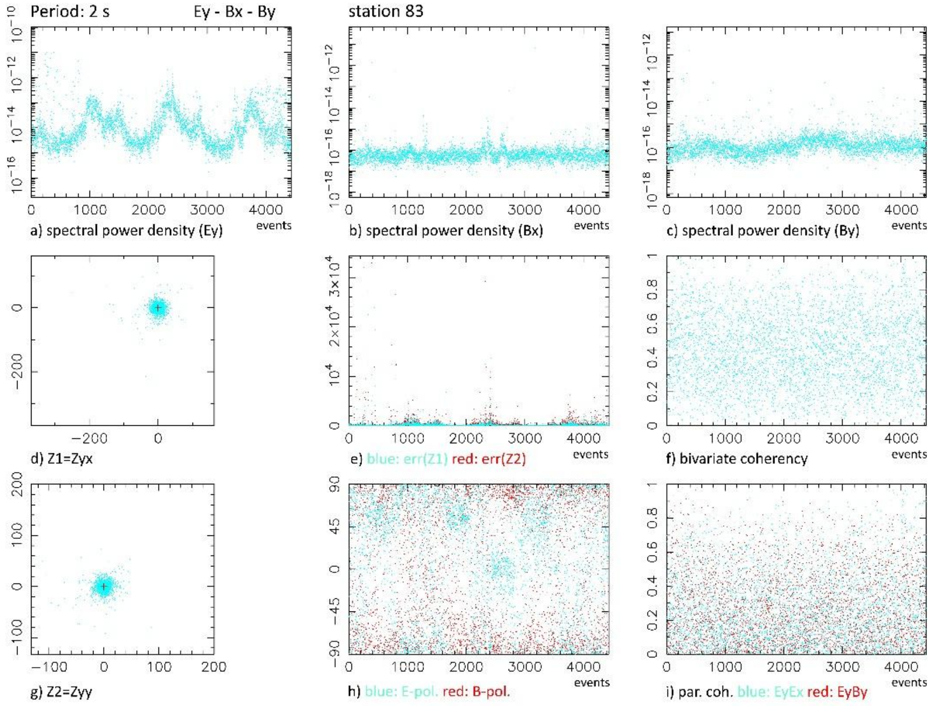

after selection

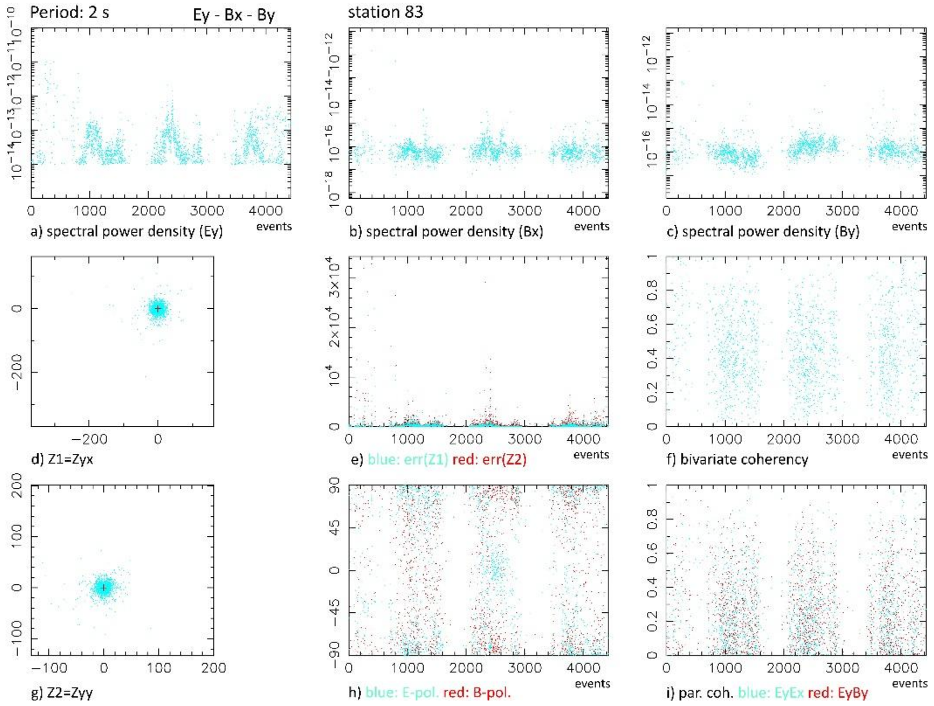

Figure 4.9 - Graphical interface of SEL4ROB for the period of 2 s and channels Ey, B_x, and B_y of station 83. The x-axis of graphs a), b), c), e), f) h) and i) shows the event counter and thus a time axis. The response function plots d) and g) are displayed in the complex plane. Before selection, the spectral power density of Ey shows a periodical oscillation that is not visible in B_x, and B_y. At the same event counter, the response function errors show also minimums and maximums and electric field polarization shifts between 0 and 45°. After selection, the events in a) with a spectral power density lower than 10^{-14} (mV km^{-1})^2 Hz^{-1} were removed. See text for more details.

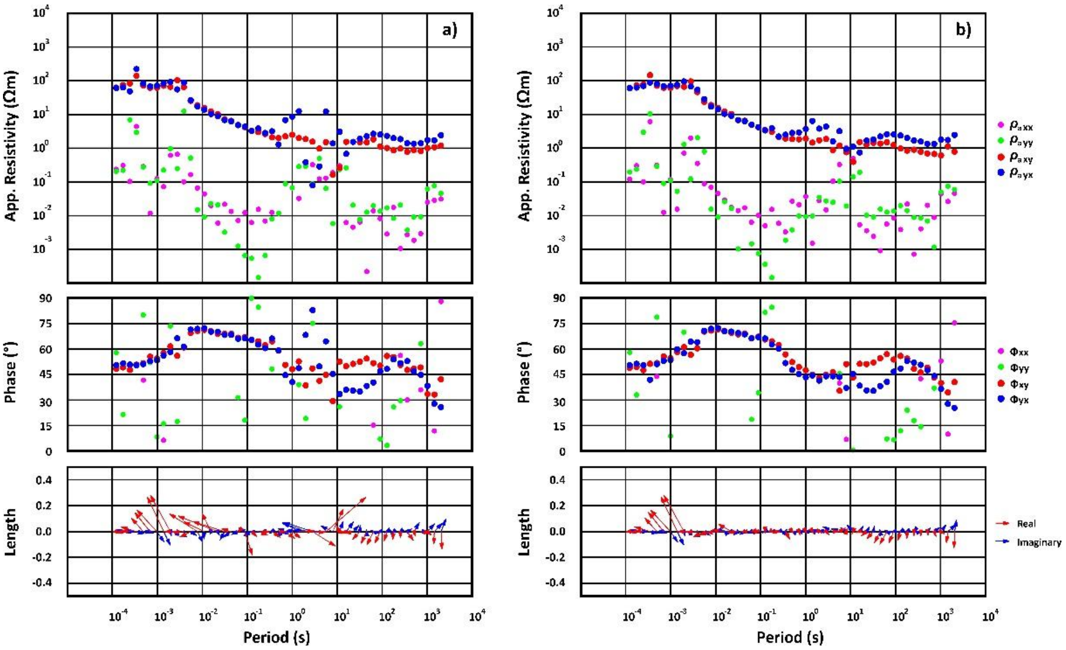

Figure 4.10 - Apparent resistivity, phases and induction arrows from station 83 obtained through single station processing with a delay-line filter a) before and b) after the application of the data pre-selection tool SEL4ROB. The use of SEL4ROB lead to an improvement of off-diagonal apparent resistivity and phase curves as well as induction vectors.

4.3.1.5 Overview

The application of RR processing, delay-line filter and SEL4ROB was helpful in removal of cultural EM noise present in the GASH MT data-set and in the consequent improvement of transfer function estimates of most stations. However, stations 1 to 27 and station 82 could not be included in further analysis because they contain too many disturbances.

4.4 Geo-electric strike estimate

To evaluate if the MT data can be interpreted with two-dimensional (2D) inversion modelling tools, I used the dimensionality and directionality analysis described in 4.1.3. Geo-electric strike estimates are shown in the directional rose diagrams in Figure 4.11. Geo-electric estimates were not considered for periods lower than 1 s because of the dominating influence of local structure.

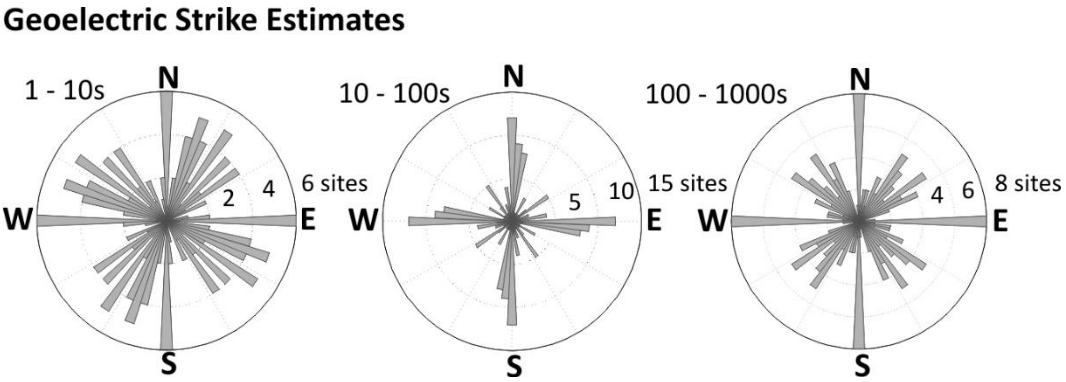

Figure 4.11 - Geo-electric strike estimates indicate regional strike direction of approximately E-W direction. The principal 90° ambiguity can be solved with the induction vectors.

Some scattering is observable and is expected because a clear strike direction cannot be derived for a subsurface with a predominantly one-dimensional (1D) character which would be consistent for a layered sedimentary basin such as the LSB. Furthermore, poor data quality causes larger scatter in the 1 to 10 s period band. However, geo-electric estimates in the 10 to 100 s and 100 to 1000 s period bands indicate predominantly a geo-electric strike direction in the range 0 to 10°, with an inherent ambiguity of 90°. To solve this ambiguity, I resorted to real induction vectors. Real inductions vectors in the same period bands are shown in the directional rose diagrams in Figure 4.12.

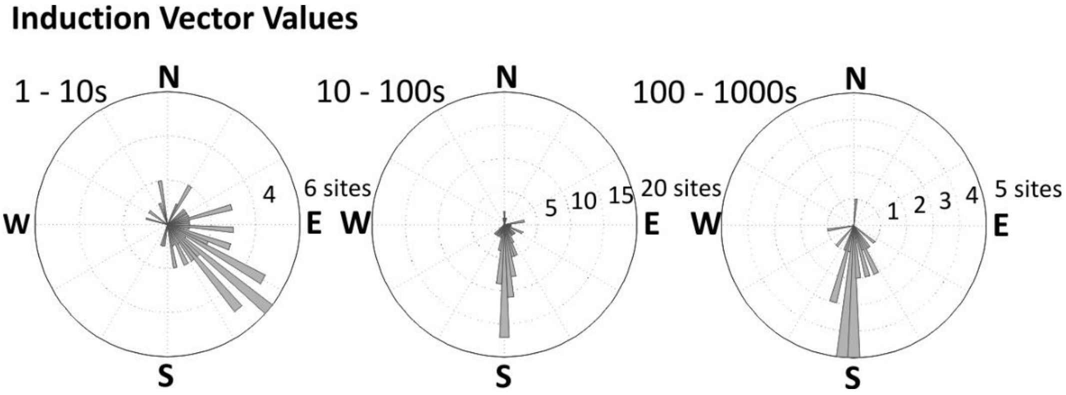

Figure 4.12 - Real induction vectors are predominantly pointing southwards at periods longer than 10 s.

As in the case of the geo-electric strike estimates, the period band of 1-10 s also exhibits scattered induction vectors from which no conclusion can be drawn. However, the rose diagrams in the period bands of 10 to 100 s and 100 to 1000 s show clear southward-pointing induction vectors. From this, the geo-electric strike seems predominantly of E-W for this particular data-set. As the coordinate system in which we installed the stations is matching the geo-electric strike, we applied a rotation of -90° to the data. Subsequently, the xy-component of the MT impedance tensor represents the B-polarization (TM mode) with electric currents flowing perpendicular to strike direction and the yx-component represents the E-polarization (TE mode) with electric currents flowing parallel to strike.

To represent a MT data-set in a compact and clear way, pseudo-sections are often used. Normally, pseudo-sections are used to obtain a first idea into the conductivity distribution along a profile. Figure 4.13 shows pseudo-sections for the apparent resistivity and phase values of the TM and TE modes for those MT stations considered in the analysis. Grey-coloured gaps represent outlier data that was not included in the analysis. Stations 56 to 68 were particularly affected by EM noise and mainly data past 10 s period was considered for these stations.

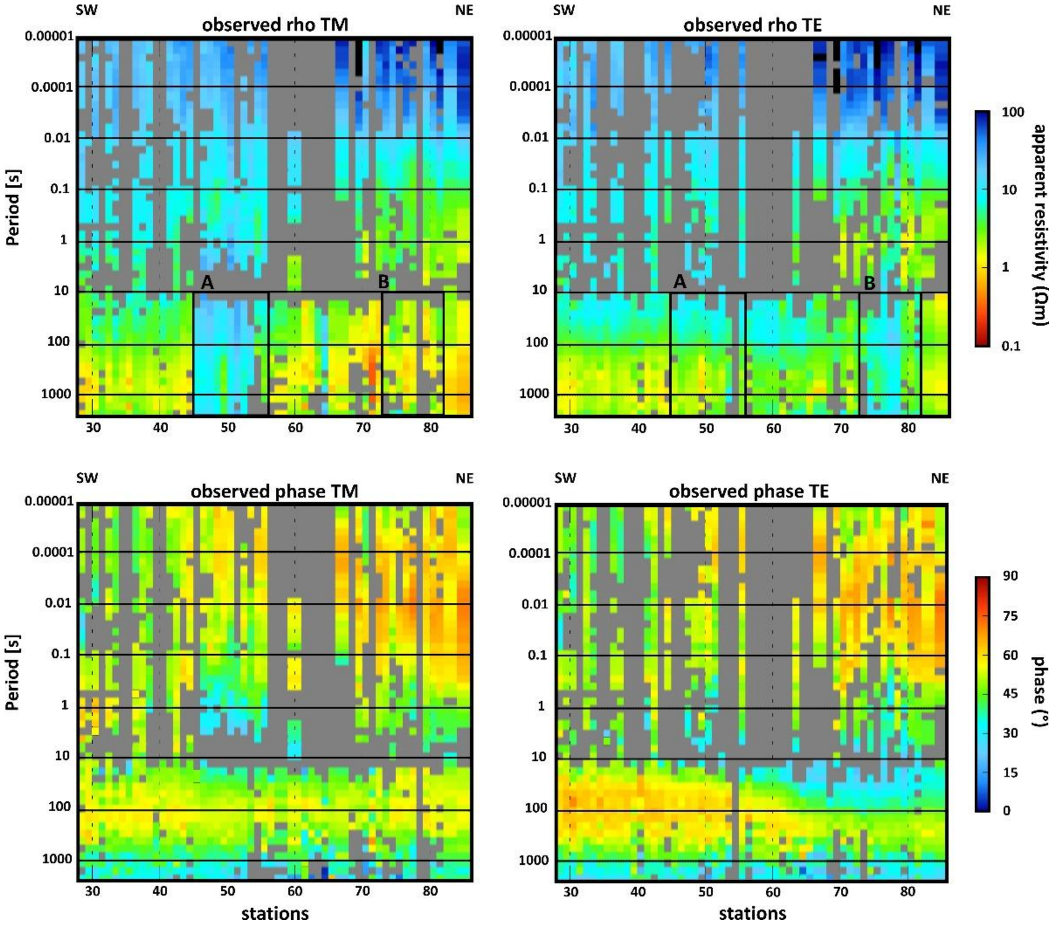

Figure 4.13 - Data pseudo-sections for observed TE and TM apparent resistivity and phase values. Grey colours indicate masked data. Regions marked with labels A and B identify significant differences between TE and TM modes.

Overall, TE and TM modes are quite similar, particularly at higher frequencies, which is consistent with a 1D nature of the uppermost crust. Areas A and B identify those stations in the data-set with 2D effects. TM and TE apparent resistivity values are clearly different for the concerning stations, especially past the 10 s period. There is, however, a distinct change between the south-eastern and north-western profile segments, with stations 28 to 55 denote a less apparent resistivity and phase change in comparison with the stations 56 to 83.

4.5 2D magnetotelluric inversion

4.5.1 Inversion theory

To find an electrical resistivity model that can explain measured EM fields, I inverted the MT data. Contrary to the well-posed forward method where one tries to describe EM fields that are generated by one particular electrical resistivity model, the inversion method is ill-posed (e.g. Zhdanov 2009). This means that from a set of recorded EM fields a wide range of models can be determined with inversion. The mathematical formulation of the inverse problem is well described by, e.g. Tikhonov & Arsenin (1977)

$$\mathbf{d} = \mathbf{f}(\mathbf{m}) + \boldsymbol{\delta}, \tag{4.41}$$

where **d** is the data vector, **m** is the model vector, **f** is the forward operator and $\boldsymbol{\delta} > 0$ represents an error vector. To solve the inverse problem in a two-dimensional scheme I used the non-linear conjugate gradients algorithm (NLCG) by Rodi & Mackie (2001). The NLCG code is implemented in the WinGlink software interface (software version 2.20.10; http://www.geosystem.net). This algorithm seeks to minimize, iteratively, a penalty function

$$\Psi_{\boldsymbol{d}}\,(\mathbf{m}) = \big(\mathbf{d} - \mathbf{f}(\mathbf{m})\big)^T \mathbf{V}^{-1} \big(\mathbf{d} - \mathbf{f}(\mathbf{m})\big) \tag{4.42}$$

where **V** represents the positive diagonal matrix of the data error. The data vector is taken to be the amplitude and phase of apparent resistivity in the TE and TM modes and/or the real and imaginary parts of the vertical magnetic transfer function; the model vector is the log electrical conductivity of the discretized subsurface. At each iteration *n*, the inversion scheme searches for the steepest gradient of the penalty function. The gradient of the penalty function at the iteration *n* is given by

$$\left.\frac{\partial \Psi_d}{\partial \mathbf{m}}\right|_{\boldsymbol{m}_n} = -2\mathbf{J}^{\mathrm{T}}\big(\mathbf{d} - \mathbf{f}(\mathbf{m})\big)^{\mathrm{T}}\mathbf{V}^{-1} \tag{4.43}$$

Where **J** is the Jacobian matrix which describes the sensitivity of the predicted data for small changes in the model. Thereafter, the gradient is used to set up a search direction in the model space for the next inversion step which is given by the direction where the gradient is steepest.

Because the inverse problem is underdetermined a large number of unknown model parameters required by the forward operator is opposed by a much smaller number of data points (e.g. Newman & Alumbaugh 1997). Because of this a regularization term is added to the penalty function to stabilize the inversion process and reduce the number of models that can explain the data,

$$\Psi_{\boldsymbol{r}}(\mathbf{m}) = \Psi_d(\mathbf{m}) + \tau\mathbf{m}^{\mathrm{T}}\mathbf{L}^{\mathrm{T}}\mathbf{L}\mathbf{m} \tag{4.44}$$

where τ is the regularization parameter and **L** is a laplacian gradient operator $(\nabla^2)^2$ which acts on **m** and is used to minimize gradients in the model. The gradient of the penalty function with this term at the iteration n is then given by

$$\left.\frac{\partial \Psi_r}{\partial \mathbf{m}}\right|_{\boldsymbol{m}_n} = \left.\frac{\partial \Psi_d}{\partial \mathbf{m}}\right|_{\boldsymbol{m}_n} + 2\tau\mathbf{L}^{\mathrm{T}}\mathbf{L}\mathbf{m}_n \tag{4.45}$$

The regularization parameter τ increases the smoothness of the model solution at the cost of a higher data misfit.

The regularization operator **L** is chosen such that it is approximately equal to the integration of a weighting function ***l*** over the model area *A* (Mackie 2002):

$$\mathbf{m}^{\mathrm{T}}\mathbf{L}^{\mathrm{T}}\mathbf{L}\mathbf{m} \cong \int l(y,z)\mathbf{L}\mathbf{m}\, dA. \tag{4.46}$$

The weighting function is set to 1.0 by default and is applied to all the horizontal derivatives in a given row since those are independent of depth. It can be used to reduce vertical stretching and/or to reduce roughness that might be in the inversion model. Assuming a uniform grid laplacian operator is chosen, we have (Mackie 2002):

$$l(z) = (z_k/z_0)^{\beta} \text{ for } z_k > z_0 \tag{4.47}$$

$$l(z) = 1 \text{ for } z_k \leq z_0 \tag{4.48}$$

where $\mathrm{z_k}$ is the thickness of the *k-th* row and z_0 the minimum block thickness that is set manually in the software order to delay the start of the weighting function. β is a factor that enhances the effect of the weighting function and it also set manually. With the weighting function the penalty increases on horizontal roughness with depth consistently with the implicit increase in vertical roughness. Finally, one can also increase the penalty on horizontal roughness by multiplying the horizontal derivatives by a factor α that it is as well set manually in WinGlink (Mackie 2002).

The misfit between data and forward response is calculated as a normalized root mean square error:

$$RMS = \sqrt{\frac{\Psi_{\boldsymbol{d}}(\mathbf{m})}{N}}, \tag{4.49}$$

where N is the number of data points. This misfit measure depends on the data error and it is a measure to evaluate the model result for a particular dataset. However, using data errors might lead the inversion to fit the MT data in a non-uniform way. To avoid this one can assign an error floor to all the data and obtain a more uniform fit.

4.5.2 Definition of inversion parameters

The geo-electric strike analysis showed that the GASH MT data-set is compatible with the assumption of a 2D electrical resistivity distribution whose geo-electric strike direction is approximately perpendicular to the measurement profile in an E-W direction. In the following subsections, I explain the different steps that were taken by me to obtain an optimal 2D model of electrical resistivity with the data that was collected.

Using the WinGlink software, I made a series of steps in order to successfully start the 2D inversion modelling process. First, the geographical location of the MT stations was projected onto a straight profile line approximately perpendicular to strike direction. Having defined this profile line, I generated a 2D model space. The model space beneath the profile should be a discretized grid as fine as possible in order to describe the data also as best as possible. However, due to computing limitations it is was not possible. After a trial of inversion modelling with different grids, I defined a model space with 120 rows and 140 columns. The row thickness starts with 5 m and increases by a factor of 1.09. The column width at the profile section was designed so that there was at least one columns between two stations. Outside of the profile section the column width increases by a factor of 1.5. No topography was included.

Having defined the profile section and model space, it is necessary to determine the trade-off parameter, τ. A satisfactory τ should result in a good balance between data misfit and model roughness. In order to find this balance, I carried out a series of inversions with different τ values. For these inversions I used the TE and TM modes of apparent resistivity and phases, but also the real and imaginary part of the T_y component of the vertical magnetic transfer function. A homogeneous half-space model of 100 Ωm was used. Error floors were set to 10% for apparent resistivity, 1.44° for the phases and 0.03 (absolute) for the vertical magnetic transfer function.

Figure 4.14 shows the model results for the different trade-off parameter τ. It is observable that the models with smaller trade-off parameter τ exhibit more structure but have low RMS. Then, the higher the trade-off parameter τ becomes, higher is the smoothness and RMS of the models. Moreover, it is noticeable that the majority of the resolved structures remain present independently of the choice of trade-off parameter τ.

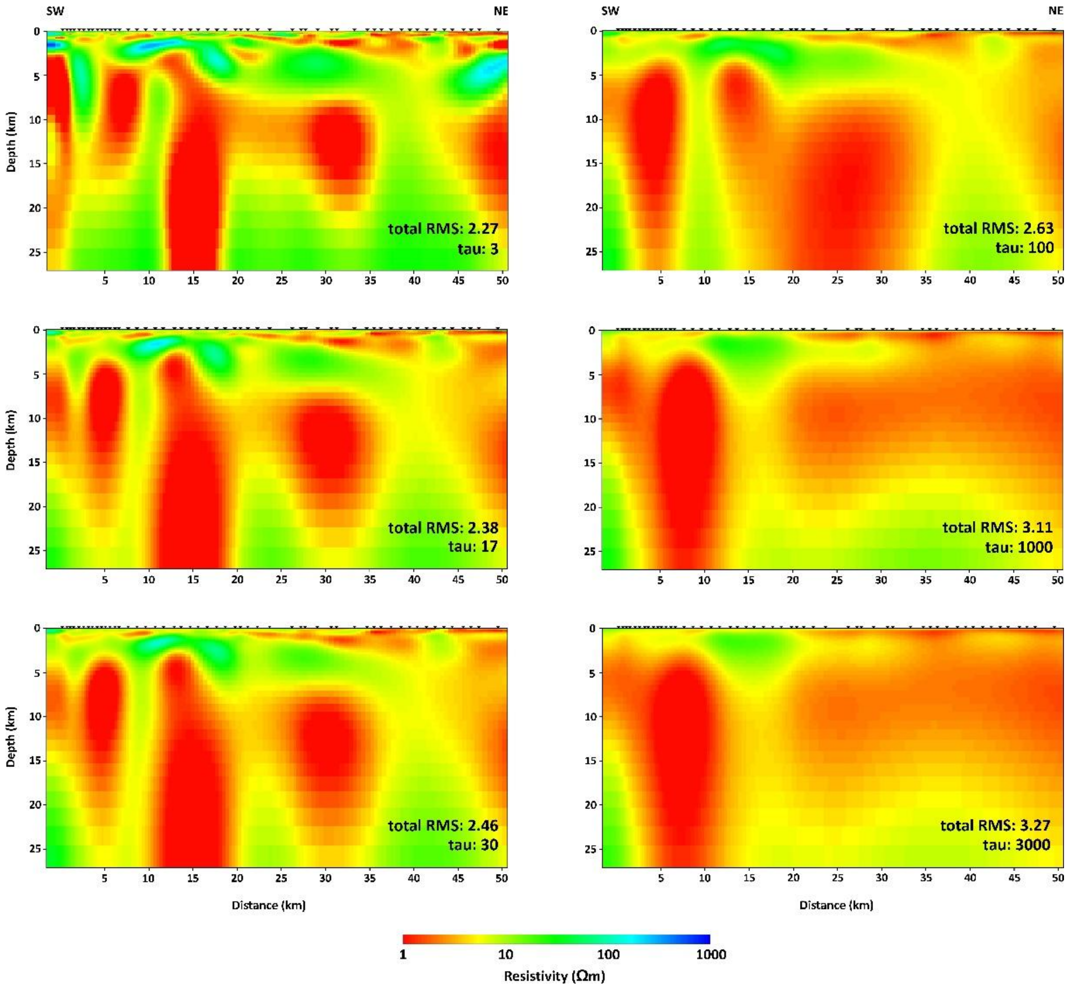

Figure 4.14 - 2D Inversion results using different values for the smoothing parameter τ. The increase of τ increases the model smoothness but also the data misfit (RMS).

In order to find an optimum choice for the trade-off parameter τ, I plotted model roughness versus the RMS data misfit for the different inversion results. The result is the so-called “L-curve” (Figure 4.15). The optimum trade-off parameter τ corresponds to the kink of maximum curvature which marks a satisfactory trade-off for both data misfit and model roughness at the same time. In this case a value of 30 for trade-off parameter was the optimum choice. Having chosen the trade-off parameter τ value, I re-ran the inversion process again until it converged. The inversion process stopped at iteration 240 and total RMS was of 1.96.

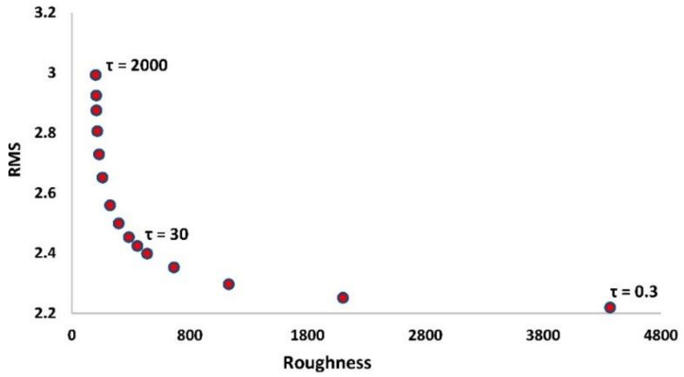

Figure 4.15 - The L-curve is a visual tool to evaluate the optimum value for the trade-off parameter (τ). The optimum value for the regularization parameter is found as a best compromise between model roughness and data misfit. In this case, a value of 30 appears to be a good compromise.

After this, I tested the dependence of the model results with regard to different half-space electrical resistivities. Figure 4.16 shows model results for three different starting electrical resistivities of 10, 100 and 500 Ωm. All inversion results converge to the same solution with the same RMS misfit of 1.96. Therefore, it is reasonable to say the model result is independent of starting electrical resistivity. However, the best value seems to be 100 Ωm as fewer iterations were needed for the inversion to converge to the final solution.

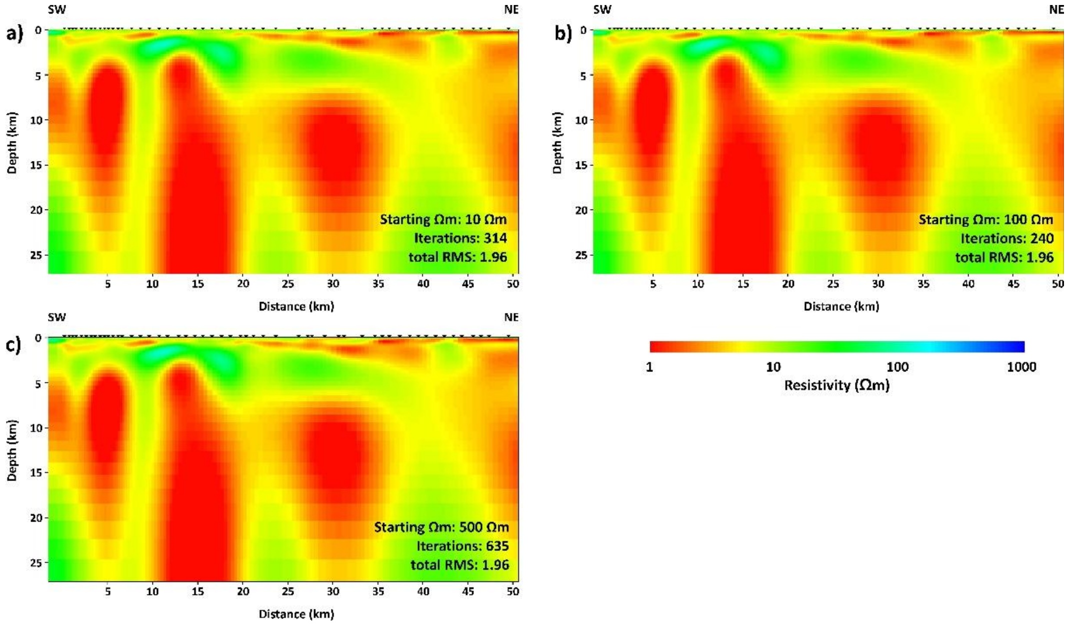

Figure 4.16 - 2D inversion models obtained using starting electrical resistivities of a) 10 Ωm, b) 100 Ωm and c) 500 Ωm. The same inversion parameters were used in all inversions. The model result is similar for all starting resistivities. However, the best value seems to be of 100 Ωm as lesser iterations were needed for the inversion to reach the final solution.

Figure 4.17 shows the preferred model result using the chosen parameters and the calculated total RMS values for each station along the profile. In a first appreciation, the model shows a number of conductive bodies at the top 2 km and below, followed by a more resistive layer which is extending horizontally throughout most of the profile section. Then, vertically extending conductive bodies are found at depths below 3 km. The data fit of this model is generally good. The RMS values at most stations of the profile are found mostly between 1 and 2 and only sites 69 and 78 exceed the value of 3 (Figure 4.17b).

For an individual visualization of the data fit of the MT stations see Figure 7.1, 7.2, 7.3 and 7.4, which are found in chapter 7 of this thesis.

After obtaining the preferred model, I decided to test the robustness of the model by introducing constraints in the model space and changing the smoothing parameters. This work is explained in the following sub-section.

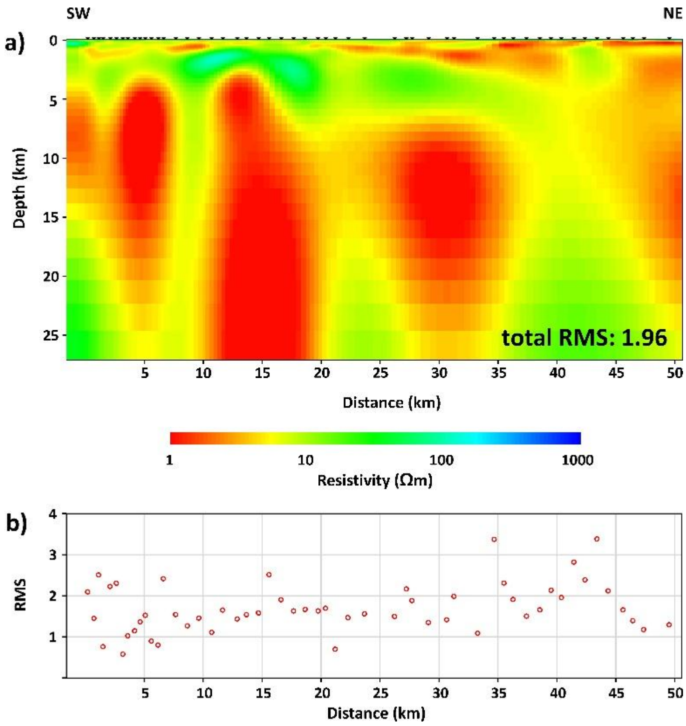

Figure 4.17 - a) 2D inversion result using a smoothness parameter of 30. Two conductive “layers” are observable in the model, separated a more resistive layer, denoting a layered look that is expectable for a mainly one-dimensional sedimentary basin such as the LSB. b) RMS values obtained for each station along the profile.

4.5.3 Robustness tests

I tested the robustness of the model by first testing the resolution of the data. To do this I locked the model space at a certain depth before the inversion was ran. Figure 4.18 shows the comparison between the unconstrained and constrained model. With a trial and error approach, I could establish a depth of 30 km as the limit as to which model variations hardly influence data fit. The result also shows that the depth range extent of the individual conductive bodies is now found between depths of 3 and 20 km (Figure 4.18b). This shows that the vertical extent of these bodies is ambiguous and poorly resolved in the unconstrained model.

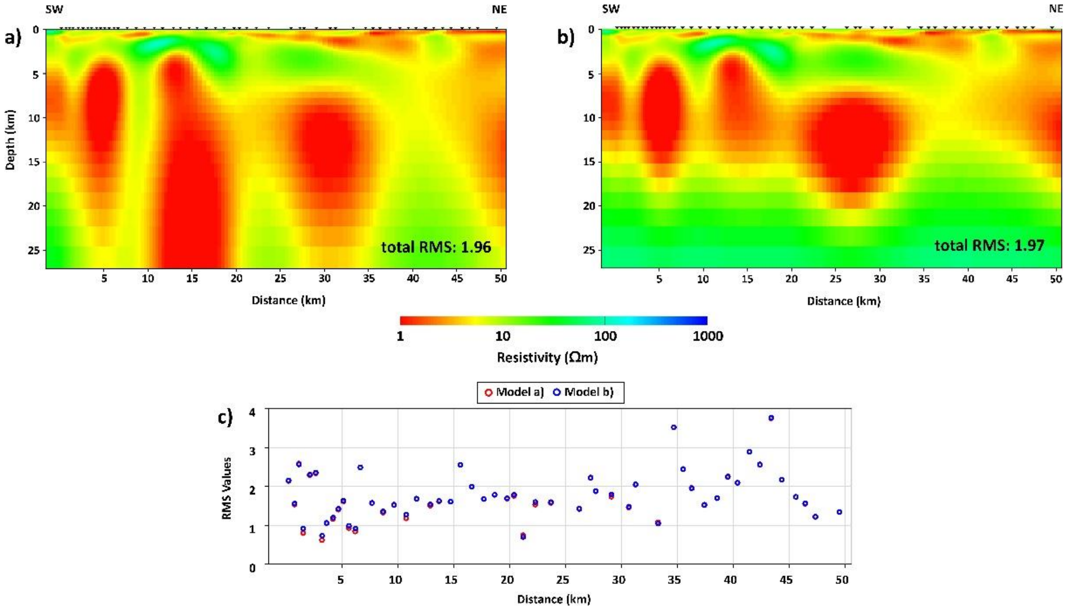

Figure 4.18 - a) Unconstrained 2D inversion model result in comparison with b) 2D inversion model where the bottom resistivity is locked for depths below 30 km and set to 100 Ωm. c) Very insignificant differences between RMS misfit values suggest a data resolution limit of approximately 30 km.

Next I decided to increase the horizontal smoothing in relation to the vertical smoothing. This procedure sets a more layered look to the structures in the model, which is more in line with the geologic setting of the LSB. In order to achieve this, I used the settings used for the model in Figure 4.18b and altered the α and β factors. I tested a range of different combinations of these values and found that the best compromise obtained using factors of α = 2 and β = 3 and setting minimum cell thickness of 500 m as to which the α and β factors influence smoothing.

Figure 4.19 shows a comparison between the model in Figure 4.18b and a model obtained with the same settings plus the mentioned changes of horizontal versus vertical smoothing. As expected, the new model appears smoother in horizontal direction at the cost of generally higher misfits (Figure 4.19c). Nevertheless, the model is similar in its essence. The top 3 km of the inversion model are practically unchanged, while the deeper conductors appear now horizontally connected.

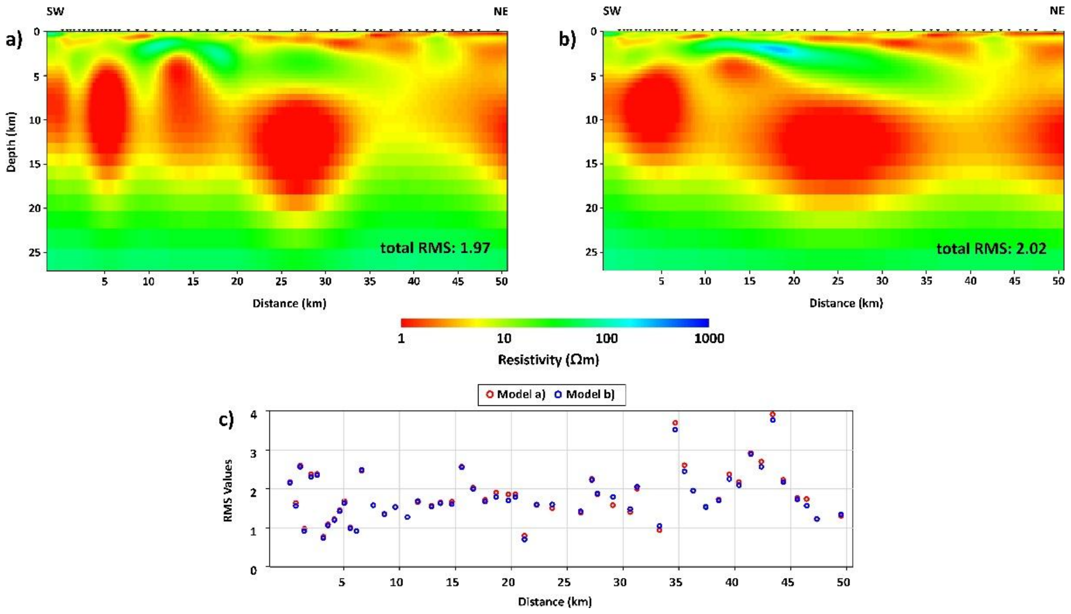

Figure 4.19 - Comparison between a) 2D inversion model result of Figure 4.18b and b) a model with stronger horizontal versus vertical smoothing. c) RMS misfit values increase for most stations as a consequence of the changed horizontal versus vertical smoothing.

Finally, I decided to verify the lateral continuity of the more electrically resistive layer found in-between the electrically conductive features in the model. To do this I locked a horizontal region at 5 km depth towards the northern end of the profile to test if an intermediate resistivity of approximately 20 Ωm could be maintained by the inversion (Figure 4.20). The introduction of the horizontally locked top region (hatched in Figure 4.20b) did not result in higher RMS values, which means that the additional constraint in the model does not contradict the data.

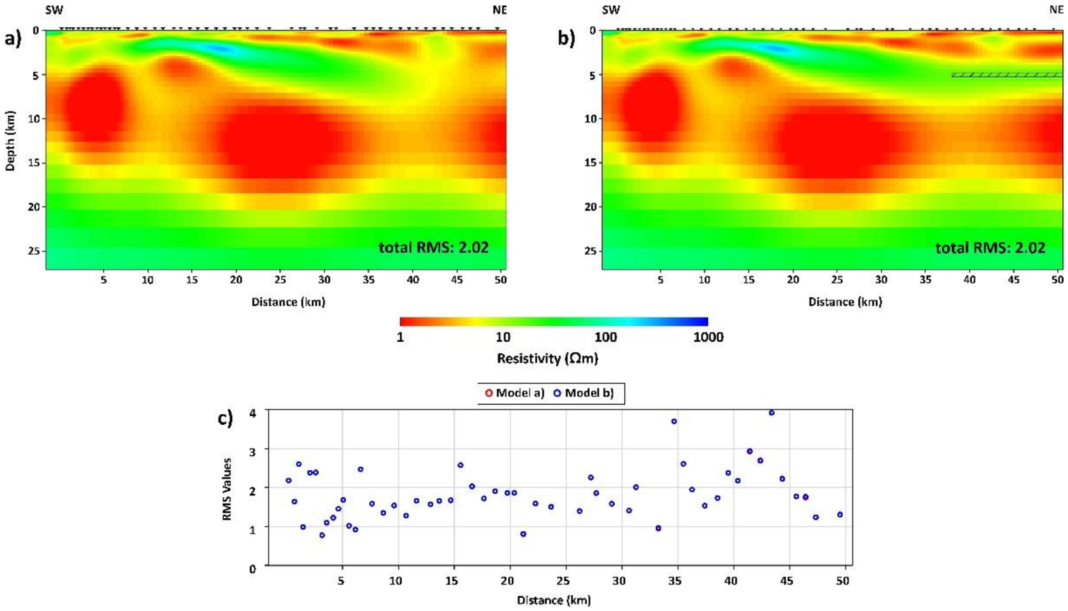

Figure 4.20 - Comparison between the 2D inversion model result of Figure 4.19b a) without and b) with an added constraint located at 5 km depth towards the northern end of the sections marks a region of locked resistivity, to investigate if the inversion could maintain a layer with intermediate resistivity. c) RMS misfit values are practically the same for both model results in spite of the added constraint.

4.5.4 Discussion

For interpretation and discussion, I decided to use the model in Figure 4.20b. Figure 4.21 shows this model in combination with the approximate locations of major faults crossing the MT profile, according to Baldschun et al. (2001). I also included stratigraphic boundaries (top limits) from the 3D basin model carried out by Bruns et al. (2013). These boundaries were modelled using a range of sources: the surface morphology was based on the GEBCO digital atlas (IOC, IHO, BODC 2003); the thicknesses of Pleistocene to Zechstein sediments were obtained from the Geo-tectonic Atlas of NW-Germany (Baldschun et al. 2001), the Zechstein carbonate to Rotliegend, thicknesses were provided by GFZ Potsdam (Maystrenko et al. 2010), and the Carboniferous was derived from the dataset found in Gerling et al. (1999a). The major structures revealed by the preferred 2D model inversion are labelled as conductors C1, C2, C3, C4 and resistors R1, R2.

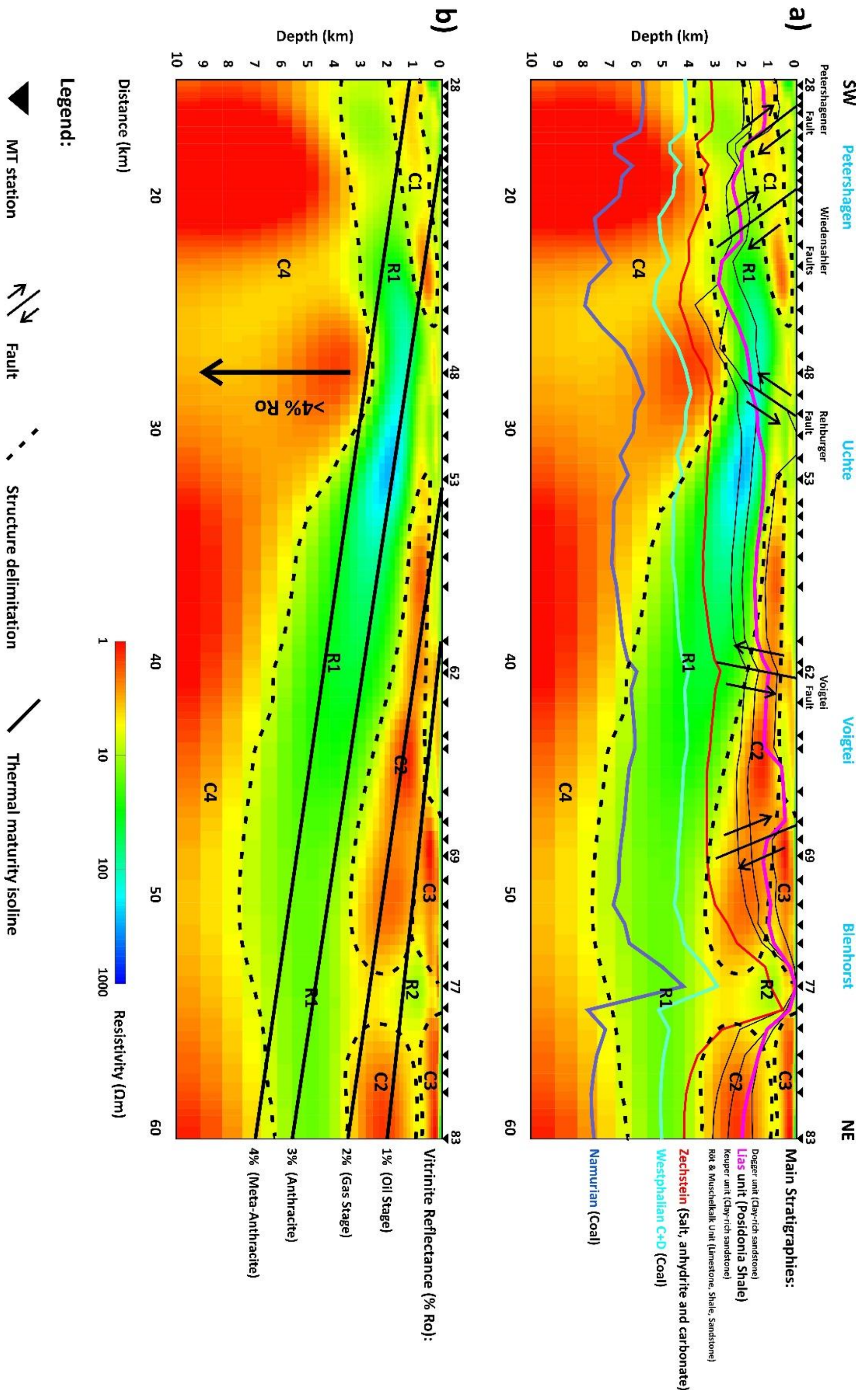

Figure 4.21 - a) The preferred resistivity model including the top boundaries of the different stratigraphies according to Bruns et al. (2013). Main faults intercepting the MT profile are depicted after Baldschun et al. (2001). b) The preferred resistivity model including vitrinite reflectance isolines by Bruns et al. (2013).

Main conductive structures are labelled C1, C2, C3, C4 and main resistive structures are labelled R1, R2.

Conductive features

The occurrence of the top conductors C1, C2 and C3 is probably due to the presence of saline aquifers. Similar conductive features have been modelled with MT in the LSB (Hoffmann et al. 2005, 2008) and throughout most of the NGB (Munoz et al. 2010; Schäfer et al. 2011). Conductors C1 and C2 appear separated, possibly due to a series of normal faults related to the Wiedensahler and the Rehburger fault systems. These fault systems form an intricate horst-graben structure where more impermeable Lower Cretaceous/Upper Jurassic sediments outcrop and form the Rehburg anticline structure (Baldschun et al. 2001). In terms of lithology, the two conductors C1 and C2 could correspond to brine filled, Upper Jurassic clay-rich sandstones. Conductor C2 preserves its upper boundary until the Voigtei fault and becomes thicker north of the station 62 and probably includes deeper sediments. Between stations 62 and 77, the conductor C2 coincides spatially with a region of abundant east-west and southeast-northwest striking faults (Baldschun et al. 2001). Such a brittle deformation zone could be providing the necessary pathways for deeper circulation of saline fluids in porous sediments down until the Upper Triassic Keuper clay-rich sandstones. Overlying conductor C2, the conductor C3 is likely also associated with brines, but now comprising younger Cenozoic clay-rich sandstone sediments, which are more abundant in the northern part of the Lower Saxony Basin (Betz et al. 1987).

Conductor C4 can be explained with the presence of meta-anthracitic and/or graphitized Carboniferous, Westphalian and Namurian coals. These coals have been detected before with MT and described as quasi-metallic conductors (Hoffman et al. 2005, 2008). The thermal maturity anomaly in the LSB has been modelled by Bruns et al. (2013) as well and I have matched their results with my preferred 2D inversion model (Figure 4.21b). According to the corresponding vitrinite reflectance isolines, vitrinite reflectances higher than 4% Ro are predicted for these sediments, which means they are past the meta-anthracite stage of coalification. Conductor C4 reaches its topmost position just under station 48 at depths of approximately 3 km. The stratigraphic boundary predicts a depth of at least 4 km for the Westphalian coals at this station. However, well-log information 6 km off-profile, in relation to site 48, confirms the top boundary of the Westphalian coal sediments at 3 km depth just as it is in the resistivity model (Petmecky et al. 1999). Then, the top boundary of the conductor C4 becomes deeper north of station 48. Due to the decrease of thermal maturity towards the north, the electrical resistivity of the Westphalian coals north of site 48 is probably no longer representative of the conductor C4. The top boundary of the conductor C4 could, however, correspond to the older, deeper Namurian coals which should still be thermally mature enough (reflectance below 4% Ro) to be electrically conductive (Bruns et al. 2013).

Resistive features

The intermediate electrically resistive feature R1 should correspond to different lithology along the model section. This feature should comprise sediments from the Lower Jurassic shales down to the Permian limestones and marlstones up until station 53. Between this station and station 69 I believe there is a transition phase of the sediments representing the resistor R1. North of the station 69, the sediments representing this resistive feature are most likely to be comprised between the Permian limestones and marlstones and the Carboniferous Westphalian coals.

Interrupting the conductor C2, the resistor R2 appears to be associated with the Blenhorst Permian Zechstein salt dome, which is consistent with the Zechstein stratigraphic boundary by Bruns et al. (2013). Salt domes in the NGB are usually very resistive (Buehnemann et al. 2002). However, in the model the electrical resistivity of the salt dome is around 10 Ω·m. Concerning this aspect, the Zechstein sediments are known to be partially composed of anhydrite and carbonates, which together with salt, makes them a rather brittle composite (Munoz et al. 2010). It is possible, therefore, that the extensive faulting in the concerning area has led to the influx of meteoric water into the Zechstein sediments, causing the formation of brine around the salt dome, which, consequently, made its bulk electrical resistivity lower.

The Posidonia black shale

This formation, in terms of mineralogy, the carbonate minerals are most abundant in the PBS (~40%), followed by clay minerals (~15%), quartz (~10%), pyrite (~5%) and others (Littke et al. 1988). Of these minerals the only well conducting ones are the pyrite minerals. However, in the PBS these are commonly found in isolated clusters (Bernard et al. 2013), which are not interconnected. Therefore, pyrite minerals in this rock cannot provide electrical induction at the regional scale.

With regard to the organic carbon found at the grain boundaries of the PBS, its composition and electrical resistivity matter depends on thermal maturity (see chapter 2.3). In this sense, the thermal maturity anomaly found at the LSB provides an interesting study case as to understand the influence of this property on electrical resistivity of the PBS. The PBS is known to be found within the LSB in the depth range of 1 and 3 km (Baldschun et al. 2001). Furthermore, the corresponding vitrinites reflectances range between 0.5 and 4% Ro (between immature and meta-anthracite stages) (Bruns et al. 2013). In the preferred resistivity model, and according to the modelled stratigraphy, the PBS is comprised within the resistor R1, between stations 28 and 62. Then, towards the northern end of the profile it is comprised between conductors C2 and C3. It is observed then that where the PBS is expected to be more thermally mature it is matching a resistive feature in the model and where it is less thermally mature it is matching conductive features. These observations indicate that it is unlikely that any of the conductive features within the same depth range of the PBS are due to its presence. Meaning the thermal maturity range (below 4% Ro) of the PSB and, consequently, the electrical conductivity of the PBS within the profile section are just too low in order to resolve it using MT.

To reinforce the previous conclusion, I present in the next chapter laboratory measurements of electrical resistivity made on PBS samples with thermal maturities partially comparable to those observed within our MT profile section.

5 Laboratory study of the Posidonia black shale

The Posidonia black shale (PBS) sample material was collected from the Wickensen, Harderode and Haddessen wells, located in the so called Hils Syncline structure, just southeast of the Lower Saxony Basin (LSB). Figure 5.1 shows the location of the wells in the Hils Syncline structure within Germany.

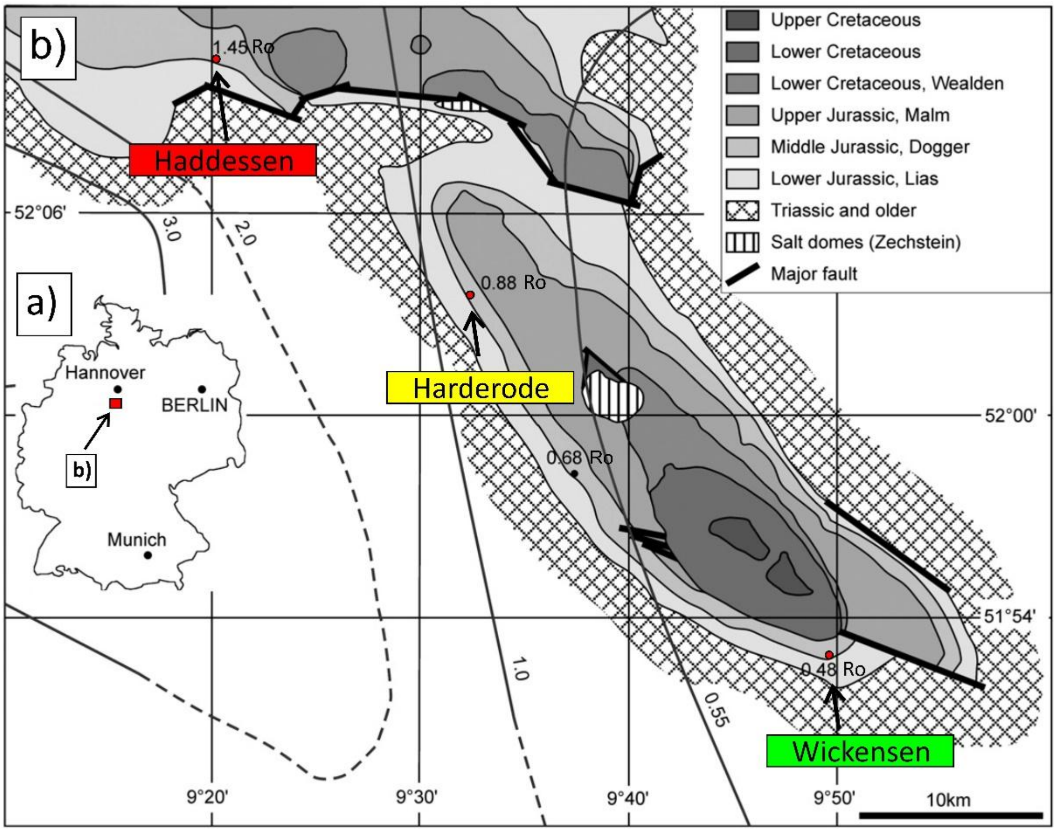

Figure 5.1 - a) Location of the Hils Syncline in Germany. b) Geological map of the Hils Synclince including the locations of the Wickensen, Harderode and Haddessen wells where the Posidonia black shale samples were collected (modified after Klaver et al. 2012) and isovitrinite reflectance contours after Bartenstein et al. (1971) and Koch & Arnemann (1975).

These wells were made to investigate the effects of progressing thermal maturity of the PBS (Mann 1987). The thermal maturity of the PBS in the Wickensen well is in immature stage (0.53% Ro), while it is in the oil producing stage (0.88% Ro) in the Harderode well, and in the gas producing stage (1.45% Ro) in the Haddessen well (Littke & Rullkötter 1987; Littke et al. 1988; Horsfield et al. 2010; Bernard et al. 2012b). Total organic carbon (TOC) is higher for the immature (~10%) samples than for the oil (~8%) and gas producing samples (~5%) (Bernard et al. 2012b). Other detailed geochemical analyses of the Posidonia shale can be found in Leythaeuser et al. (1988); Littke et al. (1988, 1991a); Rullkötter & Marzi (1988); Mann & Müller (1988); Rullkötter et al. (1988); Vandenbroucke et al. (1993). There is vertical heterogeneity of the shale mineral constituents but, in general, carbonate minerals occupy the largest volume (~40%) followed by clay minerals (~15%), quartz (~10%), pyrite (~5%) and others (Littke et al. 1988). Furthermore, the PBS sediments from the three investigated wells show lateral facies continuity (Mann 1987). Geochemical and mineralogical differences between them is largely a result of varying thermal maturation (Bernard et al. 2012b). This allows the study of electrical resistivity of PBS as a function of thermal maturity.

Table 5.1 lists the sample material available for the study. TOC values were provided by the GASH (Gas Shale in Europe) database, which is not publicly available, and measured at the GeoForschungZentrum Potsdam by Dr. Nicolaj Mahlstedt.

Table 5.1 – Information on the Posidonia black shale samples.

Samples	Wells	Depth (m)	Organic content (%)	Vitrinite reflectance (% Ro)
W1	Wickensen	39	9.74	0.53
W2	Wickensen	49	9.79	0.53
W3	Wickensen	58	9.86	0.53
Hr1	Harderode	43	7.22	0.88
Hr2	Harderode	56	11	0.88
Hr3	Harderode	68	7.49	0.88
Hr4	Harderode	76	9.97	0.88
Hr5	Harderode	77	4.8	0.88
Hd1	Haddessen	38	7.5	1.45
Hd2	Haddessen	51	5.04	1.45
Hd3	Haddessen	52	5.54	1.45
Hd4	Haddessen	53	6.12	1.45
Hd5	Haddessen	56	6.17	1.45
Hd6	Haddessen	62	6.02	1.45

5.1 Sample preparation

In order to measure the electrical resistivity of PBS, core samples were prepared parallel and perpendicular to rock bedding. Figure 5.2a shows the drill machine that was used for the core samples. The drill would come from above and slowly perforate the core sample until its end. The core samples were drilled to retrieve cylindrical plugs with a 3 cm diameter. Plugs would then be cut at the ends and made with a length between 3 and 6 cm, depending on the state of the cores (Figure 5.2b). Figure 5.2c shows the appearance and typical dimensions of a prepared PBS sample.

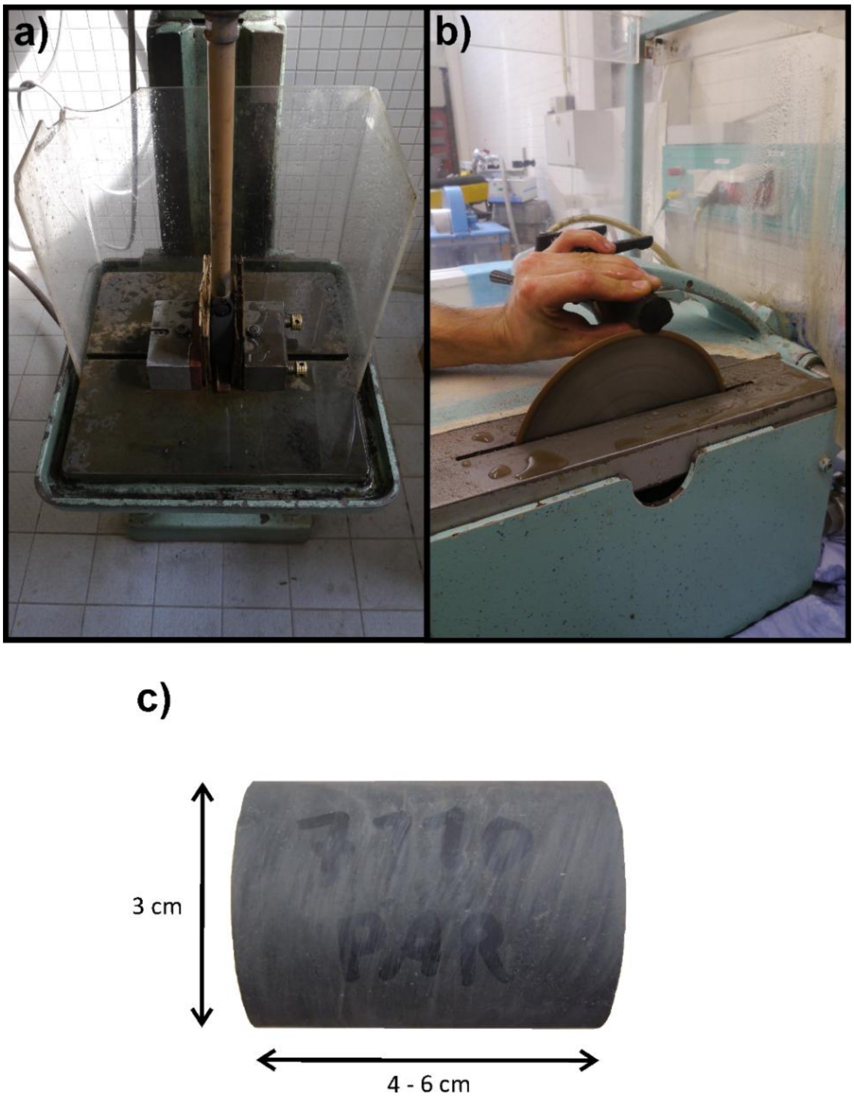

Figure 5.2 - a) Photo of the drilling process of the core samples. b) Photo of cutting process of the core samples. c) Photo of a Posidonia black shale sample and typical dimensions.

After the drill and cutting phases, the samples were put for two-three days in a vacuum cell at a temperature of 60 °C in order to extract fluids contained in fissures and pores (Figure 5.3a). With this procedure a common starting point was set for comparison of results. Afterwards, the samples were soaked with distilled water and aqueous fluids with NaCl concentrations 0.1 and 1 M (mol/L). Before soaking, drying of the samples was repeated to ensure comparability. The saturation of the samples was achieved by submerging the samples into an aqueous solution in a vacuum desiccator with 2 mBar atmosphere (Figure 5.3b). After one week, the samples were removed from the desiccator and electrical resistivity was measured right after. Sample Hr3 and the Haddessen samples did not resist the process of saturation and ultimately got disintegrated (Figure 5.3c). This was possibly due to the clay minerals present in the samples which inflated with the presence of water and cracked the rock into pieces.

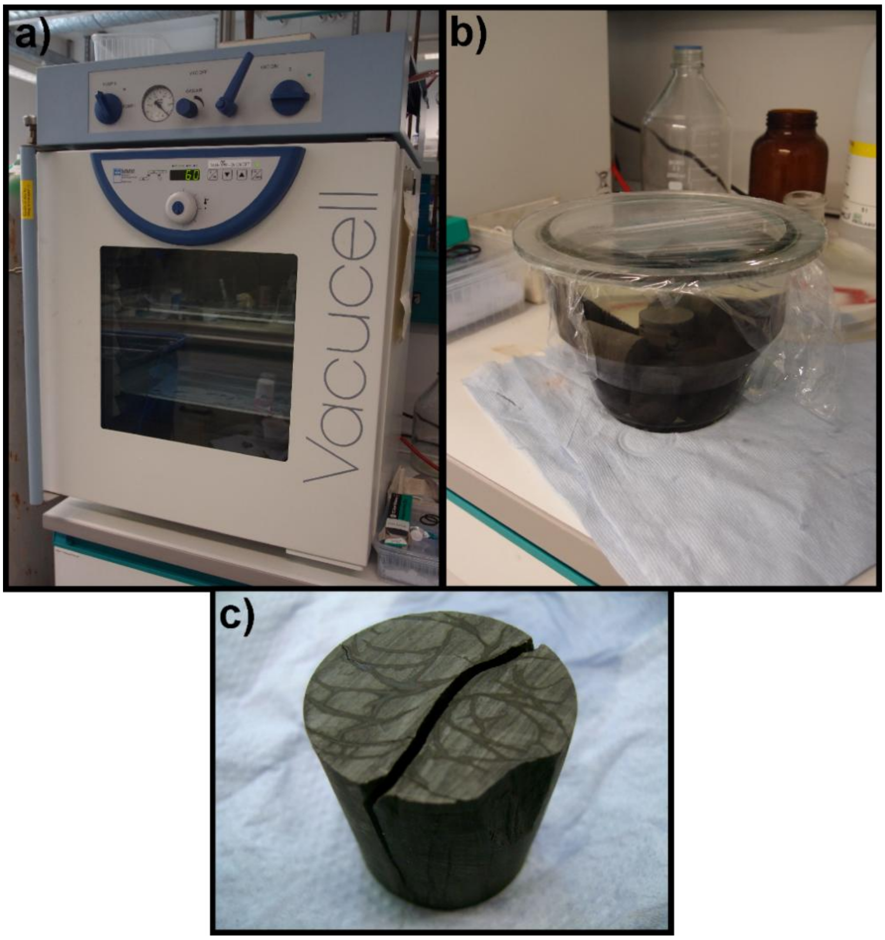

Figure 5.3 - a) Vacuum cell where samples were dried up. b) Vacuum desiccator where samples were saturated. c) Cracked sample after saturation.

5.2 Measuring sample electrical resistivity and porosity

5.2.1 Electrical resistivity

Using Ohm's law (5.1), the electrical impedance Z of a rock sample can be determined, for a specific frequency ω in the following way:

$$V = IZ \leftrightarrow Z = \frac{V}{I} \tag{5.1}$$

with

$$V = |V|e^{j\omega t} \tag{5.2}$$

$$I = |I|e^{j(\omega t-\theta)} \tag{5.3}$$

$$Z = |Z|e^{-j\theta} \tag{5.4}$$

where I is an alternating current, V the applied voltage and θ the phase lag between the current and the voltage. The SI units and dimensions are:

Table 5.2 - Quantities and respective units.

Quantities	**Units**	
V	Volt	(V)
I	Ampere	(A)
Z	Ohm	(Ω)

The electrical impedance can be written as:

$$Z = R + jX \tag{5.5}$$

Where R is the electrical resistance and X the electrical reactance. Electrical resistance equals the magnitude of the electric impedance $|Z|$.

To obtain the electrical resistivity of a cylindrical rock sample, the electrical resistance *R* is multiplied by the cross-section area *A* of the sample and divided by the distance between the potential electrodes

$$\rho_{sample} = R \cdot \frac{A}{L} \qquad [\Omega\mathrm{m}] \qquad (5.6)$$

where ρ_{sample} is the electrical resistivity.

A four-point configuration was used to measure the electrical resistivity of the PBS samples. In this scheme, a cylindrical rock sample is set between two plates serving as current electrodes and in-between the sample two additional voltage electrodes are placed below (Figure 5.4). Polarization effects occurring between current electrodes and the rock sample are avoided with this setup. The voltage electrodes practically draw no current because they have a very high impedance (~10 TΩ). The actual measurements were done with a Zahner's electrochemical workstation ZENNIUM (for detailed information, see: http://www.zahner.de/workstations.html), managed by the Thales software interface (Figure 5.4b).

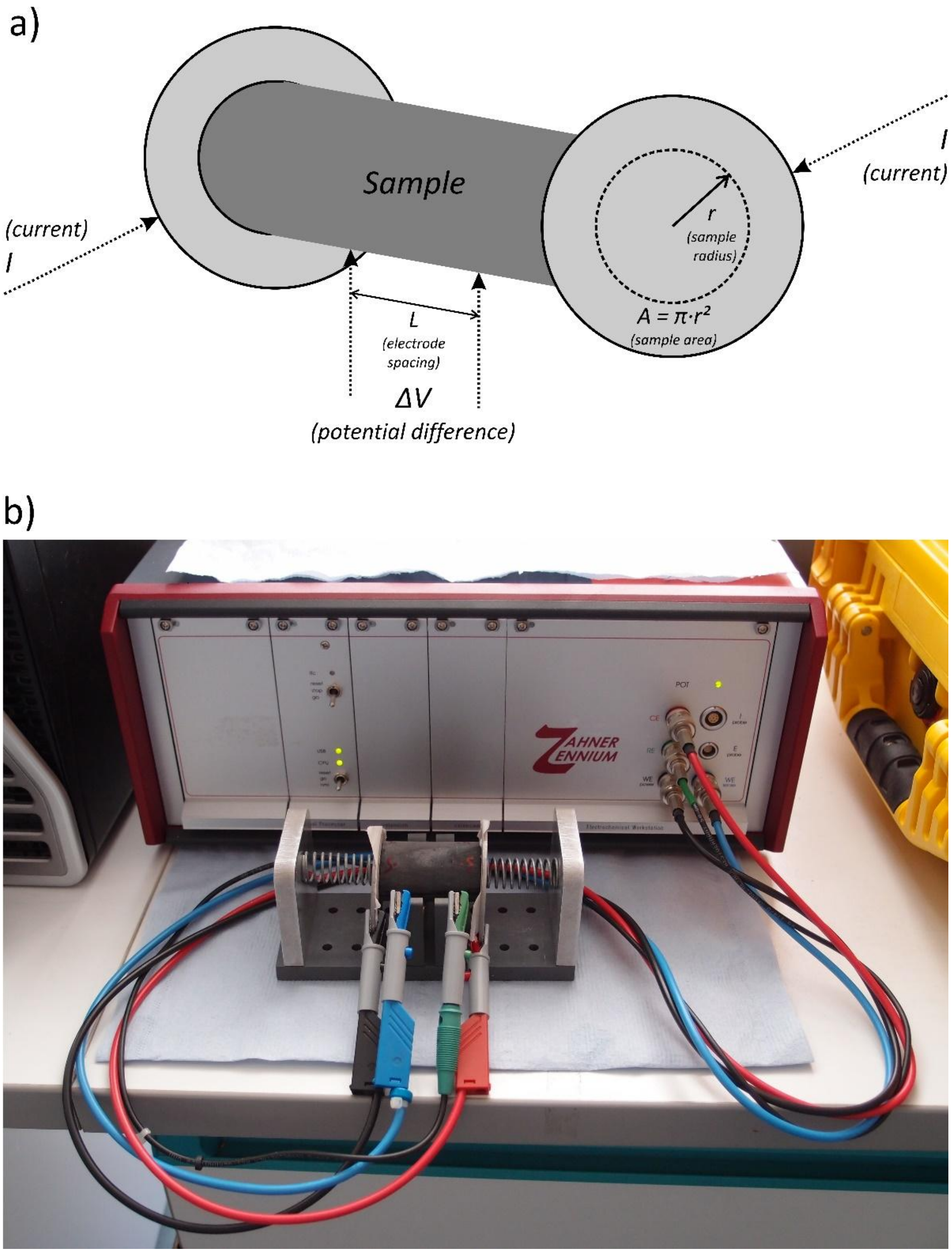

Figure 5.4 - a) Graphical representation of the four-point electric impedance measuring scheme; b) Photograph of the actual apparatus connected to the Zahner electrochemical workstation.

5.2.2 Porosity

Porosity measurements were done on the black shale samples using the Archimedes method. First, the mass of the samples was determined in dry and saturated (with distilled water) conditions. The saturated sample was then weighed suspended under a balance in air, and again while suspended in the fluid with which it was saturated. From these measured weights and known density of the fluid, porosity can be calculated using the following formulas:

$$V_{sample} = \frac{(m_{sat} - m_{sub})}{d_{fluid}} \tag{5.7}$$

$$V_{pore} = \frac{(m_{sat} - m_{dry})}{d_{fluid}} \tag{5.8}$$

$$\phi = \frac{V_{pore} * 100}{V_{sample}} \tag{5.9}$$

V_{sample} is the volume of the sample’s rock matrix, V_{pore} is the volume of the pore matrix reached by the saturation fluid, d_{fluid} is the density of distilled water and ϕ is the porosity of the sample in percentage.

5.3 Results

Electrical resistivity measurements were conducted on PBS under room temperature (~20 °C) and pressure. All measurements were done in the frequency range of 1 Hz to 1 kHz. Figure 7.5, 7.6 and 7.7 in chapter 7 show electrical impedance results within the chosen frequency range for each sample whilst these were dry. Results show that electrical impedance is frequency-dependent for all samples. Most measurements show a 50 Hz disturbance due to surrounding electrical equipment present in the room. The portions of the curves that show frequency independent electrical resistivity are those where conduction currents are dominant, and those portions of the curves with electrical resistivity strongly varying with frequency are where displacement currents are dominant (Olhoeft 1981). Therefore, electrical impedance values at 1 Hz were chosen to determine electrical resistivity of each sample. Table 5.3 lists the results of electrical resistivity measurements at a frequency of 1 Hz and porosity measurements on rock samples from the Hils Syncline.

Table 5.3 - Electrical resistivity and porosity of the Posidonia shale samples collected at the Hils Syncline. Electrical resistivity was measured in parallel and perpendicular to rock bedding using different samples. Porosity results correspond to the porosity measured at the samples which were drilled parallel to bedding.

Samples	**Wells**	**Electrical resistivity (Ωm) ± Standard deviation**				
		Dry		**Distilled water saturation**	**0.1 M NaCl water saturation**	**1 M NaCl water saturation**
		Parallel	**Perpendicular**	**Parallel**	**Parallel**	**Parallel**
W1	Wickensen	2.20E+03 ± 2.32E+02	1.22E+04 ± 3.88E+02	7.53E+01 ± 2.90E+00	3.81E+01 ± 2.64E+00	1.10E+01 ± 7.19E-01
W2	Wickensen	2.37E+03 ± 5.38E+02	n/a	4.39E+01 ± 8.66E+00	1.50E+01 ± 9.85E-01	3.92E+00 ± 3.33E-01
W3	Wickensen	8.72E+04 ± 9.26E+03	n/a	5.87E+01 ± 2.25E+00	3.25E+01 ± 4.44E+00	7.55E+00 ± 1.37E-01
Hr1	Harderode	2.44E+05 ± 7.23E+04	7.45E+06 ± 2.65E+06	4.06E+02 ± 1.28E+01	1.14E+02 ± 1.45E+01	1.76E+01 ± 3.48E+00
Hr2	Harderode	2.54E+04 ± 8.96E+02	3.03E+05 ± 5.95E+04	1.48E+03 ± 4.39E+02	1.04E+03 ± 6.21E+02	1.27E+02 ± 2.79E+01
Hr3	Harderode	3.65E+03 ± 9.65E+02	1.32E+05 ± 3.85E+04	n/a	n/a	n/a
Hr4	Harderode	6.79E+05 ± 6.13E+04	1.26E+07 ± 4.64E+06	7.41E+03 ± 3.15E+02	1.63E+03 ± 8.64E+02	1.21E+02 ± 2.66E+01
Hr5	Harderode	3.81E+04 ± 7.28E+03	1.83E+05 ± 1.30E+04	2.24E+03 ± 6.49E+01	4.65E+02 ± 3.76E+01	1.56E+02 ± 8.09E+01
Hd1	Haddessen	1.49E+04 ± 1.24E+03	n/a	1.30E+02 ± 2.02E+01	n/a	n/a
Hd2	Haddessen	1.03E+02 ± 5.86E+00	n/a	1.87E+01 ± 1.09E+01	n/a	n/a
Hd3	Haddessen	1.64E+02 ± 6.12E+01	n/a	n/a	n/a	n/a
Hd4	Haddessen	1.41E+02 ± 7.99E+00	n/a	7.60E+01 ± 1.03E+01	n/a	n/a
Hd5	Haddessen	2.42E+02 ± 5.68E+01	2.47E+03 ± 1.12E+02	n/a	n/a	n/a
Hd6	Haddessen	5.84E+02 ± 6.83E+01	n/a	n/a	n/a	n/a

Due to the heterogenic constitution of the samples, measurements were done at four different positions for each sample. Each measurement value was different and the standard deviation of electrical resistivity is, at least, an order of degree lower for all samples. This is indication that electrical resistivity does not alter much depending on the position of measurement. Therefore, I consider the arithmetic mean to be a good estimate of the order of magnitude of the electrical resistivity of each sample.

All samples show electrical resistivity exceeding 100 Ωm, and electrical resistivity is consistently higher when measured across rock bedding, which reflects the heterogeneity and electrical anisotropy of the PBS. Furthermore, electrical resistivity does not correlate with the increase of thermal maturity. Samples from the Harderode well exhibit the highest electrical resistivity values, whilst samples from the Haddessen well the lowest. Injection of distilled and saline aqueous solutions leads to a systematic decrease in electrical resistivity, with the highest salt concentrations leading to lower electrical resistivity, at least in the Wickensen and Harderode samples. Figure 5.5 shows electrical resistivity of all samples whilst these were dry and saturated with distilled water and NaCl solutions of 0.1 M and 1 M. It should be noted that some samples, particularly those from the Haddessen well, could only be measured in dry conditions, as fluid injection caused physical disintegration of the samples.

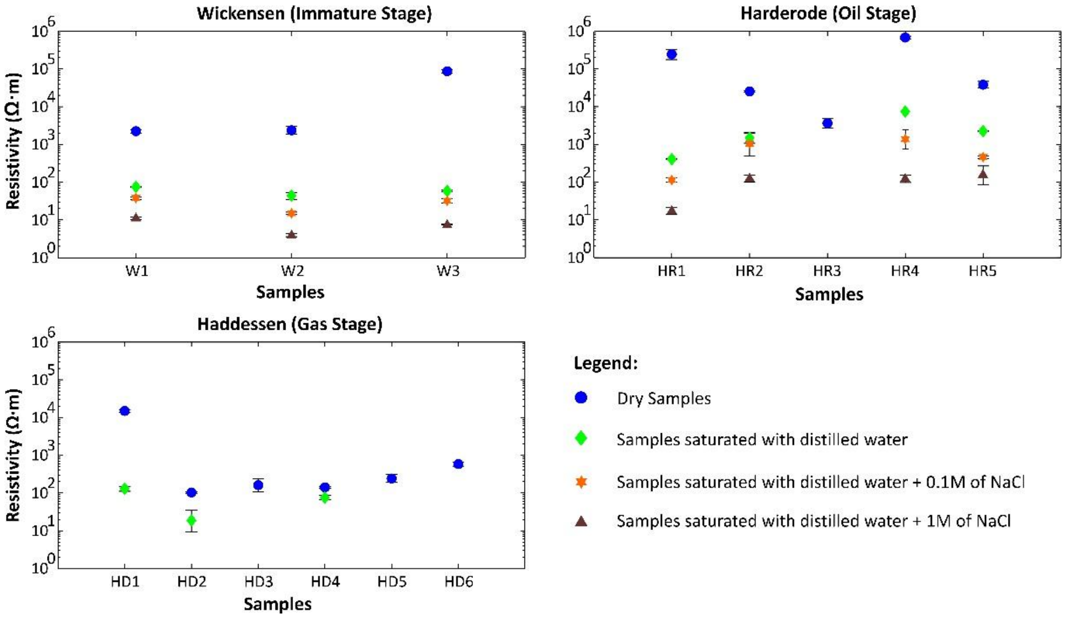

Figure 5.5 - Electrical resistivity measurements of the Posidonia shale samples in dry and wet conditions. In dry conditions, all samples are resistive, with the Harderode well exhibiting the highest resistivity values. Saturation of the samples with distilled water and salty solutions lowers the resistivity of all samples.

With regard to porosity, samples from the Harderode well show the lowest values between 4 and 5%, followed by the Haddessen with values between 6 and 8% and Wickensen samples with values between 10 and 15% (Figure 5.6). A similar trend was observed by Bernard et al. (2013). They determined slightly higher porosities between 10 and 14% for the Wickensen, 4 and 6% for the Harderode and 9 and 12% for the Haddessen. The methods utilized in this study were both gravimetric (Archimedes method) and volumetric (mercury injection). The latter can access pores as small as 2.5 nm and therefore could access the smaller range of pores in comparison to the Archimedes method.

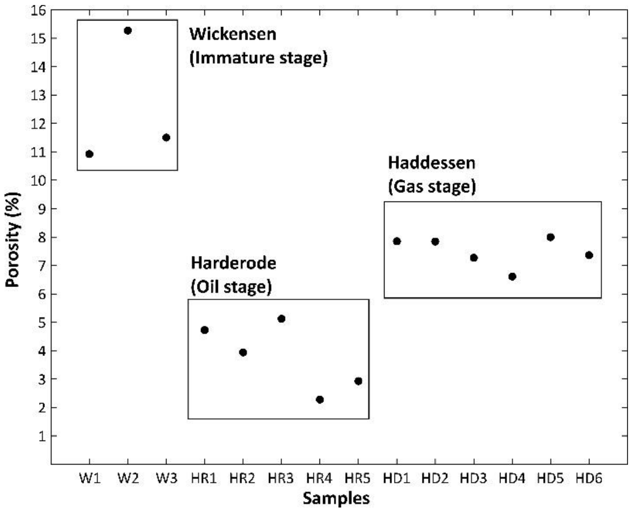

Figure 5.6 - Porosity of the Posidonia shale samples. Samples from the Wickensen well exhibit the highest porosities, those from the Harderode well the lowest.

The electrical resistivity values obtained for samples flushed with distilled water and NaCl aqueous solutions of 0.1 M and 1 M were used to investigate the correlation between electrical resistivity and porosity. Figure 5.7 shows strong and negative correlations between electrical resistivity and porosity with higher porosity being associated with lower resistivity, except for the Haddessen samples. It is possible that a negative correlation would have been seen for the Haddessen well if the remaining samples had not disintegrated during the saturation process.

Electrical resistivity values obtained for samples whilst they were dry were used to investigate the correlation between electrical resistivity and TOC. Figure 5.8 shows only a predominant positive correlation between electrical resistivity with TOC for the Haddessen samples. A positive correlation is also observed for the Wickensen samples but the TOC range is of 0.2% and is rather insignificant for interpretation purposes.

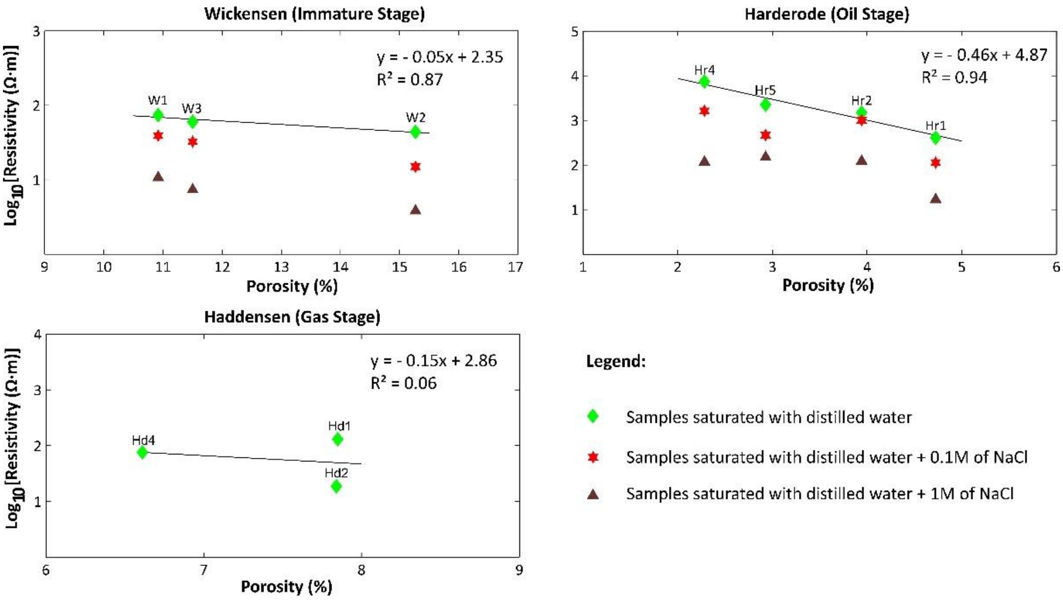

Figure 5.7 - Correlation between electrical resistivity and porosity for the Wickensen, Harderode and Haddessen samples. For the Wickensen and Harderode samples strong and negative correlations between electrical resistivity porosity are observable. The samples from the Haddessen well were generally more fragile and tended to disintegrate when saturated.

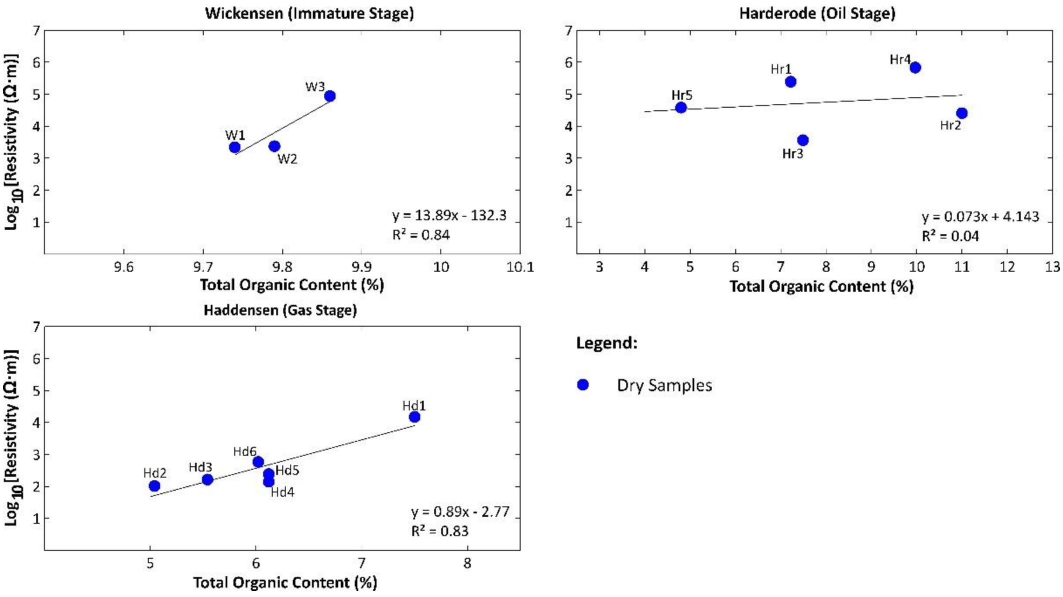

Figure 5.8 - Correlation between electrical resistivity and TOC for the Wickensen, Harderode and Haddessen samples (dry conditions). The samples from the Haddessen well shows a prominent correlation between electrical resistivity and TOC.

5.4 Discussion

Results show that the PBS samples taken from the Wickensen, Harderode and Haddessen wells at the Hils Syncline area has electrical resistivity higher than 100 Ωm when measured in dry conditions. For one, this suggests that the mineral composition (mainly calcite) of this black shale does not possess a well-conductive mineral phase. The only well-conductive mineral is pyrite which in the PBS it is not well interconnected. Figure 5.9 shows examples of photomicrographs from Wickensen and Haddessen samples where one can observe that the pyrite clusters are not interconnected in the rock matrix. Furthermore, the results also indicate that the organic carbon found at grain boundaries of PBS has not yet reached, in any of the wells, a thermal maturity that is high enough to produce low electrical resistivity. Similar conclusions, for example, were drawn for other low-grade maturity organic-rich black shales by Duba (1983); Ahmad et al. (1991); Raab et al. (1998). Although the PBS is not a particularly well conducting rock at the investigated thermal maturities, it could become conductive in areas of the LSB where thermal maturity is closer to the meta-anthracite stage. This is reported in Walters et al. (2014) where a PBS sample with a vitrinite reflectance of 3.6% Ro rendered high electrical conductivity. No electrical resistivity values, however, were disclosed in this study.

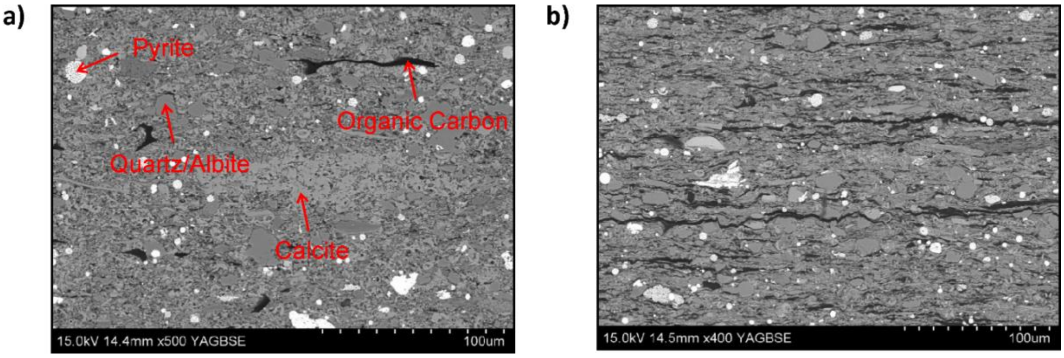

Figure 5.9 - Microphotograph of Posidonia black shale from the a) Haddessen and b) Wickensen wells (modified after Bernard et al. 2013). Note the light grey carbonate patches, dark grey quartz and albite grains, black organic carbon spots and wisps, and the white pyrite clusters.

The electrical resistivity results do not show a linear decrease of electrical resistivity of the samples in the dry state with increasing thermal maturity. As was mentioned in chapter 2.2, increasing thermal maturity transforms organic carbon into hydrocarbons and leaves a carbonaceous residue that can become electrically conductive at the meta-anthracite, semi-graphite and graphite stages. Besides the PBS, Walters et al. (2014) measured the electrical resistivity of five other black shales with vitrinite reflectances of 0.6%, 1.6%, 3.3%, 4.5% and >4.5% Ro and verified that electrical resistivity decreased consistently with increasing thermal maturity. This descent in electrical resistivity was attributed to the increase in turbostratic carbon structures in the black shales with thermal maturity. This process leads to a decrease of bulk electrical resistivity of organic-rich rocks, of course, if the carbon content is high enough and widely connected between grain boundaries. It is possible that black shales in the graphitic stage do not have low electrical resistivity due to low or no interconnectivity of graphite crystals at the grain boundary (Branch et al. 2007). In the case of the PBS from the Hils Syncline, organic carbon is well disseminated throughout the grain boundaries (Bernard et al. 2013). Furthermore, Bernard et al. (2012b) show that the increase in thermal maturity between the Wickensen and Haddessen wells also increases the aromatic carbon structures in the PBS. Therefore, a steady decrease of electrical resistivity between the Wickensen and Haddessen wells would have been expected if organic carbon was a controlling factor of electrical resistivity in the PBS samples.

The reason for the observed trend is not clear. Coincidently, a similar trend has been observed for coals within the same thermal maturity range (Parkhomenko 1967) (Figure 5.10). Electrical resistivity of coals seems to increase from the immature, brown coal stage until they reach the gas coal stage, followed by a steep decrease until the graphite stage. This trend was established after compiling a series of results from different publications concerning the electrical resistivity of coals at different thermal maturities available. According to Toporets (1961), however, brown coal is the most electrically resistive coal type, with an electrical resistivity of the order of 10^{12} Ωm. In regard to this, Parkhomenko (1967) refers that the wide range of electrical resistivity values for different thermal maturities is related to moisture being present in some of the investigated coals. The water content influenced in particular the values of electrical resistivity of coals with vitrinite reflectance below 1% Ro, mainly provided by Dakhnov (1961).

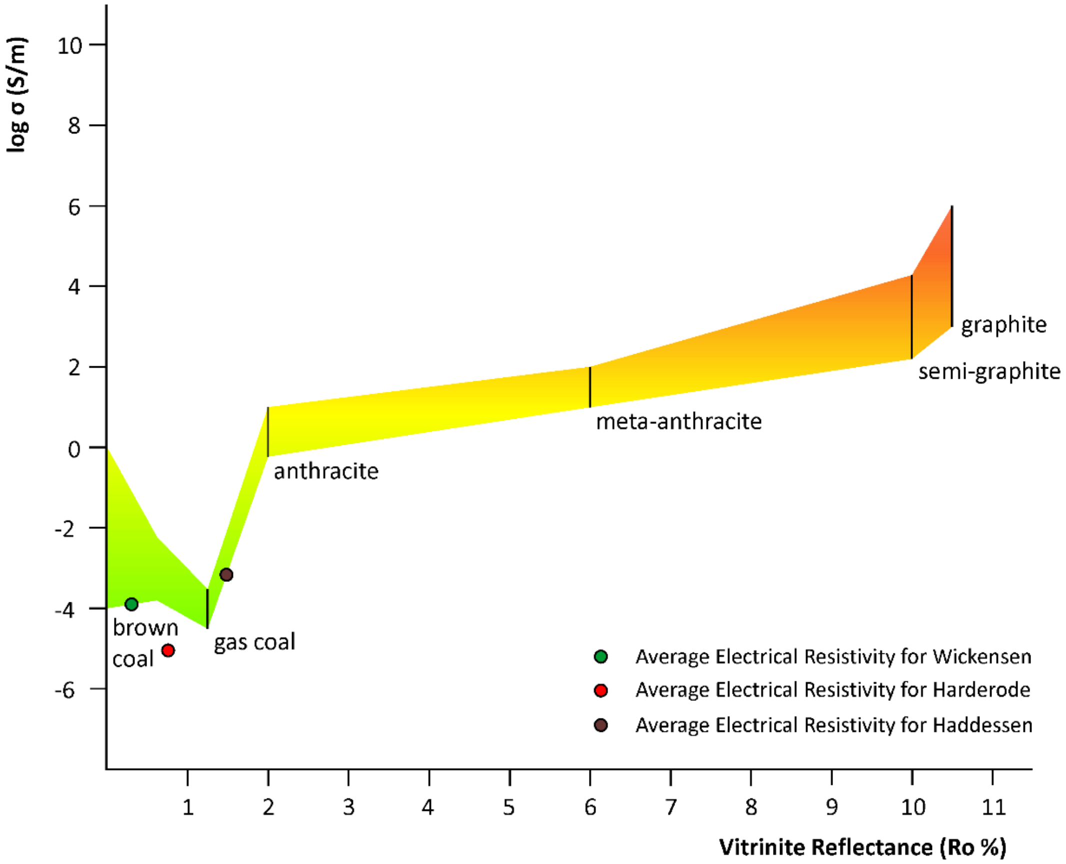

Figure 5.10 - Electrical conductivity range for natural coals as function of vitrinite reflectance (% Ro) (after Parkhomenko (1967) and Teichmüller et al. (1979)). The vertical colour gradient elucidates the electrical resistivity range at different thermal maturities. The average electrical resistivity observed for the Posidonia black shale from the Wickensen, Harderode and Haddessen follows the electrical resistivity trend of coals. Coal ranks are set according to the German DIN coal rank system.

The fact water content is referred as an influential factor of the observed trend of electrical resistivity for coals could be relevant in the interpretation of the observed trend of electrical resistivity between the Wickensen and Haddessen wells. The only trend that was observed and matches that of electrical resistivity is that of porosity. The loss of porosity between Wickensen and Harderode wells and the subsequent gain of porosity between the Harderode and Haddessen wells could be setting the observed electrical resistivity trend in case electrolytic and/or surface conduction was occurring whilst the samples were supposedly dry. However, this would require that water was present in the pores whilst electrical resistivity was measured. If this was the case, it implies the drying process was not entirely successful. An open question is left with the fact that the Haddessen samples exhibit the lowest electrical resistivity values in spite of the Wickensen samples exhibiting the highest porosities. A contribution from rock matrix elements in electric conduction cannot, therefore, be excluded, particularly in the Haddessen samples, in which carbon content seems to be influential.

A consistent result of our investigation is the decrease of electrical resistivity of the PBS samples due to pore saturation with distilled and salty water. This result indicates that electric conduction in PBS in thermal maturity lower than the gas stage is predominantly porosity controlled. Furthermore, strong negative correlations between electrical resistivity and porosity point in that direction, at least for the Wickensen and Harderode samples. Also according to Bernard et al. (2013), a significant fraction of the pore space of the PBS is located inside the clay mineral matrix. Clay minerals are known to have an electrically ‘active’ surface layer that can supply ions in aqueous solutions (e.g. Mitchell & Soga 1993). Enhanced mobility of ions could explain why even saturation with distilled water, which is an insulator, causes a drop in resistivity. The Haddessen samples showed, however, lower decrease of electrical resistivity with distilled water in comparison with the remaining samples. Together with the fact that a positive correlation between electrical resistivity and TOC was observed, it could be that the influence of pore water at the gas stage is starting to become lower in detriment of carbon content.

With regard to MT, these results confirm the difficulty that it is to resolve the PBS formation, at the inspected thermal maturities. Besides not being a well-conductive rock, its electric resistivity dependence on porosity makes it very hard to distinguish from other permeable rock formations such as sandstones which are known to behave in the same way.

Forward modelling

Using the MT and laboratory results, I did a forward modelling test to investigate if an electrically resistive layer of black shale has any chance to be resolved in sedimentary basin such as the LSB. Figure 5.11 shows a layered resistivity model with a 100 m thick layer at 1500 m depth representing the PBS formation. This model was based on the two-dimensional inversion model result seen in Figure 4.17. I assigned a 100 Ωm value to the PBS which is the lowest value measured with the samples. Figure 5.12 shows the forward response obtained with and without the layer PBS. The responses are virtually identical (if no noise is added). Thus, under these circumstances, identifying the PBS formation by its electrical properties and using standard 2D inversion approaches is evidently not possible. Furthermore, where the PBS contains free and adsorbed hydrocarbons in the pore matrix – and knowing these are electrically resistive – one could expect an analogous electrical resistivity contrast as observed in Figure 5.11. Moreover, the laboratory study also showed that electric conduction of the PBS in the immature and hydrocarbon generation stages is predominantly porosity controlled. Because of this, it is difficult to distinguish this formation from other permeable formations of the LSB, such as sandstones, if these are water saturated.

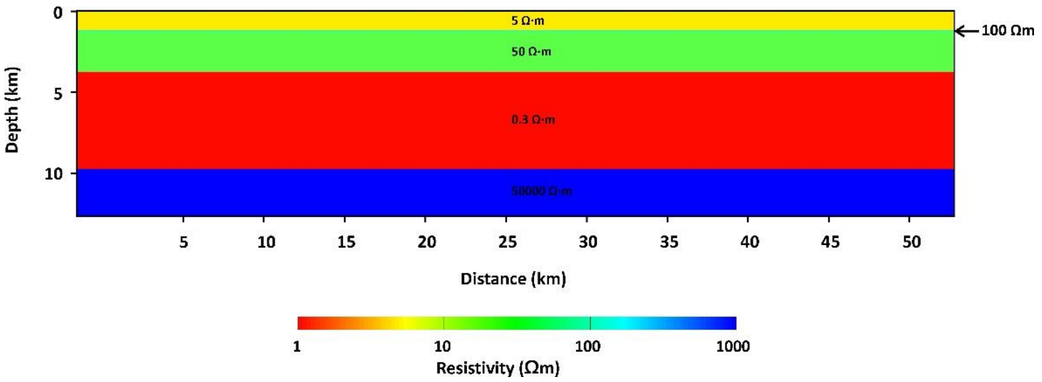

Figure 5.11 - Layered resistivity model based on inversion result seen in Figure 4.17. The Posidonia black shale is represented as a 100 Ωm, 100 m thick layer.

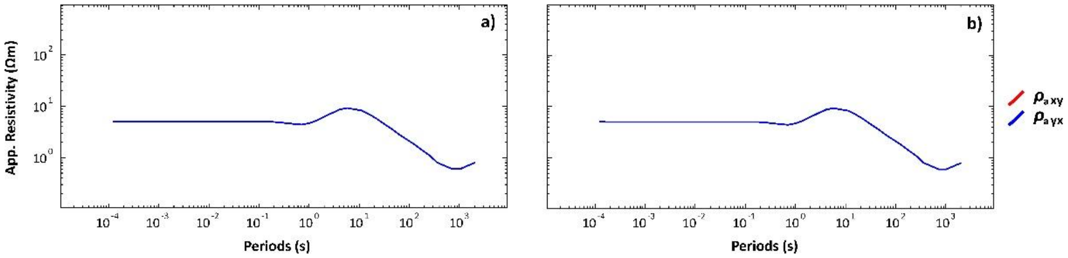

Figure 5.12 - Model response a) without and b) with the inclusion of the Posidonia black shale layer. Both model responses are virtually the same which implies a resistive Posidonia shale layer is unresolvable.

6 Main conclusions and outlook

This study presents a series of interesting results which indicate that black shales are not always good conductors and that their electrical conductivity is rather dependent on a variety of factors.

It was fairly well understood that high organic carbon content can cause high electrical conductivity in black shales. However, in order to conduct electricity in an optimal way, carbon needs to be in a highly aromatized chemical arrangement, such as carbon in graphite. For carbon to reach this stage it needs to be thermally matured, or in other words, needs to be exposed to very high temperatures (>400°C). Otherwise, carbon has high electrical resistivity.

The laboratory measurements on dry Posidonia black shale (PBS) samples carried out as part of this thesis confirm this. Between the immature and gas stages of thermal maturation (<200°C), electrical resistivity of the PBS mostly ranges between higher than 10^3 and 10^6 Ωm, with the lowest values measured around 100 Ωm, at the gas stage. No direct correlation was observed, however, between electrical resistivity and thermal maturity. The Harderode samples showed the highest electrical resistivity values and the Haddessen samples the lowest. The reason for this result is not clear since aromatization of the organic carbon of the PBS did increase from Wickensen to Haddessen. An unsuccessful drying process of the samples and the consequent presence of moisture in the pore structure leading to a more porosity controlled electric conduction through the samples could have been the cause. The compositional heterogeneity of the PBS became evident when all measurements of electrical resistivity done perpendicular to rock bedding resulted higher than those done parallel to rock bedding. Furthermore, the electrical resistivity of the PBS samples decreased significantly when soaked with distilled and salty water and showed high dependence on porosity, at least for PBS samples in the immature and oil stages. This indicates electric conduction is predominantly controlled by pore fluid and porosity rather than by carbon content at these thermal maturity.

Because electrical conductivity of black shales depends on thermal maturity, successful magnetotelluric (MT) exploration of black shales also depends on their thermal maturity. According to the basin model of the Lower Saxony Basin (LSB), the thermal maturity range of the PBS formation for which we obtained our two-dimensional (2D) MT inversion model is comparable to that of the samples. Towards the southern end of the model the

PBS is in the anthracite stage and in the immature stage for the northern end of the profile. The 2D inversion model shows a number of conductive features within the depth range of the PBS. However, where the PBS is more mature it coincides with a more resistive feature and where it is less mature it coincides with a conductive feature. It is likely that the referred conductive features are best explained by brines present in over- and underlying porous sediments and the PBS as well. The thickness of the black shale layers is only of 100 m and is found between clay-rich sandstones. Furthermore, the laboratory results suggest that the thermal maturity of the PBS in the MT survey area is not high enough to be electrically conductive.

The deeper conductive features in the 2D inversion model, however, are most likely caused by thermally mature Carboniferous coals. Due to their greater depth of burial (>3 km), these coals are very likely thermally more mature (meta-anthracite to graphite stage) than the PBS and consequently, more electrically conductive. The electrical conductivity associated with the shallower Westphalian coal layer is around 1 Ωm at the southern end of the inversion model and ends at around 20 Ωm for its northern end. Therefore, even though the PBS was not successfully resolved within the sedimentary sequences of the LSB with MT, one cannot exclude the possibility of resolving it in areas where thermal maturity is higher.

As an outlook, further analysis could be done of the remaining GASH MT data which was left out of the inversion modelling. Due to high level of EM noise, the stations 1 to 27 the southernmost 13 km of the MT data could not be included in the inversion modelling, out of time considerations. As this data is located in an area where thermal maturity is higher it may be possible to resolve the PBS with MT as a conductive feature. I suggest that in an eventual, more detailed analysis of this particular data that was left-out, thorough investigation could still be done with the SEL4ROB tool. Also, one could try using an activity filter based on the Wiener filter and also do a multi-remote reference approach, in order to improve the data. Then, an integration of this research could be done with the already performed CS-MT and seismic experiments, which were done in the same section of the MT profile that was left out. These experiments impart different and valuable information that can be used as a constraint in inversion modelling and consequently help in obtaining clearer results.

7 Appendix

In Figures 7.1, 7.2, 7.3 and 7.4 I show the selected measured transfer functions of the GASH stations (points) and the corresponding responses (lines) of 2D model inversions. The data of each station is presented in three diagrams. The axis scale and the data of every graph follows a conventional representation of MT data. The abscissa of all the graphs is the period length T in seconds, the axis is located between logarithmic 10^{-4} and 10^{4} s. The ordinate of the upper diagram shows the apparent electrical resistivity ρ_a, with a logarithmic axis division of 10^{-1} to 10^{3} Ωm. The ordinate of the middle diagram of each station is the phase linearly divided between 0° and 90°. The lower diagram, slightly narrower each chart shows the vertical magnetic transfer function T_y, and the ordinate is linearly divided between -1 and 1. Regarding the color coding of the curves, in the top two graphs, $\rho_{a\,xy}$ and ϕ_{xy} shown in red (corresponding to the case of rotated 2D data of the TE mode) and $\rho_{a\,yx}$ and ϕ_{yx} (in 2D TM mode) are shown in blue. In the case of the vertical magnetic transfer function T_y, the real part (Re(T_y)) has the colour of red and the imaginary part (Im(T_y)) has the colour of blue.

In Figures 7.5, 7.6 and 7.7 I show the electrical impedance measurements done at each Posidonia black shale sample. The abscissa of the graphs represents the frequency range in log_{10}Hz, the axis is located between 0 and 3. The ordinate of the graphs represents the electrical impedance in Ω. The color coding stands for different iterations of the electrical impedance measurement.

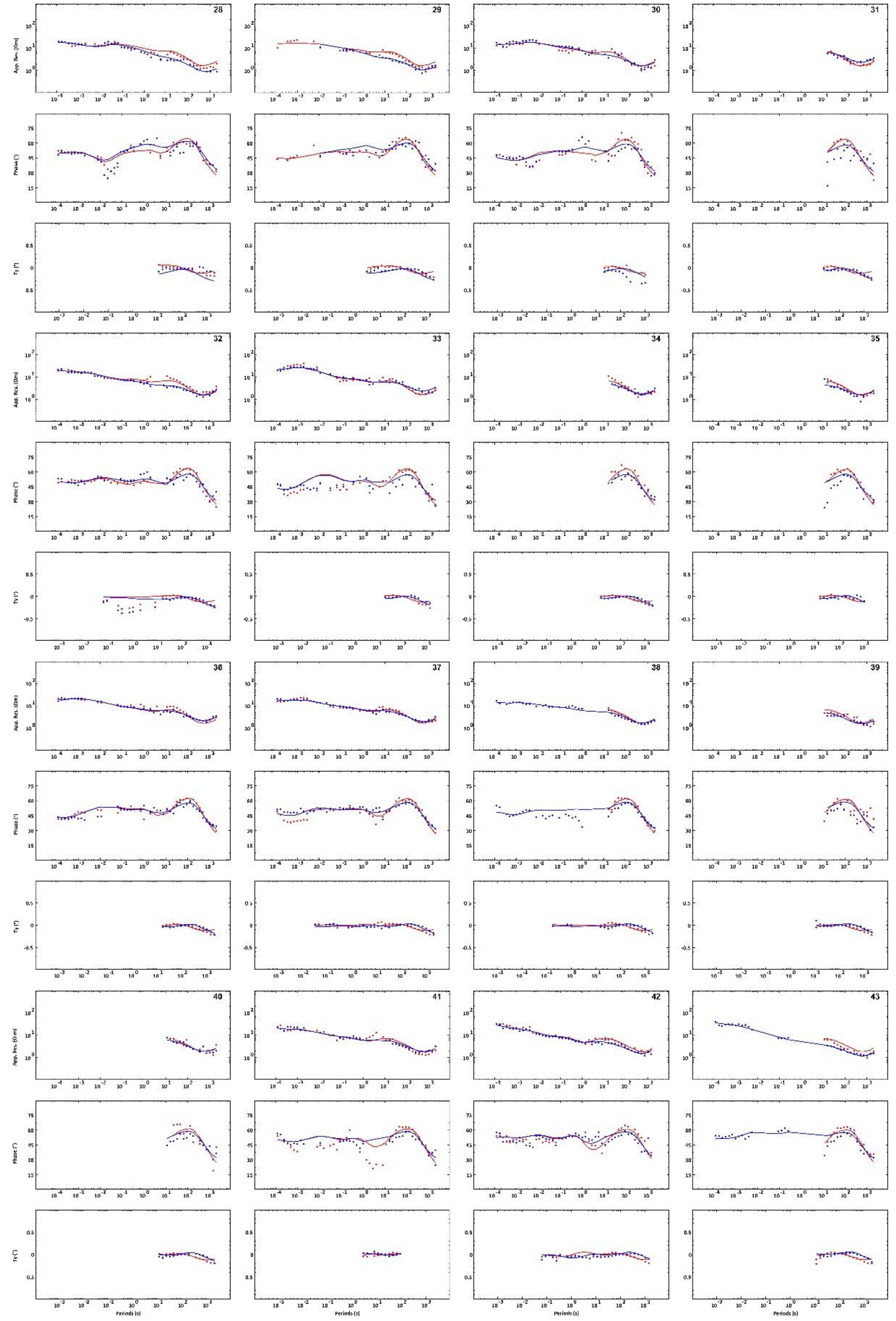

Figure 7.1 - Measurement data and model response of the preferred 2D model (Figure 4.17) for GASH stations 28 to 43. See text for corresponding diagram description.

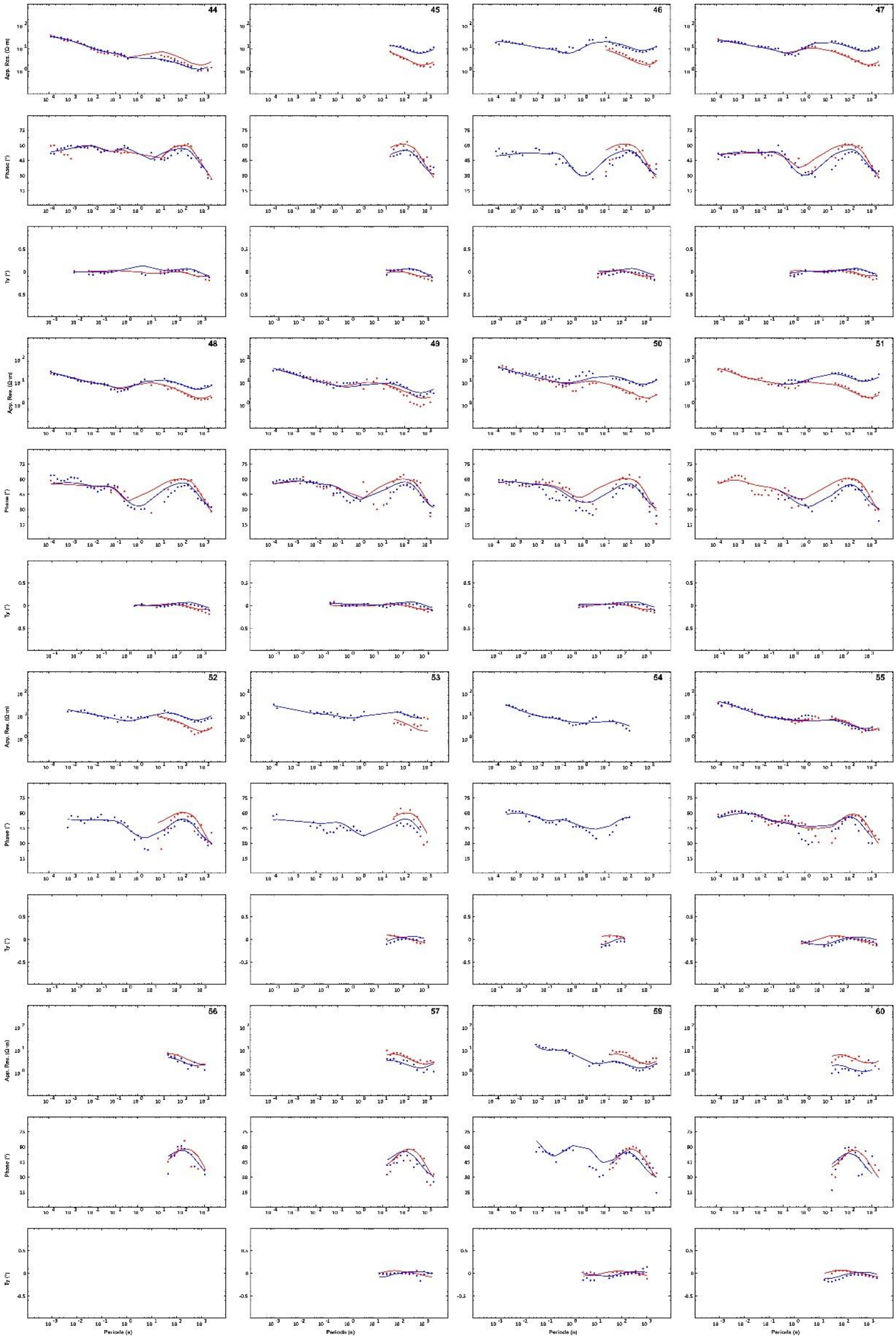

Figure 7.2 - Measurement data and model response of the preferred 2D model (Figure 4.17) for GASH stations 44 to 60. See text for corresponding diagram description.

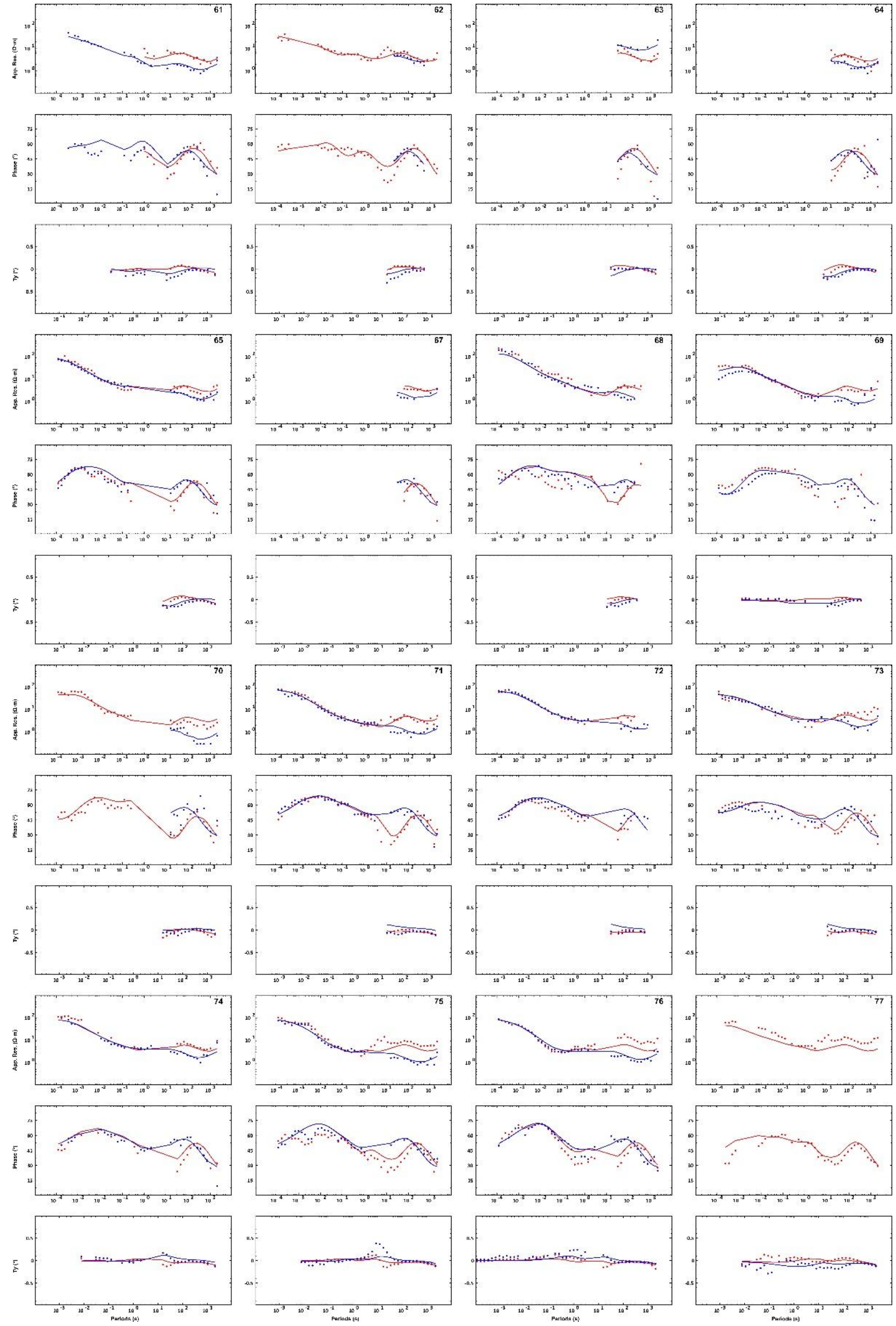

Figure 7.3 - Measurement data and model response of the preferred 2D model (Figure 4.17) for GASH stations 61 to 77. See text for corresponding diagram description.

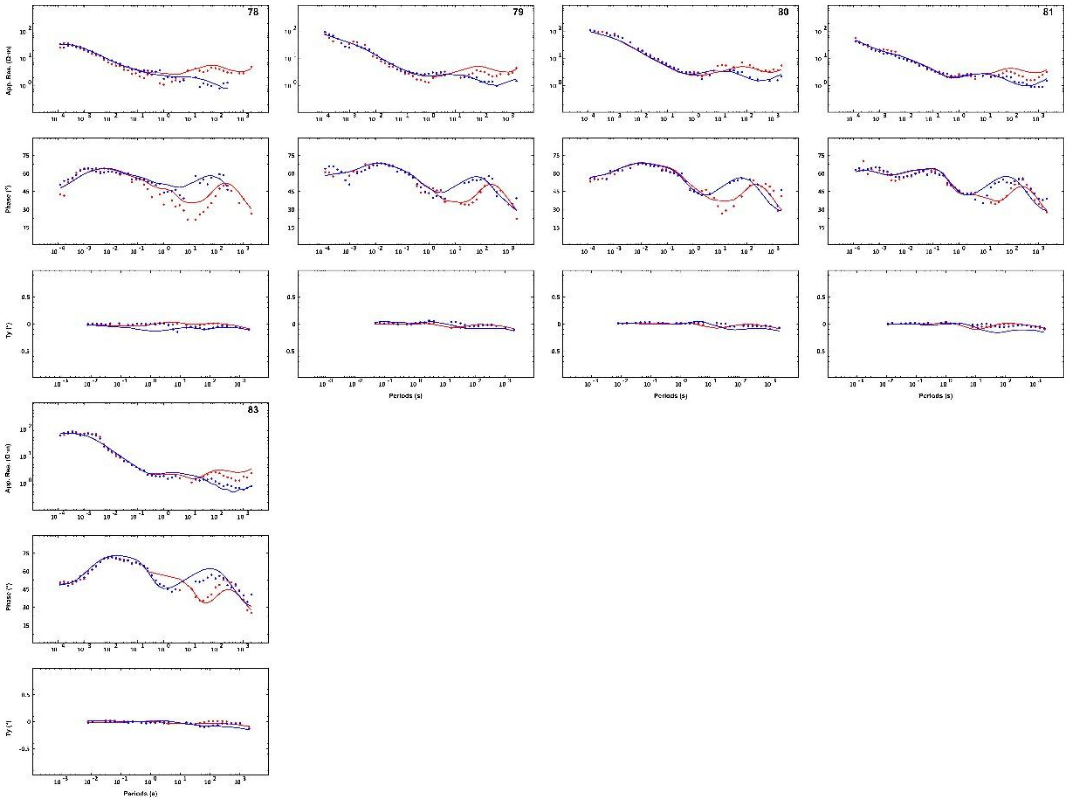

Figure 7.4 - Measurement data and model response of the preferred 2D model (Figure 4.17) for GASH stations 78 to 83. See text for corresponding diagram description.

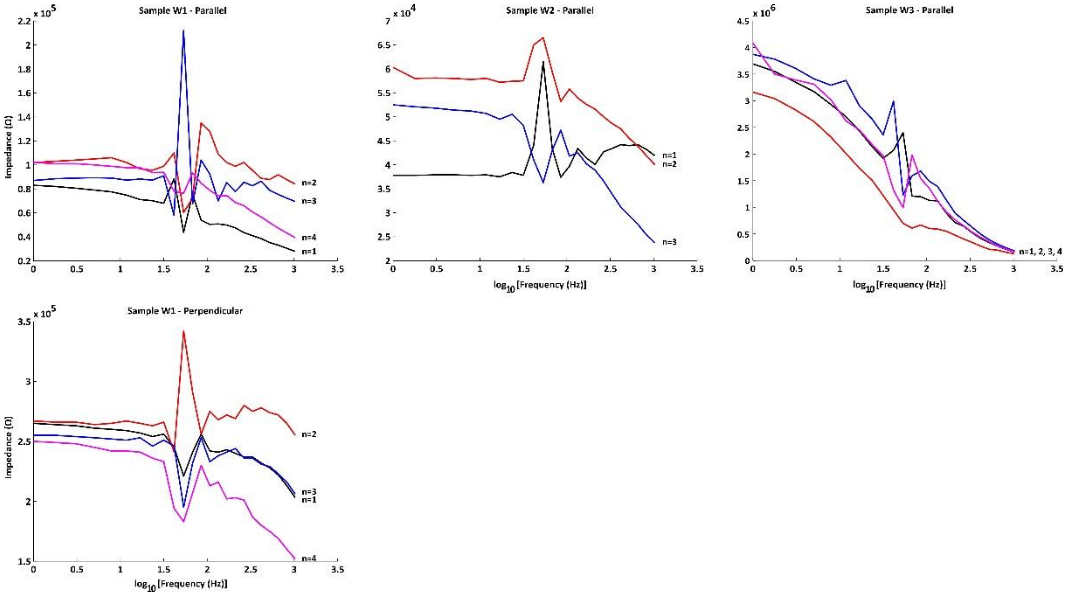

Figure 7.5 - Measured electrical impedance for the Wickensen Posidonia black shale samples. See text for corresponding diagram description.

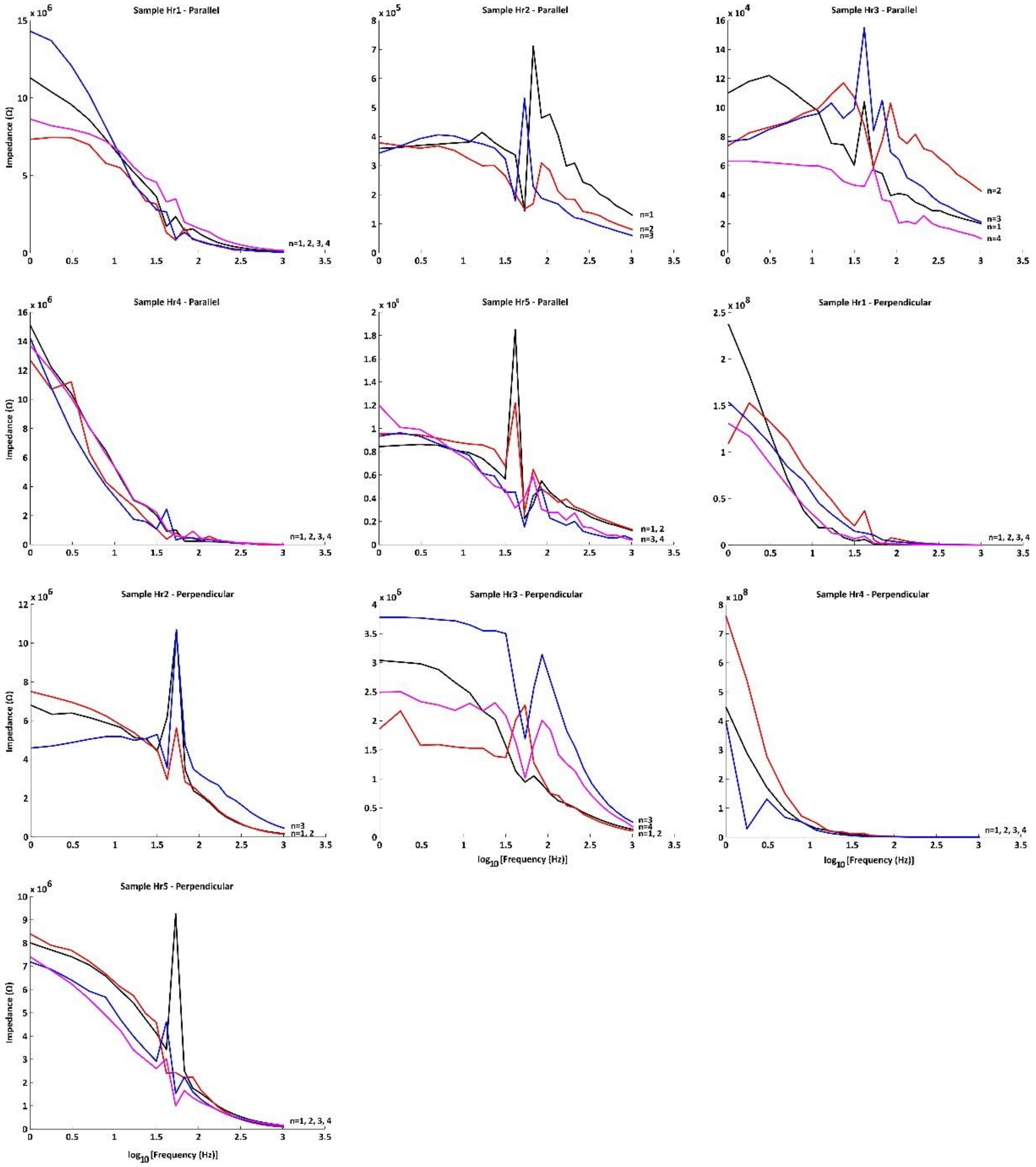

Figure 7.6 - Measured electrical impedance for the Harderode Posidonia black shale samples. See text for corresponding diagram description.

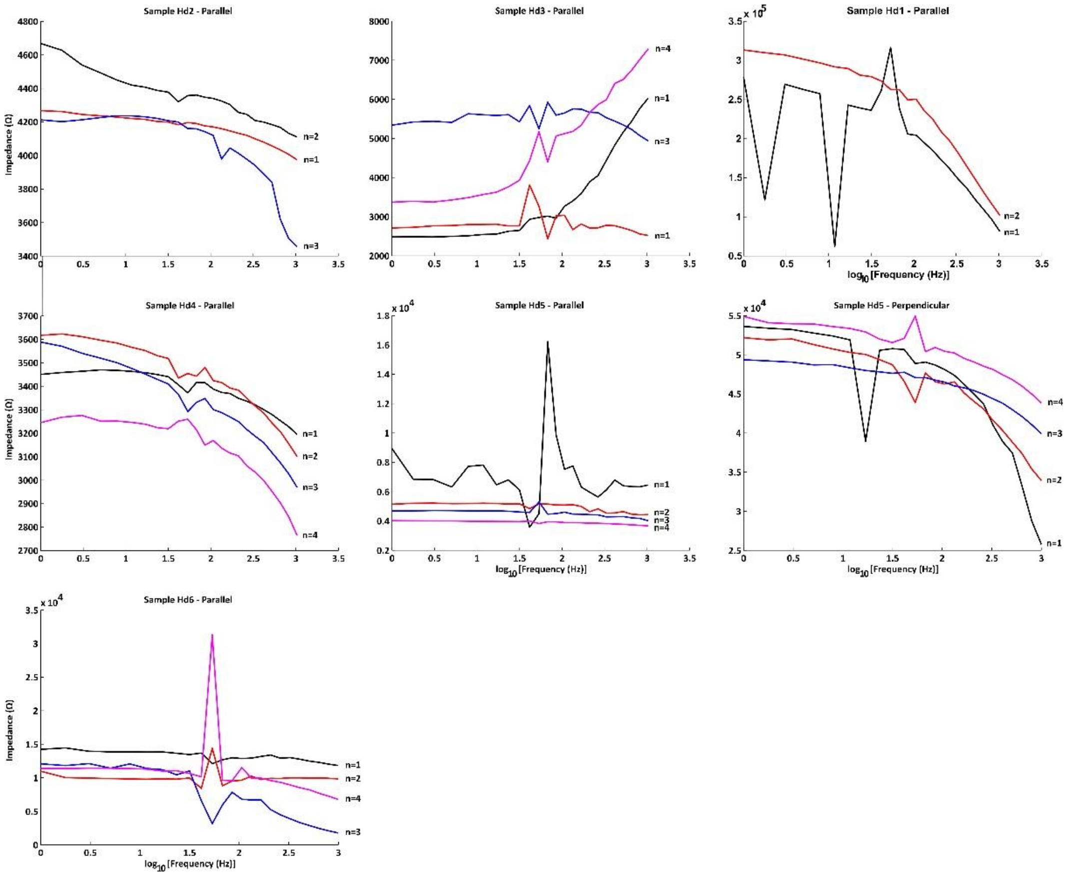

Figure 7.7 - Measured electrical impedance for the Haddessen Posidonia black shale samples. See text for corresponding diagram description.

References

Adriasola-Munoz, Y., Littke, R. & Brix, M. (2007). Fluid systems and basin evolution of the western Lower Saxony Basin, Germany. *Geofluids,* **7**, 335–355.

Ahmad, M., Haj Abdallah, M., Zihlif, A. & Abdelazeez, M. (1991). Electrical properties of oilshale rocks. *Journal of materials science,* **26**, 203-207.

Amelinckx, S., Delavignette, P. & Heerschap, M. (1965). *Chemistry and Physics of Carbon* (Vol. 1). (J. E. Walker P.L., & M. Dekker, Eds.) New York.

Bahr, K. (1988). Interpretation of the magnetotelluric impedance tensor: regional induction and local telluric distortion. *Journal of Geophysics*. **62**, 119–127.

Baldschun, R., Binot, F., Fleig, S. & Kockel, F. (2001). *Geotektonischer Atlas von Nordwest-Deutschland und dem deutschen Nordsee-Sektor.* Hannover.

Bartenstein, H., Teichmüller, M. & Teichmüller, R. (1971). Die Umwandlung der organischen Substanz im Dach des Bramscher Massivs. *Fortschritte in der Geologie von Rhein- land und Westfalen,* **18**, 501–538.

Bayer, U., Scheck, M. & Hauf, Y. (1995). Structural evolution of the Northeast German Basin during Early Permian to Keuper — volumetric analysis of sediment accumulation in the Northeast German Basin. *Terra Nostra, 95,* **8**, 80.

Becken, M. & Burkhardt, H. (2004). An ellipticity criterion in magnetotelluric tensor analysis. *Geophysical Journal International, 159,* **1**, 69-82.

Becken, M., Ritter, O., Park, S., Bedrosian, P., Weckmann, U. & Weber, M. (2008). A deep crustal fluid channel into the San Andreas Fault system near Parkfield, California. *Geophys. J. Int.,* **173**, 718–732.

Benek, R., Kramer, W., McCann, T., Scheck, M., Negendank, J., Korich, D. & Bayer, U. (1996). Permo-Carboniferous magmatism of the NE German basin. *Tectonophysics,* **266**, 379–404.

Bernard, S., Brown, L., Horsfield, B., Schulz, H.-M., Wirth, R., Schreiber, A. & Mathia, E. (2013). FIB-SEM and TEM Investigations of an Organic-rich shale Maturation Series from the Lower Toarcian Posidonia Shale, Germany: Nanoscale Pore System and Fluid-rock Interactions. In *Electron microscopy of shale hydrocarbon reservoirs,* **202**, 53-66.

Bernard, S., Schulz, H.-M., Wirth, R., Schreiber, A. & Sherwood, N. (2012b). Geochemical evolution of organic-rich shales with increasing maturity: A STXM and TEM study of the Posidonia Shale (Lower Toarcian, northern Germany). *Marine and Petroleum Geology,* **31**, 70-89.

Betz, D., Führer, F., Greiner, G. & Plein, E. (1987). Evolution of the lower saxony basin. *Tectonophysics,* **137**, 127– 170.

Branch, T., Ritter, O., Weckmann, U., Sachsenhofer, R. & Schilling, F. (2007). The Whitehill formation: a high conductivity marker in the Karoo Basin. *South. Afr. J. Geol.,* **110**, 465–476.

Breitkreuz, C. & Kennedy, A. (1999). Magmatic flare-up at the Carboniferous/Permian boundary in the NE German basin revealed by shrimp ages. *EUG - J. Confer. Abstracts,* **10**, 290.

Breyer, F. (1971). Geophysikalische und geologische Beiträge zur oberflächennahen oberflächennahen Tektonik im Dach des Bramscher Massivs. *Fortschritte in der Geologie von Rheinland und Westfalen*, **18**, 353-386.

Bruns, B., di Primio, R., Berner, U. & Littke, R. (2013). Petroleum system evolution in the inverted Lower Saxony Basin, northwest Germany: a 3D basin modeling study. *Geofluids,* 13, **2**.

Buehnemann, J., Henke, C., Müller, C., Krieger, M., Zerilli, A. & Strack, K. (2002). Bringing complex salt structures into focus – A novel integrated approach. *SEG Expanded Abstracts,* **21**, 446–449.

Cagniard, L. (1953). Basic theory of the magneto-telluric method of geophysical prospecting. *Geophysics,* **18**, 605–635.

Chave, A., & Jones, A. (2012). *The Magnetotelluric Method: Theory and Practise.* Cambridge University Press.

Chen, X. (2008). Filterung von geophysikalischen Zeitreihen mit periodisch auftretenden multifrequenten Störsignalen. *Diploma thesis*, Technical University of Berlin.

Dakhnov, V. (1962). Intepretation of the results of Geophysical Investigations of Well sections. *Gostoptekhizdat*.

Duba, A. (1983). Electrical conductivity of Colorado oil shale to 900 °C. *Fuel,* **62**, 966–972.

Duba, A., Huenges, E., Never, G., Will, G. & Jödicke, H. (1988). Impedance of black shale from Münsterland1 borehole: An anomalously good conductor? *Geophys. J.*, **94**, 413-419.

Espitalié, J., Marquis, F., Sage, L. & Barsony, I. (1987). Géochemie organique du bassin de Paris. *Revue de l'Institut Français du Pétrole*, **42**, 271–302.

Eydam, D. & Munoz, G. (2012). The Permanent Magnetotelluric Remote Reference Station. In R.-U. S. Börner (Ed.), *Protokoll über das 24. Schmucker-Weidelt-Kolloquium für Elektromagnetische Tiefenforschung*, (pp. 45-56). Neustadt a. d. Weinstraße.

Flotow, A., Berroth, A. & Schmehl, H. (1931). Relative Bestimmungen der Schwerkraft auf 115 Stationen in Norddeutschland. *Veröffentlichung preußisch geodätisches Institut*, **106**, 1-88.

Fowler, R., Kotick, B. & Elliot, R. (1967). Polarization analysis of naturally and artificially geomagnetic micropulsations. *J. geophys. Res.*, **72**, 2871-2883.

Franke, D., Hoffmann, N. & Lindert, W. (1996). The Variscan deformation front in east Germany, Part 2. Tectonic interpretation. *Z. Angew. Geol.*, 42, **1**, 44-54.

Gamble, T., Goubau, W. & Clarke, J. (1979). Magnetotellurics with a remote magnetic reference. *Geophysics, 44,* **1**, 53-68.

Gaucher, E. (1983). Estimation of Sulfide Content of a Potential Orebody from Surface Observations and its Role in Optimising Explorations Programmes. *A. A. Fitch (ed.), Developments in Geophysical Exploration Methods*, 4.

Gerling, P., Kockel, F. & Krull, P. (1999a). *Das Kohlenwasserstoff–Potential des Pr€awestfals im norddeutschen Becken – Eine Synthese.* DGMK, 433, Hamburg.

Goes, S., Govers, R. & Vacher, P. (2000). hallow mantle temperatures under Europe from P and S wave tomography. *J. Geophys. Res., 105,* **B5**, 11153-11169.

Gölke, M. & Goblenz, D. (1996). Origins of the European regional stress field. *Tectonophysics*, **266**, 11–24.

Goubau, W., Gamble, T. & Clarke, J. (1978). Magnetotelluric data analysis: removal of bias. *Geophysics, 43,* **6**, 1157-1166.

Gramann, F. H., Klassen, H., Kockel, F., Dulce, G., Harms, F.-J., Katschorek, T. & Weiss, M. (1997). Das Niedersächsische Oberjura-Becken - Ergebnisse interdisziplinärer Zusammenarbeit. *Zeitschrift der Deutschen Geologischen Gesellschaft,* **148**, 165-236.

Haak, V. & Hutton, R. (1986). Electrical resistivity in continental lower crust. *Geological Society (Special Publications),* 24, **1**, 35-49.

Hahn, A., & Kind, E. (1971). Eine Interpretation der magnetischen Anomalie von Bramsche. *Fortschritte in der Geologie von Rheinland und Westfalen*, **18**, 423-428.

Hedemann, H., Schuster, A., Stancu-Kristoff, G. & Lösch, J. (1984). Die Verbreitung der Kohlenflöze des Oberkarbons in Nordwestdeutschland und ihre stratigraphische Einstufung. *Fortschritte in der Geologie von Rheinland und Westfalen,* **32**, 39-88.

Heidbach, O., Tingay, M., Barth, A., Reinecker, J., Kurfeß, D. & Müller, B. (2008). The 2008 Release of the World StressMap. In: www.world-stress-map.org.

Hoffmann, N., Jödicke, H. & Horeshschi, L. (2005). Regional distribution of the Lower Carboniferous culm and carboniferous limestone facies in the North German Basin: derived from magnetotelluric soundings. *Z. Deut. Ges. Geowiss.,* 156, **2**, 323–339.

Hoffmann, N., Jödicke, H. & Horeshschi, L. (2008). The contribution of magnetotellurics to an improved understanding of the geological evolution of the North German Basin – review and new results. *Z. Deut. Ges. Geowiss.*, 159, **4**, 591–606.

Horsfield, B., Schulz, H.-M., Aplin, A., Doornenbal, H., Moretti, I., Lorant, F. & Thomas, R. (2010). Shale gas research: the way forward for Europe. *Oilfield Technology,* **3**, 14-18.

Iliceto, V. & Santarato, G. (1999). On the interference of man-made EM fields in the magnetotelluric 'dead band'. *Geophysical Prospecting*, **47**, 707-719.

IOC, IHO & BODC. (2003). *Centenary Edition of the GEBCO Digital Atlas.* Liverpool: British Oceanographic Data Centre.

Jarvie, D., Hill, R., Ruble, T. & Pollastro, R. (2007). Unconventional shale-gas systems: The Mississipian Barnett Shale of north-central Texas as one model for thermogenic shale-gas assessment. *AAPG Bulletin,* 91, **4**, 475-499.

Jenkins, G. & Watts, D. (1968). Spectral Analysis and Its Applications. *Holden-Day*.

Jenkins, H. (1985). The early Toarcian and Cenomanian-Turonian anoxic events in Europe — comparisons and contrasts. *Geologische Rundschau*, **74**, 505–518.

Jiracek, G. (1990). Near-surface and topographic distortions in electromagnetic induction. *Surveys in Geophysics*, 11, **2-3**, 163–203.

Jödicke. (1992). Water and graphite in the Earth's crust: An approach to interpretation of conductivity model. *Surv. Geophys.*,**13**, 381-407.

Jones, A. (1979). On the difference between polarisation and coherence. *J. Geophys.*(45), 223–239.

Jones, F. & Price, A. (1970). The perturbations of alternating geomagnetic fields by conductivity anomalies. *Geophys. J. R. Astr. Soc.*, **20**, 317–334.

Keller, G. & Frischknecht, F. (1966). Electrical methods in geophysical prospecting. Eds: F. V. A. L. Cullen. Pergammon Press, Oxford.

Klaver, J., Desbois, G., Urai, J. & Littke, R. (2012). BIB-SEM study of the pore morphology in early mature Posidonia Shale from the Hils area, Germany. *International journal of Coal Geology*, **103**, 12-25.

Koch, G. & Arnemann, H. (1975). Die Inkohlung in Gesteinen des Rhät und Lias im südlichen Nordwestdeutschland. *Geologisches Jahrbuch*, **A28**, 45–55.

Kockel, F. (2002). Rifting processes in NW-Germany and the German North Sea Sector. *Geologie en Mijnbouw*, **81**, 149–158.

Kockel, F., Wehner, H. & Gerling, P. (1994). Petroleum systems of the lower Saxony basin, Germany. Eds.: Magoon, L.B.. *American Association of Petroleum Geologists Memoirs*, **60**, 573-586.

Korja, T. & Koivukoski. (1990). Magnetotelluric Soundings Along the SVEKA Profile in the Central Fennoscandian (Baltic) Shield, Finland. (Report n°17).

Kossow, D. & Krawczyk, C. (2002). Structure and quantification of factors controlling the evolution of the inverted NE German Basin. *Marine and Petroleum Geology*, **19**, 601–618.

Krings, T. (2007). *The influence of Robust Statistics, Remote Reference, and Horizontal Magnetic Transfer Functions on data processing in Magnetotellurics.* Diploma thesis, Westfählische Wilhelms-Universität Münster, GeoForschungsZentrum Potsdam, Germany.

Krishnan, K. & Ganguli, N. (1939). Large Anisotropy of the Electrical Conductivity of Graphite. *Nature*, **144**, 667-667.

Leythaeuser, D., Littke, R., Radke, M. & Schaefer, R. (1988). Geochemical effects of petroleum migration and expulsion from Toarcian source rocks in the Hils syncline area, NW-Germany. *Organic Geochemistry,* **13**, 489-502.

Littke, R. & Rullkötter, J. (1987). Mikroskopische und makroskopische Unterschiede zwischen Profilen unreifen und reifen Posidonienschiefers aus der Hilsmulde. *Facies*, **17**, 171-180.

Littke, R., Baker, D. & Leythaeuser, D. (1988). Microscopic and sedimentologic evidence for the generation and migration of hydrocarbons in Toarcian source rocks of different maturities. *Organic Geochemistry,* **13**, 549–59.

Littke, R., Fourtanier, E., Thurow, J. & Taylor, E. (1991). Silica diagenesis and its effects on lithification of Broken Ridge deposits, Central Indian Ocean. *Proceedings of the Ocean Drilling Program, Scientific Results,* **121**, 261-272.

Littke, R., Jendrzejewski , L., Lokay , P., Shuangqing, W. & Rullkötter , J. (1995). Organic geochemistry and depositional history of the Barremian-Aptian boundary interval in the Lower Saxony Basin northern Germany. *Cretaceous Research,* **19**, 581–614.

Loukola-Ruskeeniemi, K. (1989). Early Proterozoic Metamorphosed Black Shales in the Kainuu Schist Belt and in the Outokumpu Region. *Geological Survey of Finland,* **10** (Special Paper), 103-106.

Mackie, R. (2002). Users Manual and Software Documentation for Two-Dimensional Inversion of Magnetotelluric data. San Francisco, California.

Mann, U. (1987). Veränderungen von Porosität und Porengröße eines Erdölmuttergesteins in Annäherung an einen Intrusivkörper. *Facies*, **17**, 181-188.

Mann, U. & Müller, P. (1988). Source rock evaluation by well log analysis (lower Toarcian, Hils syncline). *Organic Geochemistry*, **13**, 109-119.

Manouchehri, H., Rao, K., Hanumantha & Forßberg, K. (2001). Triboelectriccharge, electrophysical properties and electrical beneficiation potential of chemically treated feldspar, quartz and wollastonite. *Mag. Electric. Separat.*, 1-24.

Maystrenko, Y., Bayer, U., Brink, H.-J. & Littke, R. (2008). The Central European Basin System – an Overview. In R. B. Littke (Ed.), *Dynamics of Complex Intracontinental Basins,* 15–34. Springer–Verlag, Berlin.

Maystrenko, Y., Bayer, U., Scheck-Wenderoth, M. & Littke, R. (2010). Salt movements within the Central European Basin System. *Erdöl Erdgas Kohle*, 126, **4**, 156-163.

Mazur, S. & Scheck-Wenderoth, M. (2005). Constraints on the tectonic evolution of the Central European Basin System revealed by seismic reflection profiles from Northern Germany. *Netherlands Journal of Geosciences — Geologie en Mijnbouw*, 84, **4**, 389-401.

Mitchell, J. & Soga, K. (1993). *Fundamentals of soil behaviour.* Wiley.

Morris, K. (1980). Comparison of major sequences of organicmatter-rich mud deposits in the British Jurassic. *Journal of the Geological Society*, **137**, 157-170.

Munoz, G., Ritter, O. & Moeck, I. (2010). A target-oriented magnetotelluric inversion approach for characterizing the low enthalpy Groß Schönebeck geothermal reservoir. *Geophysical Journal International*, 183, **3**, 1199-1215.

Mutterlose, J. & Bornemann, A. (2000). Distribution and facies patterns of Lower Cretaceous sediments in northern Germany - a review. *Cretaceous Research*, **21**, 733-759.

Newman, G. & Alumbaugh, D. (2000). Three-dimensional massively parallel inversion - I. Theory. *Geophysical Journal International*, **128**, 345-354.

Oberlin, A. (1989). High-resolution TEM studies of carbonization and graphitization. Ed.: Thrower, P.. *Physic and Chemistry of Carbon* , **22**.

Oberlin, A., Boulmier, J. & Villey, M. (1979). Electron microscopic study of kerogen microtexture selected criteria for determination of kerogen evolution path and evolution stage. Ed.: Durand, B.. *Kerogen, Technip,* Paris.

Olhoeft, G. (1981). Electrical properties of rocks. In: Physical Properties of Rocks and Minerals. Eds.: Touloukian, Y. S., Judd, W. R. & Roy, R. F.. *Physical Properties of Rocks and Minerals,* 257-330. McGraw-Hill, New York.

Parkhomenko, E. (1967). *Electrical Properties of Rocks*. Plenum Press US, New York.

Petiau, G. & Dupis, A. (1980). Noise, temperature coefficient and long-time stability of electrodes for telluric observations. *Geophysical prospecting,* **28**, 792-804.

Petmecky, S., Meier, L., Reiser, H. & Littke, R. (1999). High thermal maturity in the Lower Saxony basin: intrusion or deep burial?. *Tectonophysics*, **304**, 317-344.

Pierson, H. (1993). Handbook of carbon, graphite, diamond and fullerenes: Properties, processing and applications. Park ridge, New York, USA: Noyes publications.

Raab, S. (1998). Role of sulphur and carbon in the electrical conductivity of the middle crust. *Journal of geophysical research*, **13**, 9681-9689.

Rasser, M. & Harzhauser, M. (2008). *Palaeogene and Neogene*, 1031-1139.

Riegel, W., Loh, H., Maul, B. & Prauss, M. (1986). Effects and causes in a blackshale event – the Toarcian Posidonia Shale of NW-Germany. *Global bio-events – Lecture Notes in Earth Sciences*, 8, **6**, 267–276.

Ritter, O. (1996a). Kalibrierung von Metronix MFS05 Induktionsspulenmagnetometern. Eds.: Bahr, K., Junge, A.. *Protokol über das 16. Kolloquium "Elektromagnetische Tiefenforschung"*, Berg Ludwigstein.

Ritter, O., Junge, A. & Dawes, G. (1998). New equipment and processing for magnetotelluric remote reference processing observations. *Geophysical Journal Int.*, **132**, 535-548.

Rodi, W. & Mackie, R. (2001). Nonlinear conjugate gradients algorithm for 2-D magnetotelluric inversions. *Geophysics*, **66**, 174–187.

Rouzaud, J. & Oberlin, A. (1984). Contribution of high resolution transmission electron microscopy (TEM) to organic materials: Characterization and interpretation of their reflectance. Ed.: Durand, B.. *Thermal Phenomena in Sedimentary Basins*, 127-134.

Rouzaud, J. & Oberlin, A. (1990). The characterization of coals and cokes by transmission electron. Ed.: Charcosset, H.. Elsevier, Amsterdam.

Rullkötter, J. & Marzi, R. (1988). Natural and artificial maturation of biological markers in a Toarcian shale from northern Germany. *Organic Geochemistry*, **13**, 639-645.

Rullkötter, J., Leythaeuser, D., Horsfield, B., Littke, R., Mann, U., Müller, P. & Welte, D. (1988). Organic matter maturation under the influence of a deep intrusive heat source: a natural experiment for quantitation of hydrocarbon generation and expulsion from a petroleum source rock (Toarcian shale, northern Germany). *Organic Geochemistry*, **13**, 847-856.

Schäfer, A., Houpt, L., Brasse, H., Hoffmann, N. & Group, E. W. (2011). The North German Conductivity Anomaly revisited. *Geophys. J. Int.*, 187, **1**, 85-98.

Scheck, M. & Bayer, U. (1999). Evolution of the Northeast German Basin – inferences from a 3D structural model and subsidence analysis. *Tectonophysics,* **313**, 145-169.

Scheck, M., Bayer, U. & Lewerenz, B. (2003). Salt movements in the Northeast German Basin and its relation to major post-Permian tectonic phases—results from 3D structural modelling, backstripping and reflection seismic data. *Tectonophysics*, **361**, 277–299.

Scheck-Wenderoth, M. & Lamarche, J. (2005). Crustal memory and basin evolution in the Central European Basin System — new insights from a 3D structural model. *Tectonophysics*, **397**, 143–165.

Scheck-Wenderoth, M., Maystrenko, Y., Hübscher, C., Hansen, M. & Mazur, S. (2008). Dynamics of salt basins. Ed.: Littke, R.. *Dynamics of complex intracontinental basins: The Central European Basin System*, 307-322. Springer.

Scheidt, G. & Littke, R. (1989). Comparative organic petrology of interlayered sandstones, siltstones, mudstones and coals in the Upper Carboniferous Ruhr basin, Northwest Germany, and their thermal history and methane generation. *Geologische Rundschau*, **78**, 375-390.

Schmidt, A. (1914). Die magnetische Vermessung I. Ordnung des Königreichs Preußen, 1898 bis 1903, nach den Beobachtungen von M. Eschenhagen und J. Edler. *Veröffentlichung Preußisches Meteorologisches Institut*, 7 Kt.

Schmucker, U. (1987). Substitute Conductors for Electromagnetic Response Estimates. *PAGEOPH*, **125**, (**2-3**).

Schön, J. (2004). Physical Properties of Rocks: Fundamentals and Principles of Petrophysics (Handbook of Geophysical Exploration: Seismic Exploration). Pergamon.

Schöneberg & Neugebauer. (1987). *Einführung in die Geologie Europas.* Freiburg (Rombach).: - 294S.

Schwab, G. (1985). Paläomobilität der Norddeutsch–Polnischen Senke. Akademie der Wissenschaften, Potsdam (German DDR).

Selley, R. (1998). Elements of Petroleum Geology. Gulf Professional Publishing.

Senglaub , Y., Brix , M., Adriasola , A. & Littke, R. (2005). New information on the thermal history of the southwestern Lower Saxony Basin, northern Germany, based on fission track analysis. *International Journal of Earth Sciences,* **94**, 876–96.

Senglaub, Y., Littke, R. & Brix, M. (2006). Numerical modelling of burial and temperature history as an approach for an alternative interpretation of the Bramsche anomaly, Lower Saxony Basin. *International Journal of Earth Sciences,* **95**, 204–224.

Simpson, F. & Bahr, K. (2005). *Practical Magnetotellurics.* Cambridge University Press.

Smith, J. (1995). Understanding telluric distortion matrices. *Geophys. J. Int.,* **122**, 219 – 226.

Stollhofen, H., Bachmann, G., Barnasch, J., Bayer, U., Beutler, G., Franz, M. & Radies, D. (2008). Upper Rotliegend to Early Cretaceous basin development. Eds.: Littke, R.. *Dynamics of Complex Sedimentary Basins. The Example of the Central European.* , 181–210. Springer-Verlag, Berlin-Heidelberg.

Szarka, L. (1988). Geophysical Aspects of Man-Made Electromagnetic Noise in the Earth - A Review. *Surveys in Geophysics,* **9**, 287-318.

Tanner, B. & Meissner, R. (1996). Caledonian deformation upon southwest Baltica and its tectonic implications. Alternatives and consequences. *Tectonics*, 15, **4**, 803–812.

Teichmüller, H., Teichmüller, R. & Weber, R. (1979). Inkohlung und Illit-Kristallinität. Vergleichende Untersuchungen im Mesozoikum und Paläozoikum von Westfalen. *Fortschr. Geol. Rheinld. u. Westf.*, **27**, 201-276.

Teichmüller, M. & Ottenjhan, K. (1977). Art und Diagenese von Liptiniten und lipoiden Stoffen in einem Erdölmuttergestein auf Grund fluoreszenzmikroskopischer Untersuchungen. *Erdöl und Kohle*, **30**, 397-398.

Tikhonov, A. (1950). The determination of the electrical properties of deep layers of the earth’s crust. *Dokl. Akad. Nauk. SSR*, **73**, 295–297.

Tikhonov, A. & Arsenin, V. (1977). Methods for Solving Ill-Posed Problems. *Nauka*.

Tissot, B. & Welte, D. (1984). Petroleum Formation and Occurrence. Springer.

Toporets, S. (1961). On the effect of metamorphism on the electrical and elastic properties of commercial coals. *Dokl. Akad. Nauk SSSR, 140,* **2**.

Torsvik, T., Trench, A., Svensson, I. & Walderhaug, H. (1993). Paleogeographic significance of mid Silurian paleomagnetic. *Geophys. J. Int.*, **113**, 651–668.

Tourtelot, H. (1979). Black shale - Its deposition and diagenesis. *Clay and Clay Minerals,* 27, 5, 313--321.

Tyson, R. (1987). The genesis and palynofacies characteristics of marine petroleum source rocks. Eds.: Brooks, J. & Fleet, A.. *Marine petroleum source rocks*, **26**, 47-68.

van Wees, J.-D., Stephenson, R., Ziegler, P., Bayer, U., McCann, T., Dadlez, R. & Scheck, M. (2000). On the origin of the Southern Permian Basin, Central Europe. *Marine and Petroleum Geology*, **17**, 43–59.

Vandenbroucke, M. & Largeau, C. (2007). Kerogen origin, evolution and structure. *Organic Geochemistry*, 38, **5**, 719-833.

Villey, M., Oberlin, A. & Combaz, A. (1976). Pyrolyse d'une substance module de kerogene (sporopollenine). *Etude au microscope electronique*, **D282**, 1657-1660.

Villey, M., Oberlin, A. & Combaz, A. (1979). Influence of elemental composition on carbonization pyrolysis of sporopollenin and lignite as models of kerogens. *Carbon*, **17**, 77-86.

Walter, R. (1995). *Geologie von Mitteleuropa*, **6**, 566.

Walters, C., Kliewer, C., Awwiller, D. & Rudnicki, M. (2014). Influence of turbostratic carbon nanostructures on electrical conductivity. *International Journal of Coal Geology*, **122**, 105-109.

Weckmann, U., Jung, A., Branch, T. & Ritter, O. (2007b). Comparison of electrical conductivity structures and 2D magnetic modelling along two profiles crossing the Beattie magnetic anomaly. *South African Journal of Geology*, **110**, 449–464.

Weckmann, U., Magunia, A. & Ritter, O. (2005). Effective noise separation for magnetotelluric single site data processing using a frequency domain selection scheme. *Geophysical Journal International*, 161, **3**, 635–652.

Welte, D. (1979). Organisch-geochemische Untersuchungen zur Bildung von Erdo¨l-Kohlenwasserstoffen an Gesteinen des mittleren Oberrhein-Grabens. *Fortschritte in der Geologie von Rheinland und Westfalen*, **27**, 51–73.

Wiese, H. (1962). Geomagnetische tiefensondierung. Teil II: Die Streichrichtung der Untergrundstrukturen des elektrischen Widerstandes, erschlossen aus geomagnetischen variationen. *Geofis. Pura et Appl.*, **52**, 83–103.

Wignall, P. (1994). Black Shales. Oxford University Press.

Zhdanov, M. (2009). Geophysical electromagnetic theory and methods. In *Methods in Geochemistry and Geophysics*, 848. Elsevier, Salt Lake City.

Ziegler, P. (1990). Geological atlas of Western and Central Europe. Geological Society of London, 256 pp., Hague.

List of figures

List of tables

Acknowledgements

I sincerely thank Dr. Oliver Ritter for giving me the opportunity to come to Germany and do my PhD at the GeoForschungZentrum in Potsdam. His supervision, encouragement and guidance was of upmost importance for my work, but more importantly for my evolution as a young scientist working in geophysics.

I would also like to give my sincere thanks Dr. Erik Spangenberg for helping me in my laboratory work. Without his knowledge, counselling and direct assistance all of my petro-physical research wouldn’t have been possible.

I gratefully thank Dr. Brian Horsfield, Dr. Hans-Martin Schulz, Dr. Ulrich Mann and Dr. Kai Jasper in helping me look for a suitable study area and providing me the black shale samples I needed to work on.

I am very thankful to MSc. Diane Eydam, Dr. Rita Streich and Dr. Ute Weckmann for helping me in the preparation and realization of my MT field campaign. Their contribution was crucial and essential to that part of my work. Furthermore, I would also like to express my sincere gratitude to all of those who took their time to help me in the field acquiring MT data and also to the land owners who granted access to their properties.

I thank a lot Dr. Gerard Muñoz, Dr. Gerhard Kapinos and Dr. Ute Weckmann for helping me processing my MT data-set, but also with all things related to my MT work. On this note, I also thank Dr. Naser Meqbel for his helpful advice on 2D MT inversion modelling.

I really thank Alex Reichard, Christina Rudolph and Scott Angus MacLennan for their help preparing the black shales samples in the laboratory.

I thank all of my GASH project partners and colleagues who have given me helpful data and information that I could work with. I specially acknowledge Eliza Mathia and Thomas Rexer from Newcastle University and Nicolaj Mahlstedt from GFZ Potsdam for the fruitful discussions concerning petro-physical aspects of the Posidonia black shale, and Benjamin Bruns from RWTH Aachen for sharing data on his Lower Saxony basin model.

To all my present and former colleagues in GFZ, my many thanks for your comradery, kindness and help that you have given me.

This work was funded within the framework GASH interdisciplinary project. All of the instruments for the magnetotelluric experiments were provided by the Geophysical Instrument Pool Potsdam (GIPP).

To all my friends, thank you for your invaluable companionship during my time in Germany so far. A special mention to my girlfriend, Martina, who has been inspiring, encouraging and remarkably supportive of me.

Last but not least, my biggest thanks to my parents, Maria de Fátima Santos Cordeiro and Martinho Manuel Ferreira Adão, for caring and always being there for me. I wouldn’t have been able to make this thesis without you. Muito, muito obrigado!

Erklärung

Hiermit versichere ich, daß ich die vorliegende Arbeit selbständig verfaßt und keine anderen als die angegebenen Hilfsmittel benutzt habe. Die Stellen der Arbeit, die anderen Werken wörtlich oder inhaltlich entnommen sind, wurden durch entsprechende Angaben der Quellen kenntlich gemacht.

Diese Arbeit hat in gleicher oder ähnlicher Form noch keiner Prüfungsbehörde vorgelegen.

Teile von dieser Dissertation sind veröffentlicht in:

Adao, F., Ritter, O. & Spangenberg, E. (2015). The electrical resistivity of Posidonia black shale – from magnetotelluric exploration to rock samples. *Geophysical Prospecting*, Accepted.

Potsdam, 20. November 2014